AERO-PROPULSIVE CHARACTERISTICS OF AN OVERWING DISTRIBUTED ELECTRIC PROPULSION SYSTEM WITH VECTORED THRUST

BY

DANIEL B. YU

THESIS

Submitted in partial fulfillment of the requirements
for the degree of Master of Science in Aerospace Engineering
in the Graduate College of the
University of Illinois at Urbana-Champaign, 2021

Urbana, Illinois

Adviser:

Assistant Professor Phillip J. Ansell

Abstract

A series of experiments were conducted on a quasi-2D S8036 airfoil with a distributed electric propulsion (DEP) system. An overwing ducted fan system was tested with varied thrust angles achieved by deflecting the fan exit flow direction. The DEP system was comprised of five electric fans mounted on the upper surface of the airfoil trailing edge. The electric ducted fans were sized with a diameter-to-chord ratio of 19.7%, and five fans were installed to cover 70.3% of the airfoil model span. Aerodynamic forces and moments were recorded for the airfoil in a static condition, as well as across a range of Reynolds numbers, angles of attack, tip speed ratios, and nozzle deflection angles. It was found that nozzle deflection led to a significant increase in the stream-normal force due to an increase in circulation-based lift and direct thrust force. At low thrust deflection angles, increases in stream-normal forces were also observed, alongside significant amounts of forward thrust, with increased fan tip speed ratio. At a given nozzle defleciton angle and fan tip speed ratio, minimal variations in pressure distributions were found across the spanwise region covered by the center-fan radius, suggesting a reasonably spanwise-invariant loading produced by the installation of the overwing ducted fan DEP system. Thrust vectoring was also observed to increase the magnitude of the overall pitching moment, and this effect was significantly amplified by the tip speed ratio of the fans. These observations were attributed to the role of the vectored nozzle system in producing a jet-flap system, with varying induced circulation effects brought about by control of the nozzle deflection angle and the fan tip speed ratio.

Acknowledgements

To begin, I would like to wholeheartedly thank my academic advisor Prof. Phil Ansell. I will always be grateful for his continued guidance and support, which has enabled me to learn, grow, and achieve more in my research than I had ever expected. This work would not have been complete without his help throughout the entire process. I consider myself very fortunate to have an advisor as patient and helpful as Prof. Ansell.

I would also like to thank Virgil Bourgon, whose generous donation supported this work and will continue to support research at the University of Illinois at Urbana-Champaign. I have always found his ambitious goals and desire to challenge conventional ways of thinking to be inspirational. I'd also like to thank Virgil for the copy of *Kelly: More Than My Share Of It All* which he had gifted to me. This, coincidentally, is one of my favorite books, and I greatly appreciated the gesture.

There are many individuals who have helped me in this process that I would like to thank. I am thankful for the help and advice given by Prof. Jason Merret, who also supported me, particularly in the model shop. I'd like to thank Georgi Hristov for entrusting me with his airfoil model, and I'd like to apologize for breaking one of the flap element flanges. I repaired it with JB weld, and as of this writing it is still in place. I'd also like to thank all the members of the Aerodynamics the Unsteady Flows Research group for being welcoming and helpful as I began my Master's degree studies and research.

Finally, I would like to thank my family for their never ending support and confidence in me. I will always think my parents are overblowing my accomplishments and enjoy long conversations with my brother. I also owe much of my academic and personal growth to the support of my loving girlfriend, whom I can always count on to prop me up when I feel down and prod me forward when I am holding back.

Table of Contents

List of Figures

List of Tables

Nomenclature

Acronyms

BLDC Brushless Direct Current

DC Direct Current

DEP Distributed Electric Propulsion

EDF Electric Ducted Fan

ESC Electric Speed Controller

eVTOL Electric Vertical Take Off and Landing

RPM Revolutions Per Minute

V/STOL Vertical/Short Take Off and Landing

Symbols

α	Angle of attack
α_0	Zero-lift angle of attack
δ_f	Flap deflection angle
δ_T	Thrust deflection angle
λ	Tip speed ratio
ω	Revolutions per minute
ρ_∞	Ambient air density
A_{fans}	Total fan-swept area
A_{ss}	Settling section cross sectional area
A_{ts}	Test section cross sectional area
b	Airfoil span
c	Airfoil chord
C_d	Drag coefficient (stream-axial force coefficient)
C_l	Lift coefficient (stream-normal force coefficient)
C_m	Quarter-chord pitching moment coefficient
C_p	pressure coefficient
C_{l_α}	Lift curve slope
C_{T_a}	Chord-axial thrust coefficient
C_{T_n}	Chord-normal thrust coefficient
C_T	Thrust coefficient
D	Stream-axial force (Drag)
D_f	EDF diameter
F_a	Chord-axial force
F_n	Chord-normal force
L	Stream-normal force (Lift)

M Pitching moment

$M_{c/4}$ Quarter-chord pitching moment

P_{amb} Ambient static pressure

P_{ss} Settling section static pressure

P_{ts} Test section static pressure

R Fan radius

Re Chord-based Reynolds number

T_{amb} Ambient static temperature

U_{∞} Test section velocity

U_{ss} Settling section velocity

U_{ts} Test section velocity

V_{tip} Fan tip speed

Chapter 1

Introduction

1.1 Background and Literature Review

In recent years, concerns regarding the environmental sustainability of traditional aviation fuels as well as advancements in battery technology and electric power systems have precipitated an interest in concepts for aviation which utilize fully electric or hybrid-electric vehicles for a variety of missions [1]. One such mission is short distance trips facilitated by fully electric or hybrid-electric vehicles that are capable of vertical/short take-off and landing (V/STOL). In response, many unique propulsion systems and means for propulsion system integration have been proposed. A large number of existing and novel designs incorporate some form of a fixed wing in order to facilitate a high-efficiency cruise capability. However, a challenge that affects the design of all fixed-wing VTOL propulsion systems is the transition from hover to forward flight. This period of flight can be difficult due to the limited control authority provided by traditional wing-tail control surfaces before the stall speed of the aircraft is reached. In addition, this period of flight poses significant power requirements on the vertical lift system due to the low speed and subsequent low amount of wing lift. Therefore, it would be of interest to investigate aero-propulsive systems that could be used to augment lift generation or improve vehicle controllablity in this regime.

Powered lift is a set of well known aero-propulsive methods for improving fixed wing lift performance at low speeds. These methods are characterized by utilizing secondary flow provided by an aircraft's propulsors to augment the flow field around a wing. Examples of powered lift methods can be generally categorized into blown flaps, jet flaps, and circulation control devices.

Historically, a wide range of powered lift configurations have been studied using traditional wing-and-pod propulsors or internally routed engine exhaust and bleed air [2]. Despite configuration and aero-propulsive differences between each of these methods, at a fundamental level their ability to augment wing lift can be attributed to a combination of increased circulation and direct vectoring of thrust in the lift direction [3]. Therefore, any propulsion system which generates a powered wake has the potential to demonstrate some amount aero-propulsive benefit through these mechanisms. The benefits of powered lift would be of particular use to fixed-wing aircraft that may be limited in power or need to operate at slow speeds, such as electric aircraft performing a V/STOL mission. Distributed electric propulsion (DEP) systems are one example of a system for which powered lift techniques could be particularly advantageous. A key benefit of electric power systems is the ability to distribute thrust-producing propulsors along a wing span instead of having thrust concentrated at a single location on a wing [4]. Unlike historical examples of augmentor wings which diverted engine bleed air or exhaust to achieve span-wise powered lift effects at the wing, a DEP system would theoretically be capable of applying the full output of its propulsors towards a powered lift system. In addition, significant interactions exist between distributed propulsion systems and the surrounding flow field, such as boundary layer ingestion and the effect of propulsor mass flow on circulation [5].

Given that many proposed V/STOL and electric or hybrid-electric aircraft designs incorporate distributed propulsion, it would be beneficial to investigate the ability of distributed electric propulsion (DEP) systems to beneficially utilize these aero-propulsive integration effects, which can be further controlled with the use of thrust vectoring across high-lift and low-speed flight regimes.

1.1.1 Powered Lift

One of the main categories of powered lift systems is jet flaps or jet wings, which are generally characterized by a wing and flap system where distributed ejectors are placed at or near the flap trailing edge. The emission of a propulsive jet from the wing trailing edge increases wing circulation through multiple mechanisms. This increase in circulation and lift is produced, in part, from the ability of a high momentum stream of air to support a pressure load beyond the airfoil trailing edge [6]. The entrainment and acceleration of flows, as well as direct vectoring of propuls-

ive flow, also serve to increase wing circulation [3]. Example of jet flaps can be seen in the C-8A Augmentor Wing Jet STOL Research Aircraft aircraft built by Boeing, which contained ducting systems to divert fan flow from each engine to the flaps and ailerons of the aircraft, and the Hunting H.126, which also ducted engine exhaust over the full span of flaps and ailerons [7] [2]. These aircraft demonstrated the clear aero-propulsive benefits of jet wings; for example, the H.126 was found to be capable of lift coefficients greater than 6 [8]. However, an important challenge for jet flaps is the increased structural complexity and weight associated with the necessary ducting systems. Given the established literature regarding jet flaps, it is evident that DEP systems comprised of propulsors mounted directly along a wing present a novel source of distributed, high-momentum efflux which could have similar aero-propulsive benefits.

Another category of powered lift that has been successfully applied in multiple aircraft is blown flaps. The increased lift provided by such a configuration also results primarily from the use of a high-momentum jet, which generates a powered wake with increased total pressure beyond that of the freestream. This local excess in total pressure is capable of supporting a pressure load and, thus, introduce wake circulation effects that are observed across the wing and flap surfaces. The momentum provided within the propulsor streamtube can also be used to delay the bursting of the main-element wake as well as the separation of the flap boundary layer [9]. Wing and propulsor configurations that employ this concept, such as wings with upper surface blowing and blown flaps, have been extensively studied in the past [10, 11]. However, most cases that have been studied involved discretely-podded jet and propeller configurations, with limited attention to extensively distributed aero-propulsive systems.

Wind tunnel testing has shown that a blown wing section could achieve extremely high lift coefficients with the use of a distribution of underwing-mounted propellers [12]. This suggests that a distributed propulsion system with vectored thrust mounted near the trailing edge of a wing could produce a similar effect. These characteristics would be beneficial to a winged V/STOL aircraft during the transition period, as extremely high lift coefficients can be achieved with the use of the powered DEP system.

1.1.2 Distributed Propulsion

Distributed propulsion is an aero-propulsive concept which utilizes geometrically-varied propulsors to provide purposefully-designed integration benefits [13]. Examples of distributed propulsion in the context of fixed wing aircraft include distributed jets, where a jet sheet is ejected from a slot at or near the trailing edge of a wing, and multiple propulsors placed along a portion of or the entirety of a wing. One of the advantages of distributed propulsion systems is the ability to closely incorporate propulsors into the wing and body surface of an aircraft, resulting in various types of aero-propulsive coupling. In general, multiple aero-propulsive benefits of distrubted propulsion systems have been found to exist. For example, certain vehicle configurations can achieve propulsive efficiency benefits due to boundary-layer ingestion [14]. In addition, reductions in vehicle drag can be achieved through a variety of mechanisms, including wake filling and vortex suppression. Finally, the use of multiple spanwise propulsors provides an additional means of vehicle control not available to conventional configurations.

One example of a distributed propulsion concept being studied is turboelectric distributed propulsion, which involves the use of traditional gas turbines to provide electric power to multiple, distributed, electric fans [15]. The concept is motivated by the ability of many small fans to achieve a high effective bypass ratio without compromising the efficiency of large gas turbine engine cores. Another example of distributed propulsion can be seen in the NASA X-57 Maxwell aircraft, which utilizes multiple electrically driven propellers mounted on the leading edge of a wing in addition to propellers mounted on the wing tips for cruise [16]. The distributed propellers substantially increase the dynamic pressure across the wing at low speeds, allowing for the use of a smaller area, higher aspect ratio wing that is more efficient in cruise than a conventional wing without a loss in take off and landing performance [4]. Multiple novel aircraft configurations which utilize various forms of distributed propulsion have been designed and built in the emerging electric vertical take off and landing (eVTOL) industry, such as those built by Joby and Lilium. An operational advantage afforded by the use of multiple propulsors is redudancy, which can be an important factor from a safety perspective.

There also exists a significant body of work pertaining to distributed propulsion systems comprised of ducted fans integrated into wing sections. An example of this is the numerical, parametric

study of a variety of integrated ducted fan and airfoil configurations performed by Wick, which identified the potential for increased propulsive efficiency over conventional podded propulsive configurations [17]. In addition, experimental characterizations of the aero-propulsive coupling effects of an array of electric ducted fans integrated on an airfoil upper surface trailing edge were conducted by Rolling Hills Research Corporation and the University of Illinois at Urbana-Champaign [5, 18].

1.2 Research Objective

The fundamental mechanisms behind powered lift systems are well-understood for a wide subset of aero-propulsive configurations, such as jet augmentor wings and blown flaps. Although it is known that the presence of a high-momentum wake near a wing can increase circulation and support a pressure load beyond the physical limits of the wing, these characteristics have not been extensively studied on novel systems such as distributed propulsion systems comprised of multiple fans, which also exhibit aero-propulsive coupling. Given the proximity of the propulsors to wing surfaces in many distributed propulsion configurations, these systems could potentially exhibit unique aero-propulsive effects under the right conditions. Applying thrust vectoring to a distributed propulsion system could provide a means of modifying the high-momentum wake to modulate the aero-propulsive characteristics of the system.

The objective of this study was to identify the aero-propulsive characteristics of an overing distributed electric propulsion system with vectored thrust. Wind tunnel testing was performed on an airfoil model fitted with a DEP system in order to determine the aero-propulsive effects induced on a distributed propulsion system with the use of thrust vectoring. An S8036 airfoil model was fitted with a DEP system comprised of five ducted fans along the upper surface of the trailing edge. Stream-wise and stream-normal forces, as well as quarter-chord pitching moment data for the model, were acquired as a function of angle of attack, fan tip speed ratio, and nozzle deflection angle. Surface pressure data were also collected across the radial domain of the center fan to investigate the circulatory effects of the system as well as spanwise variations in wing sectional performance.

Chapter 2

Experimental Method

2.1 Testing Environment

2.1.1 Wind Tunnel

All experiments were performed at the University of Illinois in an open-circuit type, low-speed wind tunnel with a 2.8-ft tall, 4-ft wide, and 8-ft long test section shown in Fig. 2.1. The tunnel inlet is equipped with a 4-inch honeycomb, which is followed by four anti-turbulence screens that maintain a turbulence level (Tu) of below 0.1%. The contraction ratio between the end of the settling section and the start of the test section is 7.5:1. The test section height is constant throughout its length, and the width increases 0.5 inches on each side to account for boundary layer growth. The wind tunnel fan is located at the end of the diffuser section and is driven by a 125-horsepower AC motor controlled by an ABB ACS800 Low Voltage AC variable frequency drive.

Test section dynamic pressure, q_∞, and freestream velocity, U_∞, were determined with the assumption of incompressible flow using the conservation of mass (2.1a) and Bernoulli's equation (2.2). Assuming constant density, the continuity equation can be rearranged to obtain an expression (2.1b) for the the velocity at the settling section, U_{ss}, in terms of the cross sectional areas of each section, A_{ss} and A_{ts}, and the velocity at the test section, U_{ts}. This expression for U_{ss} can then be substituted into the Bernoulli equation (2.2), resulting in an equation for U_{ts} (2.3) in terms of static pressures P_{ss} and P_{ts}, test section freestream density, ρ_∞, and the areas of each section. For

the purposes of this study, the test section velocity, U_{ts}, was defined as the test section freestream velocity, U_∞.

$$\rho_\infty A_{\text{ss}} U_{\text{ss}} = \rho_\infty A_{\text{ts}} U_{\text{ts}} \tag{2.1a}$$

$$U_{\text{ss}} = \frac{A_{\text{ts}}}{A_{\text{ss}}} U_{\text{ts}} \tag{2.1b}$$

$$\frac{1}{2}\rho_\infty U_{\text{ss}}^2 + P_{\text{ss}} = \frac{1}{2}\rho_\infty U_{\text{ts}}^2 + P_{\text{ts}} \tag{2.2}$$

$$U_\infty = U_{\text{ts}} = \sqrt{\frac{2\left(P_{\text{ss}} - P_{\text{ts}}\right)}{\rho_\infty\left(1 - \left(\frac{A_{\text{ts}}}{A_{\text{ss}}}\right)^2\right)}} \tag{2.3}$$

Four static pressure ports located just behind the turbulence screens provided static pressure measurements of the settling section, P_{ss}, and four pressure ports located at the entrance of the test section provided static pressure measurements of the test section, P_{ts}. Each set of pressure ports are manifolded to a single output, providing an average pressure value for each location. The freestream density, ρ_∞, was assumed to be equal to the ambient density, which was calculated using ideal gas law (2.4) based on ambient pressure and temperature. Ambient pressure, P_{amb}, was measured using a Setra 270 absolute pressure transducer, and temperature, T_{amb}, was measured using a National Instrument Type-J thermocouple.

$$\rho_\infty = \frac{P_{\text{amb}}}{R T_{\text{amb}}} \tag{2.4}$$

For the current study, a wood ceiling fitted with two reinforcing steel channels on the outside surface was used. Bolts were inserted through a steel beam that spanned the wind tunnel frame and fastened to slot nuts in the ceiling channels. This configuration allowed an upward residual force to be applied to the wood ceiling, which was applied against inwards bowing in the center of the ceiling due to decreased section static pressure at high Reynolds numbers. The reinforcement of the ceiling was set by running the wind tunnel at a Reynolds number of 1.8×10^6 and tightening the bolts enough to produce a small gap between the ceiling and the wind tunnel model.

2.1.2 Reynolds Number Control

Data were collected for the current study at multiple tunnel Reynolds numbers. The chord based Reynolds number of the test section, Re_c, was calculated based on the airfoil model chord, c, using the following equation:

$$Re_c = \frac{\rho_\infty U_\infty c}{\mu} \tag{2.5}$$

Where U_∞ is the test section freestream velocity, ρ_∞ is the ambient air density, and μ is the dynamic viscosity of air. An iterative LabView routine that commanded the wind tunnel fan RPM based on measured test section Reynolds number was used prior to force and pressure data acquisition at each model angle of attack, α, in order to achieve a target Reynolds number within a 0.5% tolerance. The purpose of this iterative routine was to ensure that the RPM of the wind tunnel fan was sufficient in achieving the desired Reynolds number at each angle of attack, given that changes in model incidence produced different amounts of tunnel blockage.

It should be noted that during the experiments, the EDFs of the vectored DEP system were given a low, "idle-throttle" command whenever data were not being collected. This approach was taken since the EDFs are battery-powered, and the battery capacities were not sufficient to power the EDFs for the entire duration of the experiment at the throttle percentages required at each data point. Operating the EDFs at a low throttle without turning them completely off conserved power while avoiding expending additional power starting the fans back up from a fully windmilling state. As a result, the Reynolds number of the test section during data acquisition varied from the target Reynolds number in amounts dependent on model angle of attack and EDF RPM. The EDF test parameters, which are discussed in Section 3.2, were chosen both in terms of EDF RPM, ω, and tip speed ratio, λ, in order to account for this variation. The effects of the DEP system on Reynolds number are discussed in Section 3.2.2.

2.2 Quasi-2D DEP Airfoil Model

2.2.1 Airfoil Model & Construction

An S8036 airfoil model with a removable 25% trailing-edge flap element, an 18 inch chord, and a 33.6 inch span was used for the present study. The airfoil model had been designed with a modular capability, where segments of the airfoil could be interchanged to accommodate active flow control devices. In its baseline configuration, the airfoil model was equipped with a 25% simple flap which follows the surface contour of the original airfoil profile. Shown in Fig. 2.2(a) is the airfoil model with a row of active flow control devices installed in the upper surface as well as the 25% simple flap. For the vectored DEP experiment, a separate fixed-angle flap element was designed with a series of EDFs housed in nacelles integrated across the upper surface trailing edge region. All major structural components of the model were 3D printed using a stereolithography (SLA) process. The airfoil model with the vectored DEP element installed is shown in Fig. 2.3, which also shows the pressure measurement and EDF power system instrumentation outside of the wind tunnel.

Two steel structural spars extend from within the airfoil out of the wind tunnel wall through a base plate with cutouts for the spars. Each flap element also contains an aluminum structural spar which extends from within the element out of the wind tunnel. Each spar was secured to the cruciform mounting plate of a three-component force balance using steel L-brackets. The spar of the 25% simple flap element was designed such that the flap could be secured at a range of discrete flap deflection angles, δ_f, measured downwards from the airfoil chord line, whereas the spars of the airfoil and vectored DEP flap element were mounted at a fixed orientation relative to the force balance.

A total of 69 surface pressure taps were incorporated into the airfoil in three chord-wise rows. Each surface pressure tap in the airfoil and the flap elements was routed internally through the model as a closed channel to an internal, accessible interface surface where it terminated as a hole. Individual steel tubes were inserted into the holes and sealed with epoxy resin to provide an interface for vinyl tubing, which connected the surface pressure taps to pressure measurement

devices. The rows of taps were spaced 1 inch apart, with the center row placed at the mid-span of the model. During installation of the model, a pressure tap became blocked. It was located at the normalized position $(x/c, y/c, z/b) = (0.5, -0.0575, 0.47)$ in the reference frame with x in the chord axial direction, y in the chord normal direction, z in the spanwise direction, and the origin at the model root leading edge. No pressure data were collected for that blocked tap. For plotting purposes, pressure data for the blocked tap were interpolated from the two neighboring taps of the same row.

2.3 Vectored DEP Flap Element

2.3.1 Flap Element Construction

The DEP system was comprised of a fixed-angle flap element to which a row of five individual nacelles containing EDFs was mounted. The nacelles, which are shown in Fig. 2.5 as CAD renderings, were designed with removable aft fairings so that nozzles with different deflection angles of EDF efflux measured downwards from the chord line, δ_T, could be installed and tested. The nacelles were arranged in a spanwise row, with simple end-cap covers mounted on each spanwise edge of the array, as seen in Fig. 2.2(b).

A VTOL aircraft of lift + cruise configuration was conceptualized to motivate the sizing of the EDFs and design of the nacelle. It was assumed that such an aircraft would generate thrust for vertical flight using vertical lift propulsors and a vectorable DEP system mounted on the upper surface of the wing trailing edge. Therefore, the EDFs were sized to be slightly larger than those found on a typical fixed-wing DEP system designed for conventional takeoff and landing operations and cruise. The vectoring of the DEP system in the current approach allows the forward thrust propulsors to be vectored as a complement to vertical lift propulsors in order to reduce the theoretical disk loading of the VTOL propulsion system for the motivating aircraft. Past examples of cruise-only distributed propulsion systems typically utilized propulsors with diameters that range from 10% to 22% wing chord [19, 20, 17]. Among the commercially available EDFs that most closely met this criteria, the Schubeler Technologies DS-51-AXI HDS 90 mm EDF driven by an

HET 700-68-1400 motor was selected. This EDF produced a ratio between fan diameter and chord of 19.6%.

Each nacelle was comprised of a rectangular inlet leading to a circular duct containing an EDF and an aft fairing that blends into the rectangular profile of the nacelle. The upper lip of the nacelle inlet was configured based on physical constraints and the desire to provide an aerodynamically-efficient design for the simulated nominal cruise case. The leading edge of the upper lip was taken from the leading edge of a 10.6% thick airfoil, the Eppler 212. This configuration was chosen in order to maintain a low frontal profile at the cruise condition. Approximately 1.25 inches of thickness above the fan was allotted to internally route wires and pressure tap tubing out of the wind tunnel. This space was also considered representative of that required to stow the mechanical components of a thrust vectoring mechanism in the motivating DEP system. Cross sectional views of the nacelle and aft fairing are shown in Fig. 2.6.

The chordwise position of the EDFs was set at $x/c = 0.82$ for structural considerations and to ensure that the EDF exits were as close as possible to the original airfoil trailing edge. This position was also selected to allow a greater pressure recovery to occur across the airfoil surface before being ingested into the EDF inlet. As will be shown in Section 3.3, this configuration effectively ensured that the a value of $C_p = 0$ was nominally reached across the inlet when the DEP system was operational, indicating that the inviscid flow region was not significantly accelerated beyond the freestream velocity.

Vectored thrust was achieved via a constant area, tubular nozzle with the same diameter as the EDF. This nozzle was swept to varying degrees along an arc emanating from the fan center line with an origin at the lower edge of the fan exit. The tubular nozzle and aft fairing were designed as one piece. Thrust deflection angles of $\delta_T = 5.19°, 30°, 45°, 60°$, and 90° were 3D printed and tested. It should be noted that the $\delta_T = 5.19°$ case corresponds to no amount of thrust vectoring and is a result of the installed angle of the EDFs into the airfoil upper surface. Images of the aft fairings with the 30°, 45°, and 90° nozzles are shown in Fig. 2.7. Channels or slots for routing wires and accessing screws were sealed using a thin adhesive covering during testing.

The airfiol model and flap element had three chordwise rows of pressure taps installed at y/b = 0.47, 0.50, and 0.53. The nacelles housing the EDF array were installed such that the centerline

of the middle nacelle was aligned with the y/b = 0.47 location. The DEP flap element contained a total of 24 pressure taps. The locations of the main element and DEP flap element taps are shown in Fig. 2.9. The spanwise locations of the three rows of taps correspond to planes at locations measured relative to the center-fan centerline in the outboard direction of y/R = 0, 0.57, and 1.14. This approach ensured that the spanwise pressure variation across the full radius of the center EDF could be obtained and that moments caused by the vertical offset of the EDFs from the force balance were minimized.

2.3.2 Power System

Each EDF was driven by a brushless direct current (BLDC) motor, which must be driven by a 3 phase power source. Electronic speed controllers (ESC) are able to control the speed and torque of a motor by inverting a supplied direct current power source and varying the frequency of the phases. A Castle Creations Phoenix Edge Lite 160 Amp ESC was used to drive each EDF. Two of the ESCs can be seen sitting on a table under the tunnel test section in Fig. 2.4. Direct current (DC) power was provided to each ESC in the form of two Turnigy 5000mAh 14.8V 20C lithium polymer batteries connected in series, providing up to 33.6 Volts of DC power when fully charged. Based on power measurements during full throttle operation in static conditions provided by the manufacturer, which are shown in Fig. 2.8, the maximum possible current draw of a single EDF was expected to be approximately 75 Amps. For a majority of the experiments, the EDFs were operated at lower throttle settings in order to conserve battery capacity. Based on the anticipated continuous current draw of an EDF during experiments, an ESC with a much higher current rating (160 Amps) was chosen. For safety and ESC calibration purposes, switches were added between each set of batteries and corresponding ESC. The switches, which are shown in Fig. 2.3, provided an ability to power the ESCs on and off quickly and simultaneously.

2.4 Data Acquisition System

Data from the wind tunnel, airfoil model, and vectored DEP system were collected through subroutines and virtual instruments within a single LabView program running on a Dell Precision T3400 computer. This program was also used to control all aspects of the experiment, including

the wind tunnel Re_c as discussed in Section 2.1, airfoil model angle of attack, and individual EDF throttle settings. The data collection process was conducted through a LabView program by repeating the following procedure for a prescribed set of angles of attack:

1. Command force balance to a prescribed α
2. Execute Re_c control subroutine to adjust Re_c to set value
3. Execute ω or λ control subroutine to command EDFs to the set condition
4. Wait 10 seconds to allow the flow to settle
5. Collect time averaged force balance data
6. Collect time averaged pressure measurements
7. Command EDFs to idle throttle percentage until next ω or λ command

After the final data had been collected, the model was returned to $\alpha = 0^\circ$ and the EDFs were given a 0% throttle command. The commanded tunnel fan RPM remained at the the set value from the previous data point until the user provided a final shut down command. This was to allow the freestream flow to cool the EDF motors.

2.4.1 Time Averaged Balance Measurements

The airfoil model was mounted to an Aerotech three-component load cell balance located underneath the wind tunnel test section. The balance, which was integrated into an automated turntable for adjusting the airfoil model angle of attack, provided airfoil normal and axial forces as well as pitching moment. The load cells of the balance produced analog voltage signals corresponding to normal force, F_N, axial force, F_A, and pitching moment, M, in a range of ±20 mV. These signals were then passed through a signal processor which could be adjusted to improve the signal-to-noise ratio for three intervals of loading conditions, as shown in Table 2.1. The signal processor also served as a 1 Hz low-pass filter and re-scaled the signal to a nominal range of ±5 V, which improved the digitization of the analog signal. Based on the anticipated loads of the airfoil model with the vetored DEP system, the signal processor was set to the 'High' setting for all three components. The raw voltage signals for F_N, F_A, and M were digitized and converted to force measurements using the following calibration matrix provided by the balance manufacturer:

$$\begin{pmatrix} F_N \\ F_A \\ M \end{pmatrix} = \begin{pmatrix} 37.7 & 0.03159 & -0.2095 & 0.01094 & 0 & -0.00865 \\ -0.1607 & 8.3125 & -0.01638 & 0.007084 & 0 & 0.007660 \\ -0.01299 & -0.005521 & 1.247 & -0.002122 & 0 & 0.0001497 \end{pmatrix} \begin{pmatrix} v_N \\ v_A \\ v_M \\ v_N^2 \\ v_A^2 \\ v_M^2 \end{pmatrix} \tag{2.6}$$

Where v_N, v_A, and v_M are the measured normal force, axial force, and pitching moment voltage signals. The pitching moment about the quarter chord, $M_{c/4}$, was calculated from the pitching moment using the offset of the airfoil quarter chord, $(X_{c/4}, Y_{c/4})$, from the balance center:

$$M_{c/4} = M - X_{c/4}F_N + Y_{c/4}F_A \tag{2.7}$$

Stream normal and stream axial force of the model were calculated by rotating the measured airfoil normal and axial forces into the wind axis. This was achieved through a two-dimensional coordinate frame rotation using the angle of attack, α:

$$L = F_N \cos(\alpha) - F_A \sin(\alpha) \tag{2.8}$$

$$D = F_N \sin(\alpha) + F_A \cos(\alpha) \tag{2.9}$$

Where lift, L, is the total stream normal force and drag, D, is the total stream axial force. The nondimensionalized coefficients of lift, drag, and quarter chord pitching moment, C_l, C_d, and C_m, were calculated by nondimensionalizing each quantity based on the conventional definition, as shown in the following equations:

$$C_l = \frac{L/b}{\frac{1}{2}\rho_\infty U_\infty^2 c} \tag{2.10}$$

$$C_d = \frac{D/b}{\frac{1}{2}\rho_\infty U_\infty^2 c} \tag{2.11}$$

$$C_m = \frac{M_{c/4}/b}{\frac{1}{2}\rho_\infty U_\infty^2 c^2} \tag{2.12}$$

Where b is the airfoil model span and c is the model chord. It should be noted that although the traditional lift and drag nomenclature is used for the stream normal and stream axial forces, the presented values include the effects of thrust from the DEP system, which traditional definitions of lift an drag do not include. For each data point, time histories of the lift, drag, and quarter chord pitching moment were collected, and the average value was recorded for that angle of attack.

2.4.2 Time Averaged Pressure Measurements

The static pressure at each surface pressure tap of the model was measured using multiple electronic differential pressure measurement units. For the present study, the test section static pressure, which was equivalent to the freestream static pressure, was used as the reference for measuring pressure differentials. Based on the number of taps and the anticipated surface pressures of the vectored DEP system, three Esterline ESP-32 HD miniature differential pressure scanners were needed. Each pressure scanner contained an array of 32 piezo-resistive sensors connected in a Wheatstone bridge configuration, allowing for the precise measurement of pressure differentials within a certain range. Two pressure scanners with a measurement range of ±1.0 psid and one pressure scanner with a measurement range of ±5.0 psid was used. Surface pressure taps located in regions with higher potential differences from the freestream static pressure, such as the aifoil and nacelle leading edge, were connected to the ±5.0 psid pressure scanner. Fig. 2.4 shows the wooden box below the tunnel test section in which the pressure scanners were placed, as well as the pressure tubing that was routed out of the model and to the pressure scanners.

Pressure differential signals in the form of voltages from the pressure scanners were acquired through a Digital Temperature Compensation (DTC) Initium Data Acquisition System. The voltage signals were sampled at a rate of 50 Hz and then converted into pressure measurements using a 6^{th} order temperature-compensated calibration curve provided with the DTC Initium system. Pressure measurements were taken as the average value over a 2 second time period. Coefficient of

pressure (C_p) data were subsequently calculated based on the measured pressure differentials and freestream dynamic pressure according to the standard definition of C_p:

$$C_p = \frac{P - P_\infty}{q_\infty} \tag{2.13}$$

Where P is the static pressure at the pressure tap, P_∞ is the freestream static pressure, and q_∞ is the freestream dynamic pressure.

2.4.3 EDF Instrumentation & Control

Most hobby-grade ESCs, including the model used for the present study, are controlled through a pulse-width-modulation signal, where a pulse width of 1.1 ms corresponds to a minimum throttle input and a pulse width of 1.9 ms corresponds to a maximum throttle input. In addition, many hobby-grade ESCs require a calibration procedure in order to correctly associate PWM signals with the maximum and minimum throttle settings. For the ESCs used in this experiment, the calibration procedure consists of powering on the ESCs while sending the PWM signal to be associated with full throttle, waiting three seconds, and then sending the PWM signal associated with minimum throttle. A LabView routine was written to perform this calibration procedure prior to each experiment.

PWM signals based on percent throttle settings in the LabView program were generated through a National Instruments PCI-6602 Counter/Timer Board and sent to each ESC. ESCs drive BLDC motors in response to throttle commands by varying the frequency at which power is supplied to the electromagnetic stators of the motors. Although the frequency of the phased power sent to the motor can be accurately controlled by throttle commands to the ESC, the resultant motion of the motor depends on the magnetic forces between the magnetic rotors and stators and the torque load on the shaft. Therefore, variation in the voltage of DC power supplied to the ESC can lead to variation in motor RPM for a constant throttle command. In addition, physical and environmental factors such as the fan blade moment of inertia about the rotation axis and aerodynamic drag of the blades can affect the torque load experienced by the motor and subsequently, the RPM. As a result, a feedback control system is necessary to control EDFs to a specific RPM or tip speed ratio.

The RPM of each EDF was measured using an Eagle Tree brand, brushless motor RPM sensor. Each sensor was powered using four 1.5V AA batteries in series and measured the voltage difference between two of the three wires connecting each ESC to the EDF motor. A pulsed, analog voltage signal from the back electromagnetic force caused by the rotation of the rotors was read from the sensors using a sampler operating with a Nyquist frequency well above the highest achievable RPM of the EDFs in the present configuration. The RPM of the EDFs was then calculated based on the proportional relationship between RPM, the frequency of back EMF variation, and the number of magnetic rotors, or poles, in the motor. The tip speed ratio, λ, of each EDF was also calculated using the equation:

$$\lambda = \frac{\pi D_f \omega / 60}{U_\infty} \tag{2.14}$$

Where D_f is the EDF diameter, ω is RPM, and U_∞ was calculated from measured properties as discussed in Section 2.1.1. A proportional-integral-derivative controller in the LabView program was implemented to be capable of controlling the EDFs to a target RPM or tip speed ratio within a specified tolerance. During RPM control, a tolerance of around 200 was used, and during tip speed ratio control, an equivalent λ tolerance was calculated based on the target freestream velocity. The wires used to send PWM commands, those used to receive ω information, and those used to power the motors can be seen in the photo of the region below the tunnel test section in Fig. 2.4.

2.5 Wind Tunnel Corrections

In order to account for the presence of finite distance solid wall boundaries surrounding the airfoil models, standard data corrections for 2D wind tunnel testing as described by Barlow et al [21] were applied to the collected performance data. These corrections, which are based on the assumption of incompressible flow, account for effects due to three phenomena: solid blockage, wake blockage, and streamline curvature.

Solid blockage refers to the presence of a physical model in the wind tunnel, which reduces the cross-sectional area of the test section. This slight reduction in cross sectional area results in a slight increase in the test section freestream velocity due to the conservation of mass flow

rate, as illustrated in the continuity equation (2.1b) for low speed, incompressible flows. Wake blockage has a similar effect on the test section flow, although it occurs due to the presence of lower-than-freestream velocity flow in the wake of a model. This reduction in velocity for a portion of the overall flow leads to an increase in the surrounding freestream flow in order for preserve the continuity condition. The increases in velocity due to solid and wake blockage can lead to an over-prediction of variables containing velocity in the denominator, such as C_l, C_d, and $C_{m_{c/4}}$. The method outlined by Barlow corrects for these effects by defining the solid blockage velocity increment, ϵ_{sb}, wake blockage velocity increment, ϵ_{wb}, and total velocity increment:

$$\epsilon = \epsilon_{sb} + \epsilon_{w}b \tag{2.15}$$

Which are subsequently used to correct C_l, C_d, $C_{m_{c/4}}$, and C_p data. The solid blockage velocity increment, ϵ_{sb}, can be calculated for a 2D model by representing it with a series of doublets and calculating the induced velocity at the tunnel walls. A simpler approximation of this model is:

$$\epsilon_{sb} = \frac{K_1 V_m}{C^{3/2}} \tag{2.16}$$

Where K_1 is a parameter based on the airfoil configuration, C is the empty test section cross sectional area, and V_m is the airfoil volume. In the present study, the airfoil volume was approximated using the following equation:

$$V_m = \frac{3}{4}tcb \tag{2.17}$$

Where t is the thickness in percent chord and b is the span of the airfoil model. The wake blockage velocity increment, ϵ_{wb}, can also be calculated using potential flow elements. The wake can be represented using a source at the model trailing edge and a sink far downstream, and the tunnel walls can be represented as a series of source-sink combinations. The resulting velocity increment can then be found to be:

$$\epsilon_{wb} = \frac{1}{2}\frac{c}{h}C_{d,u} \tag{2.18}$$

Where $C_{d,u}$ is the uncorrected value of the airfoil drag coefficient.

Streamline curvature effects refer to those resulting from an artificial camber imposed on an airfoil model due to the inability for streamlines to pass through the solid tunnel wall boundaries. This effect can be accounted for with an empirically derived variable, σ, defined as:

$$\sigma = \frac{\pi^2}{48}\left(\frac{c}{h}\right)^2 \tag{2.19}$$

Using the incremental velocity terms and the empirically derived streamline correction factor σ, corrected values for angle of attack, C_l, C_d, $C_{m_{c/4}}$, and C_p were calculated using the following equations:

$$\alpha_{cor} = \alpha_u + \frac{57.3\sigma}{2\pi}\left(C_{l,u} + 4C_{m,u}\right) \tag{2.20}$$

$$C_{l,cor} = C_{l,u}(1 - \sigma - 2\epsilon_{wb}) \tag{2.21}$$

$$C_{d,cor} = C_{d,u}(1 - 3\epsilon_{sb} - 2\epsilon wb) \tag{2.22}$$

$$C_{m,cor} = C_{m,u}(1 - 2\epsilon) + \frac{1}{4}\sigma C_{l,u} \tag{2.23}$$

$$C_{p,cor} = \frac{C_{p,u}}{(1+\epsilon)^2} \tag{2.24}$$

2.6 Chapter 2 Table and Figures

	High	Medium	Low
F_N	±450 lbs	±225 lbs	±90 lbs
F_A	±90 lbs	±55 lbs	±18 lbs
M	±45 ft-lbs	±30 ft-lbs	±15 ft-lbs

Table 2.1: Load ranges for which voltage signals from the balance can be processed

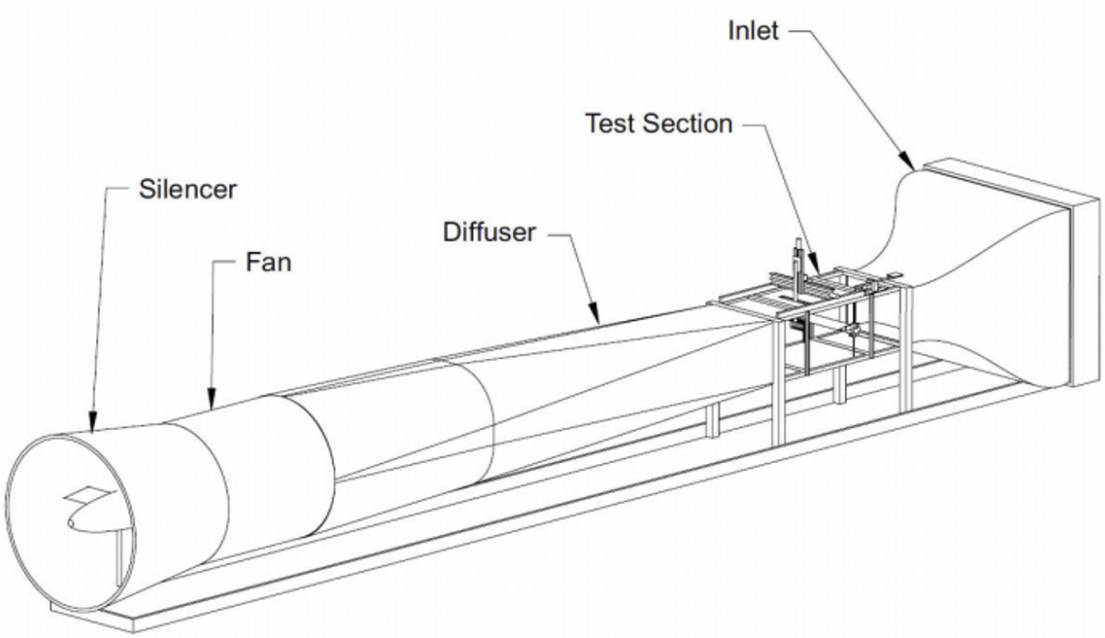

Figure 2.1: Schematic of the $3' \times 4'$ low speed tunnel at UIUC

(a) S8036 airfoil with a spanwise array of active flow control actuators and simple 25% flap installed

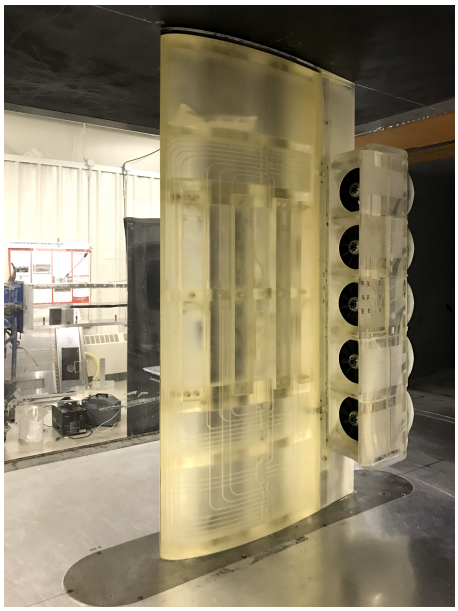

(b) S8036 airfoil with installed DEP system and no flow control devices installed

Figure 2.2: S8036 airfoil model with (a) original flap and (b) modified DEP flap.

Figure 2.3: Photo of the airfoil model installed in the wind tunnel and subsystems outside of the tunnel

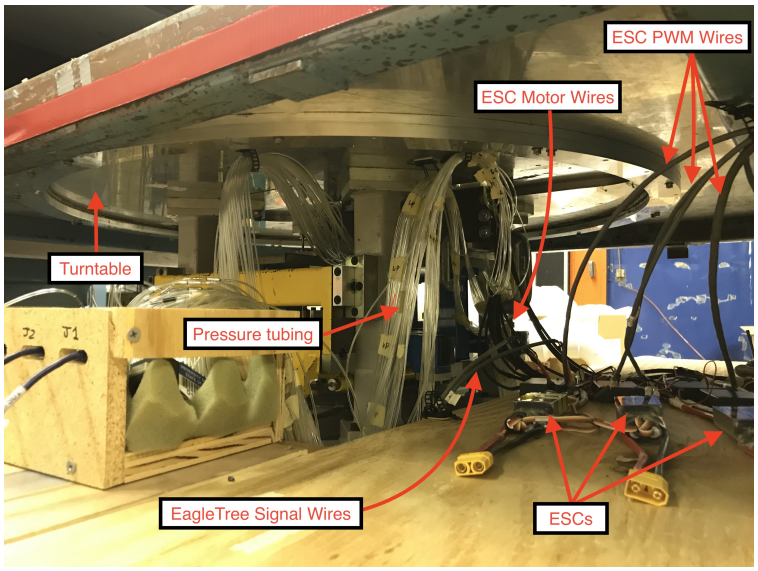

Figure 2.4: Photo of the region directly below the tunnel test section showing the turntable, EDF power system, and pressure measurement system

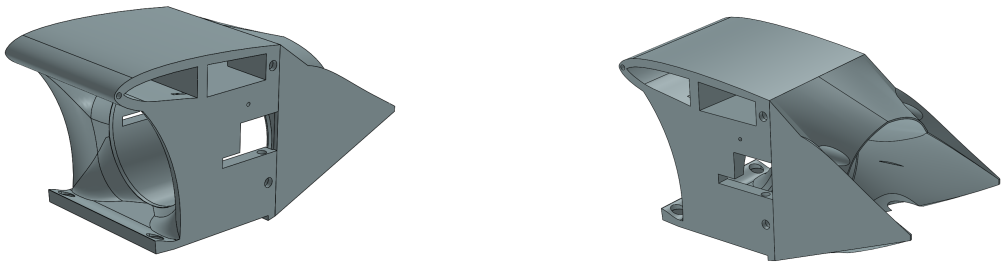

(a) Front view of nacelle and aft fairing

(b) Rear view of nacelle and aft fairing

Figure 2.5: CAD renderings of the nacelle and aft fairing without side covers.

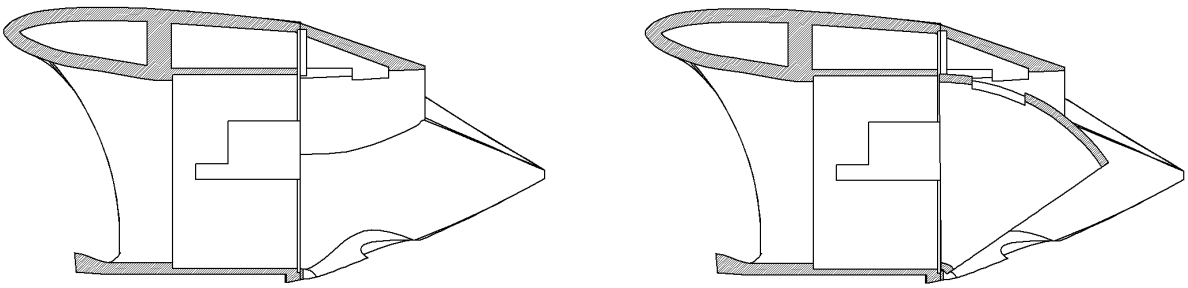

(a) Nacelle with 5.19° aft fairing nozzle

(b) Nacelle with 60° aft fairing nozzle

Figure 2.6: Diagram of nacelle and nozzle centerline cross sections for various nozzle configurations.

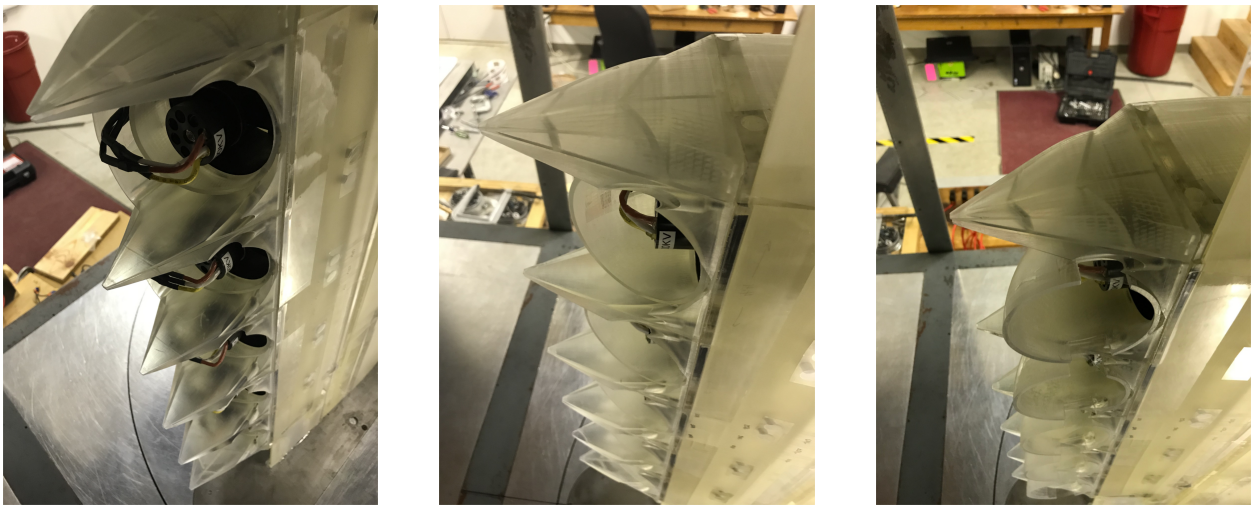

(a) 30° aft fairing nozzle (b) 45° aft fairing nozzle (c) 90° aft fairing nozzle

Figure 2.7: Images of the DEP airfoil model with various versions of the aft fairing installed

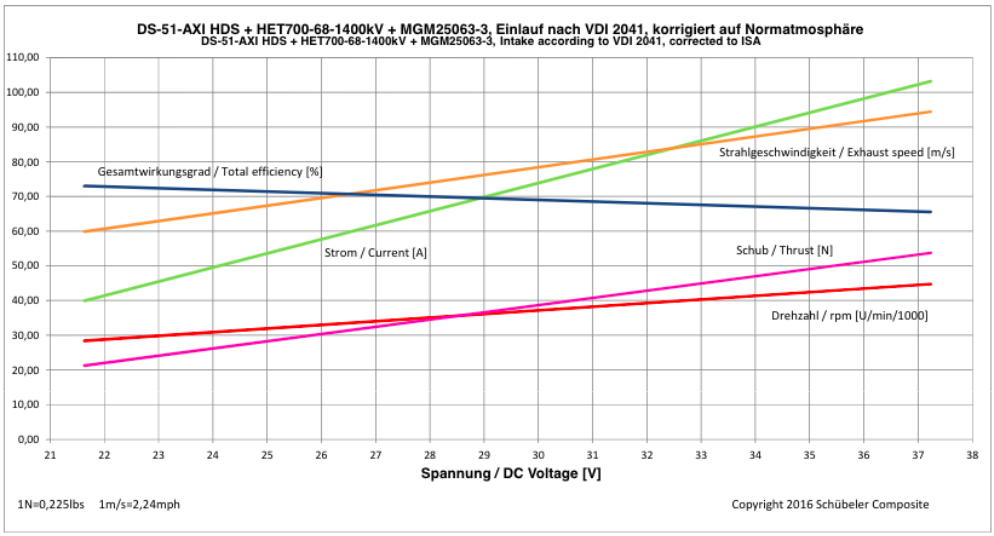

Figure 2.8: EDF performance data taken at static conditions provided by Schubeler Technologies

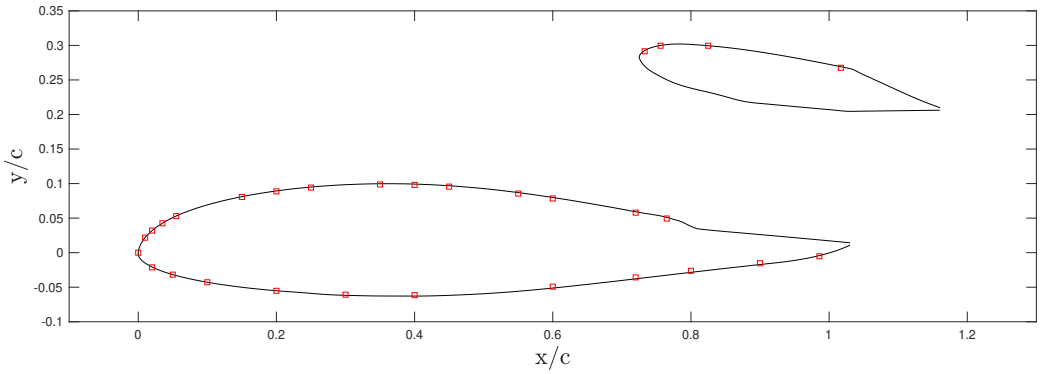

Figure 2.9: Locations of pressure taps contained in one chordwise row for the main airfoil element and DEP element

Chapter 3

Results

3.1 S8036 with Simple Flap Baseline Performance

Prior to testing the vectored DEP system, baseline force and moment coefficient data were obtained for the S8036 airfoil with a 25%-chord simple flap. Validation data were acquired for this configuration at $Re_c = 0.5 \times 10^6$ in order to assess the overall data quality produced by the wind tunnel model and associated installation. The associated comparisons to historical data [22] are shown in Fig. 3.1, where it should be noted that the results were not corrected for solid blockage, wake blockage, or streamline curvature, as these corrections were not included in the reference data. From the acquired results, it can be seen that the airfoil performance matched the historical data well. However, an additional contribution of excrescence drag can be observed in the current installation. The current wind tunnel model was designed to have a modular capability, where segments of the airfoil could be interchanged to accommodate a variety of active flow control and aero-propulsive configurations. This modularity led to the presence of very small seams in the surface and a slightly higher drag coefficient for the airfoil, though this variation was deemed to be inconsequential for the current study since changes in the stream-wise force coefficient brought about by the DEP system were multiple orders of magnitude greater than this excrescence drag contribution. While omitted here, it should be noted that standard corrections for acquired measurements are included in all subsequent performance data reported.

The configuration of the wind tunnel model with a 25%-chord simple flap allowed for it to be used as a baseline for studying the effects of the vectored DEP system. Lift, drag, and

pitching moment data, as well as pressure data, were acquired for the wind tunnel model in this baseline configuration for a range of flap deflection angles, δ_f, at a chord-based Reynolds number of $Re_c = 1.0 \times 10^6$. As anticipated, the force and moment data, shown in Fig. 3.2, indicated that the wind tunnel model exhibited performance characteristics consistent with airfoils with simple flaps. Linear increases in flap deflection from $\delta_f = 0^\circ$ to 20° can be seen to produce consistent increases in maximum lift coefficient, $C_{l_{\max}}$, and decreases in the zero lift angle of attack. Associated with this increase in lift is an expected increase in drag, as seen in Fig. 3.2b. Increased flap deflection can also be seen to result in an overall downwards shift in the C_m curve.

Airfoil and flap pressure distributions at $\alpha = 4^\circ$ and 10° for a range of flap deflections are shown in Fig. 3.3. An increase in airfoil circulation can be observed from the overall decrease in pressures on the airfoil and flap upper surfaces and increase in pressure on the airfoil and flap lower surfaces with increased flap deflection. This observation is most notably made through the growth of the leading-edge suction peak with increased flap deflection. The regions of constant pressure over the upper surface of the flap, such as that observed for $\delta_f = 10 - 20^\circ$ at $\alpha = 4^\circ$ and $\alpha = 10^\circ$, indicate the presence of separated flow.

3.2 Vectored DEP Steady Performance

3.2.1 Static Thrust Performance

Force balance measurements were initially taken for each nozzle case under static conditions to quantify the thrust performance of the system. Forces in the chord-normal and axial directions, F_n and F_a, were measured for a range of EDF RPM values. It should be noted that although thrust force in the forward and chord-normal directions were defined as positive for the static thrust measurements, this is different from the convention used for analyses of the DEP system, which utilizes canonical stream-normal and stream-wise conventions aligned with the freestream wind axes. The values of normal and axial thrust force were non-dimensionalized using the fan tip speed (V_{tip}) and total swept area (A_{fans}) of all 5 fans as shown in Eq. 3.1 and 3.2. An overall thrust coefficient, C_T, was calculated using the normal and axial forces as shown in Eq. 3.3 to examine thrust performance and losses due to vectoring.

$$C_{T_a} = \frac{F_a}{\frac{1}{2}\rho_\infty V_{\text{tip}}^2 A_{\text{fans}}} \tag{3.1}$$

$$C_{T_n} = \frac{F_n}{\frac{1}{2}\rho_\infty V_{\text{tip}}^2 A_{\text{fans}}} \tag{3.2}$$

$$C_T = \frac{\sqrt{F_n^2 + F_a^2}}{\frac{1}{2}\rho_\infty V_{\text{tip}}^2 A_{\text{fans}}} \tag{3.3}$$

The plots of axial and normal thrust coefficients with respect to thrust deflection angle in Fig. 3.4a and 3.4b align with intuitive expectations for a thrust vectoring system. The axial thrust coefficient, C_{T_a}, is greatest at a thrust deflection angle of $\delta_T = 5.19°$, and the normal thrust coefficient, C_{T_n}, is greatest at a thrust deflection angle of $\delta_T = 90°$. An interesting result was the occurrence of the highest C_T values at a thrust deflection angle of $\delta_T = 30°$. This is largely due to a combination of the relatively small change in axial thrust coefficient and significant increase in normal thrust coefficient between the $\delta_T = 5.19°$ and 30° cases. At lower fan RPMs, the deflection of the thrust to 30° led to a slight increase in the axial thrust coefficient as compared to the $\delta_T = 5.19°$ case, whereas an opposite effect was observed at higher fan RPMs. This unexpected behavior is conjectured to be the result of installation effects associated with the aft fairings and nozzles. As expected, a decrease in the overall thrust coefficient was observed with increased thrust deflection beyond $\delta_T = 30°$ due to greater duct losses. In addition, the nonzero C_{T_a} value for the $\delta_T = 90°$ case indicates that the 90° nozzle did not convert all of the axial momentum in the stream. This was likely due to the relatively short duct length of the 90° nozzle and significant amount of thrust generated by the EDF system.

3.2.2 Reynolds Number Variation

As described in Section 2.1.2, a significant limitation in the collection of aerodynamic performance data was the inability of the DEP system to operate continuously. Prior to data acquisition at each angle of attack, the Re_c control LabView routine converged on a wind tunnel fan RPM to achieve a set Re_c based on the measured test section conditions. However, the test section

conditions during the Re_c control routine did not always reflect those when the DEP system was operating. This is because the EDFs of the DEP system were operated at a near windmilling state during the tunnel Re_c control routine but at thrust-producing RPMs during data acquisition. When operated at prescribed RPMs to acquire test results, the aero-propulsive configuration produced a significantly different pressure loss and associated blockage effect than when the EDFs were operating in a windmill state. Thus, as the blockage imposed by the aero-propulsive model was reduced, the wind tunnel fan was capable of supporting higher volumetric flow rates, resulting in a higher section Re_c.

Tunnel condition and model performance data were collected for the model at angles of attack ranging from $\alpha = -10^\circ$ to 20° in 2° increments for each nozzle deflection angle configuration and a range of target EDF operating points. The test points over which data were collected are summarized in Table 3.1. Test section Re_c from two sets of experiments with a target Re_c of 0.75×10^6 are shown in Fig. 3.5, and test section Re_c from an experiment with a target Re_c of 0.5×10^6 are shown in Fig. 3.6b. The data presented in Fig. 3.5a, 3.6a, and 3.7a were taken from cases with the EDFs controlled to target EDF RPM values, whereas the data presented in Fig. 3.5b and 3.7b were taken from cases with the EDFs controlled to multiple target tip speed ratios.

As expected, the EDFs had an increasing effect on the test section Re_c with increased operating RPM. At the lowest angles of attack ($\alpha < -6^\circ$), increases in fan RPM can be seen to induce proportional increases in Re_c for all δ_T. The magnitude of this effect can be seen to decrease as α increases. At high angles of attack ($\alpha > 16^\circ$), the test section Re_c can be seen to match the target value more closely. However, at the highest angles of attack and the onset of stall, a lower than target Re_c can be seen. Increasing δ_T can be observed to magnify this trend, causing a slight increase in the magnitude of the slope of the Re_c vs. α curves up until $\delta_T = 90^\circ$. This behavior could potentially be attributed to the varying angle between EDF thrust and the negative stream axial direction. However, it can be seen that the same effective angle between EDF thrust and the negative stream axial do not produce the same shift in Re_c. For example, in Fig. 3.6b, Re_c at $\alpha = 16^\circ$ in the $\delta_T = 30^\circ$, $\omega = 30,000$ RPM case was approximately 0.54×10^6, whereas Re_c reached 0.57×10^6 at $\alpha = 0^\circ$ in the $\delta_T = 45^\circ$, $\omega = 30,000$ RPM case. This variation in Re_c for

approximately the same angle between EDF thrust and the negative stream axial direction suggests the relevance of additional factors such as EDF inflow conditions on the effect of EDFs on Re_c.

Although data were collected with the EDFs operated at target RPM values, the significant variation in test section Re_c due to EDF operation motivated the collection of data with the EDFs operated at target tip speed ratios. Fig. 3.7a contains fan tip speed ratio data for the same experiment presented in Fig. 3.5a, which involved constant RPM control. The black lines co-plotted with the fan tip speed ratios represent the calculated tip speed ratio based on the target RPM and Re_c. Variations in tip speed ratio as high as 0.55 can be observed, particularly for lower δ_T cases at high RPM. In the case of ω control, the standard deviation in λ varied both with δ_T and ω. At $\delta_T = 5.19°$, the standard deviation of λ over α at the lowest and highest ω ranged from 0.033 to 0.067. At $\delta_T = 60°$, the standard deviation ranged from 0.077 to 0.20. This variation is in contrast to the tip speed ratio controlled case shown in Fig. 3.7b, which corresponds to the same data presented in Fig. 3.5b. The standard deviation of λ in the λ control case was uniformly on the order of 0.02. As test section Reynolds number varied as a result of EDF operation, the LabView routine controlling fan tip speed ratio adjusted the RPM of the fans to maintain the prescribed tip speed ratio. As will be discussed in the following sections, fan tip speed ratio was a parameter which had a significant effect on the aerodynamic performance of the system. Ensuring a consistent tip speed ratio across angles of attack and variation in Reynolds number provided a more accurate representation of the generalized effects of the DEP system than that from operating at a consistent RPM.

3.2.3 Aerodynamic Performance

Airfoil chord-normal and axial forces, as well as the pitching moment about the airfoil quarter chord, were recorded at the test points listed in Table 3.1. Data were collected for a range of tip speed ratios and thrust deflection angles in order to assess the primary influences of direct momentum addition of the propulsion system and the efflux orientation on airfoil performance. Chord-based Reynolds numbers of $Re_c = 0.5 \times 10^6$ and 0.75×10^6 were chosen in addition to the $Re_c = 1.0 \times 10^6$ used for the baseline airfoil, as the lower associated freestream velocities allowed higher ranges of fan tip speed ratios to be achieved before load limits of the force balance

system were approached. These measurements were non-dimensionalized according to the test section dynamic pressure measured during each test point and reference geometry of the original flapped S8036 model to obtain C_l, C_d, and C_m polars, which are presented in Figs. 3.8, 3.9, 3.10, and 3.11 As stated in Section 2.4.1, it should be noted that traditional lift and drag nomenclature are used for the stream-normal and stream-wise force coefficients even though the measurements included the effects of thrust from the DEP system, which traditional definitions of lift and drag coefficient do not account for. The rated range limits of the pitching moment measurements on the force balance prevented the acquisition of data at certain conditions at each Reynolds number. For the RPM control case at $Re_c = 0.75 \times 10^6$, the limits prevented the acquisition of data for the $\delta_T = 90°$, $\omega = 30,000$ RPM case. For the λ control case at $Re_c = 0.75 \times 10^6$, the limits prevented the acquisition of data at angles of attack greater than 12° in the $\delta_T = 90°$, $\lambda = 5.25$ case. For a Reynolds number of 1.0×10^6, the limits prevented the acquisition of data for the $\delta_T = 60°$, $\lambda = 3.5$, case at angles of attack greater than 16° and the $\lambda = 4.0$ case. Additionally, no data were acquired for the $\delta_T = 90°$, $\lambda = 3.0$ case at angles of attack greater than 2° nor at $\lambda = 3.5, 4.0$. Because the force balance also served as the mounting structure for the model, no model pressure data were collected for those points either. It should also be noted that a noticeable increase in measured C_l was found to occur near and at stall conditions at high EDF ω and λ values during certain test cases which did not match trends from the majority of tests cases. This behavior could be attributed to a combination of significant buffeting of the model in the stalled condition and drastic change in Re_c.

Comparisons of C_l, C_d, and C_m data taken at $Re_c = 0.5 \times 10^6$, 0.75×10^6, and 1.0×10^6 for the windmilling case are shown in Fig. 3.12, and comparisons of data taken at $Re_c = 0.75 \times 10^6$ and $Re_c = 1.0 \times 10^6$ for a tip speed ratio of $\lambda = 3.5$ are shown in Fig. 3.13. It can be seen from both figures that there were minimal differences in force and moment coefficients between data collected at $Re_c = 0.75 \times 10^6$ and 1.0×10^6. However, in the windmill case, a region of decreased C_l and C_m and increased C_d is clearly present at angles of attack ranging from approximately $\alpha = 6°$ to 12° in the $Re_c = 0.5 \times 10^6$ data shown in Fig. 3.12. Similar trends in performance data have been observed historically on airfoils at low Reynolds numbers and have been attributed to transitional effects such as laminar separation bubbles [23]. Surface pressure measurements and further discussion regarding these trends are presented in Section 3.3.

Overall trends that were observed include an expected decrease in C_d with increased tip speed ratio and decreased thrust deflection angle, alongside an increase in C_l due to increased tip speed ratio and nozzle deflection. In addition, the pitching moment was found to uniformly decrease with increased thrust deflection angle, and this effect was significantly magnified with increased tip speed ratio. Although these trends in were evident from data collected at all Reynolds numbers, they are most clear in the $Re_c = 0.75 \times 10^6$ case as a result of the higher achievable tip speed ratios and consistency in performance compared to the 0.5×10^6 case. Therefore, results from data taken at $Re_c = 0.75 \times 10^6$ and 1.0×10^6 were considered separately from those taken at $Re_c = 0.5 \times 10^6$.

3.2.4 Aerodynamic Performance for Tip Speed Ratio Control

The net propulsive thrust of the DEP system is evident in the negative shift of the C_d polars with increasing tip speed ratio at all nozzle deflections except $\delta_T = 90°$. The nonlinear decrease in C_d with respect to proportional increases in tip speed ratio is expected, given that fans are typically designed for a constant C_T, which would by definition scale quadratically with tip speed. In addition, this trend is consistent with past studies regarding airfoils with DEP systems [13]. Another notable phenomenon resulting from increased tip speed ratio is an increase in the lift curve slope, C_{l_α}. These effects of tip speed ratio are slightly reduced by thrust deflection angle, which by contrast was observed to produce a decrease in zero lift angle of attack and a shallower lift curve slope. For the $Re_c = 0.75 \times 10^6$ case shown in Fig. 3.8, at $\delta_T = 0°$ the difference in lift curve slope between the $\lambda = 5.25$ and 0 case is approximately 2 rad^{-1}. When δ_T is increased to 45°, the difference reduces to approximately 1.8 rad^{-1}, and at $\delta_T = 90°$ the difference is 0.64 rad^{-1}. A similar trend is present in the $Re_c = 1.0 \times 10^6$ case shown in Fig. 3.9, although it is less prominent due to the lower tip speed ratios. It is believed that the influence of the circulation produced by the powered wake is primarily responsible for the observed decrease in the zero-lift angle of attack of the airfoil, which becomes more significant as the nozzle deflection angle is increased. Conversely, the variation in the stream-normal force coefficient slope with tip speed ratio is produced due to the momentum-based thrust force contribution of the DEP system, which is expected to scale by $\sin(\alpha)$. It should be noted that in the additional $\delta_T = 5.19°$, $\lambda = 4.0$ and $\delta_T = 45°$, $\lambda = 3.5$ cases of taken at $Re_c = 1.0 \times 10^6$ shown in Fig. 3.9, data were not recorded for the full α range due to an error in the pressure acquisition system used to measure tunnel conditions. This error also

occurred during the collection of the additional data in the $\delta_T = 45°$, $\lambda = 2.5$, 3.5, and 4.5 cases at $Re_c = 0.75\times10^6$. These partial data sets were included to illustrate the repeatability of performance measurements at various Reynolds numbers and EDF control cases.

Both thrust deflection and tip speed ratio were found to have a significant effect on the airfoil pitching moment. At low thrust deflection angles and at high tip speed ratios, increasing the thrust deflection angle resulted in a relatively uniform decrease in the C_m curve, similar to the simple flap case shown in Fig. 3.2c. Increasing tip speed ratio for a fixed nozzle deflection angle was observed to produce dramatic increases in the peak magnitude of the pitching moment. This observation is exemplified in the $\delta_T = 90°$ case shown in Fig. 3.8, where C_m at $\alpha = 4°$ took a value of -0.2 for $\lambda = 0$ and -0.70 for $\lambda = 5.25$. The offset of the thrust force vector relative to the quarter-chord location is likely a significant contributor to these pitching moment effects. However, as will be shown later, the nacelle surface was configured to carry a significant surface pressure load of the airfoil system, which was further increased for higher nozzle deflection angles. This large sensitivity of the nacelle C_p distribution to the jet deflection angle is believed to be due to changes in the circulation of the powered wake, which become stronger as the jet deflection angle is increased. As a result, elements of the C_m shift due to δ_T also reflect those produced by flap deflection shown in Fig. 3.2c. In the windmill case, the effect of thrust deflection angle can be seen as a downwards bowing of the C_m vs α curve. The uneven shift of pitching moment is likely due to the onset of separated flow at higher angles of attack, notably across the region of the airfoil in front of the DEP system inlets, as the windmilling fans served as an obstruction to the flow. This bowing behavior is most clear in the C_m vs α polars at $\delta_T = 60°$ and $\delta_T = 90°$. However, increased tip speed ratio can be seen to reduce this effect. This was likely due to the ability of the DEP system to increase the flow speed on the upper surface of the airfoil and delay separation.

In all of the powered cases, increasing thrust deflection angle can be seen to cause an overall increase in C_l. This is most clear in the highest λ cases, where the lift coefficient polar exhibits an upwards shift from the $\delta_T = 5.19°$ case to the 90° case. However, it can be seen that for lower λ cases, increasing thrust deflection angle only increases the lift polar and maximum lift coefficient to a certain point, after which further increases in δ_T yield the same or lower maximum lift coefficient. As λ further decreases, the δ_T at which maximum lift occurs can be seen to also

decrease. For example, in the $\lambda = 4.5$ case at $Re_c = 0.75 \times 10^6$, the maximum C_l values were 1.78, 2.15, 2.36, 2.42, and 2.40 for increasing δ_T. In the $\lambda = 2.5$ case, the maximum C_l values were 1.61, 1.61, 2.23, 1.75, and 1.67 for increasing δ_T. This behavior could be attributed to increasingly aggressive adverse pressure gradients associated with higher nozzle deflection angles combined with the flow control capability of the DEP system to sustain attached flow in these conditions.

An important takeaway is the the ability of the system to sustain a range of both positive and negative C_d values for the same, high C_l values at thrust deflection angles greater than 45° and various tip speed ratios. This indicates the potential ability of a vectored DEP system to be tailored for various degrees of stream-wise flow acceleration while maintaining a fixed dimensionless lift characteristic. For example, at $\alpha = 12°$, the system could sustain a C_d of 0.1 in the $\lambda = 2.5$, $\delta_T = 60°$ case or a C_d of -0.1 in the $\lambda = 4.5$, $\delta_T = 5.19°$ case. In both cases, the C_l is approximately 1.4. However, it is important to note that the pitching moment of the first case is more than twice that of the second case as a result of the large difference in nozzle deflection. This coupling of the pitching moment to thrust deflection could pose a significant design challenge. Therefore, large amounts of thrust deflection could be used to initially achieve high C_l values at relatively low speeds and angles of attack before transitioning to lower amounts of thrust deflection as more control over angle of attack is permissible due to the increasing airspeed. Overall, the flexibility of the system presents the potential opportunity for novel ways of operating through particularly challenging flight regimes. One such regime is the transition stage of vectored-thrust VTOL vehicles, where the aircraft proceeds into a forward flight phase from a hover phase. Across this regime, the high C_l and negative C_d values associated with $\delta_T = 45°$ and 60° would be more beneficial than the $\delta_T = 90°$ case for generating lift at low speeds while maintaining a forward acceleration.

3.2.5 Aerodynamic Performance for RPM Control

Data were taken for the DEP system across a range of constant RPM values at Reynolds numbers of $Re_c = 0.5 \times 10^6$ and $Re_c = 0.75 \times 10^6$, which are shown in Fig. 3.10 and 3.11. It should be noted that for some test cases, the voltage of the batteries used to power the EDFs decreased to levels that were insufficient to maintain the target ω at high angles of attack. These cases can be clearly identified by significant decreases in the magnitudes of C_l, C_d, and C_m at high angles

of attack. Some of the test cases with this issue were repeated, and the batteries were changed between test points of the subsequent tests. Co-plots of the ideal and actual tip speed ratios for both Reynolds number cases can be seen in Fig. 3.6a and Fig. 3.7a, which highlight the variations in tip speed ratios across α resulting from fixed RPM control and Re_c variation. As expected, increasing the fixed target RPM led to increased variation in actual tip speed ratio due to variation in Re_c. Despite these differences in λ, data from the RPM control cases exhibit trends identical to those where tip speed ratio was controlled. Similar negative shifts in the C_d polar and increases in the lift curve slope can be observed for increasing RPM, and increased thrust deflection angle can be seen to result in a decreased zero lift angle of attack.

Data collected at $Re_c = 0.5 \times 10^6$ can be seen to exhibit trends unique to that Reynolds number. In addition to the variation in C_l, C_d, and C_m over a range of α in the windmill case at $Re_c = 0.5 \times 10^6$ shown in Fig. 3.12, a significant variation in C_l, C_d, and C_m can be seen in the $\delta_T = 45°$ and $60°$ cases for multiple $\omega = 30,000$ RPM cases. In Fig. 3.10, it can be seen that one set of data taken at $\delta_T = 45°$, $\omega = 30,000$ RPM appears to follow trends associated with increased ω that have been identified, including a nonlinear decrease in C_d, relatively uniform decrease in C_m, and an overall increase in C_l and C_{l_α}. However, another set of data for the same case, also shown in Fig. 3.10, exhibits nearly identical performance to the previous case of $\omega = 25,000$. The only difference between data in the second $\omega = 30,000$ RPM case and data in the $\omega = 25,000$ case is a slightly lower C_d for $\alpha < 10°$. The tip speed ratios and test section Re_c for these sets of significantly different results at $\omega = 30,000$ RPM can be seen to be nearly identical in Fig. 3.6a and 3.6b. Variations in results can also be seen in the $\delta_T = 60°$, $\omega = 30,000$ RPM case, where data were collected in three separate runs over $-10° < \alpha < 20°$, $0° < \alpha < 20°$, and $10° < \alpha < 20°$. However, performance data for $\alpha > 10°$ closely matches between the two runs spanning a shorter range of α. In addition, the C_l, C_d, and C_m data that matches between the two runs can be seen to vary relative to data from the next lowest ω case in a manner that is consistent with the observed trends in performance with respect to ω. The known limitations of battery capacity and increased magnitudes of C_l, C_d, and C_m in runs over a shorter α range might suggest variation in tip speed ratio or Re_c as the cause of these differences. However, it can be seen in Fig. 3.6a and 3.6b that there is nearly no variation in λ or Re_c between these runs except for at test points where the batteries were depleted. Similar variations in performance for the same target ω can be seen at

$Re_c = 0.75 \times 10^6$ in Fig. 3.11, where differences are present between two runs of data collected at $\delta_T = 45°$ and $\omega = 30,000$ RPM. This is in contrast to data taken at $Re_c = 1.0 \times 10^6$ shown in Fig. 3.9, which exhibit consistent results for multiple runs at $\delta_t = 5.19°$, $\lambda = 4.0$ and $\delta_T = 45°$, $\lambda = 3.5$. This is also in contrast to data taken at $Re_c = 0.75 \times 10^6$ with tip speed ratio control, where consistent results can be seen for the $\delta_T = 45°$, $\lambda = 2.5$, 3.5, and 4.5 cases across multiple runs. The reduction in variation between identical runs with increased Re_c and tip speed ratio control suggests a potential correlation with tip speed ratio and viscous effects.

3.3 Vectored DEP Steady Surface Pressure Measurements

Airfoil and nacelle surface pressure measurements were taken for the same test cases and Reynolds numbers presented in Section 3.2, and data from selected cases are shown in Figures 3.14 - 3.24. Pressure measurements were taken to investigate the circulation effects of the DEP system and to compare features of the surface pressure distributions to the baseline S8036 airfoil model. In addition, the use of three spanwise rows of surface pressure taps permitted the investigation of spanwise pressure variation produced across a propulsor within the DEP system.

Examples of C_p distributions produced by the aero-propulsive system across the three tap rows are shown in Figs. 3.14, 3.15, and 3.16, which correspond to conditions of $\delta_T = 5.19°$ and $\delta_T = 45°$ at $\alpha = 4°$ and a range of λ values at $Re_c = 0.5 \times 10^6$, 0.75×10^6, and 1.0×10^6. It can be seen that for low and moderate tip speed ratios at $Re_c = 0.75 \times 10^6$ and 1.0×10^6, the surface pressure immediately upstream of the DEP system inlet was able to recover to a pressure of $C_p = 0$, or higher. This recovery is an important component of an effectively-designed boundary-layer ingesting DEP system, as ingesting accelerated inviscid flow beyond the freestream velocity results in counterproductive losses in propulsive efficiency. Instead, by having the inlet flow recover to the freestream velocity, the incoming kinetic energy of the inviscid flow region remains consistent with or even below that produced by an uncoupled propulsor in uniform freestream flow, in addition to the reductions in the ingested flow momentum across the boundary-layer region. It can also be seen that for the same tip speed ratio, an increase in thrust deflection from $\delta_t = 5.19°$ to 45° yields increases in the magnitudes of the airfoil and nacelle suction peak as well as a decrease in pressure on the airfoil upper surface and increase in pressure on the airfoil lower surface. Similar trends can

be seen in Fig. 3.20, 3.22, and 3.24, which present pressure distributions co-plotted for various amounts of thrust deflection. For cases of constant thrust deflection, increased EDF tip speed ratio can be seen to produce similar effects on the airfoil pressure distributions but the opposite effect on the nacelle upper surface pressure distribution. These trends are most clear in Fig. 3.19, 3.21, and 3.23.

A comparison of C_p distributions in the windmill case across Reynolds numbers is shown in Fig. 3.17, which indicates minimal variation in pressure coefficient between $Re_c = 0.75 \times 10^6$ and 1.0×10^6. This is in contrast to the pressure distributions for the $Re_c = 0.5 \times 10^6$ case shown in the same figure, which shows distinct variations from those at the higher Reynolds numbers. It should be noted that data were presented in Fig. 3.17 at angles of attack which correspond to those before, during, and after the observed variation in aerodynamic performance in the windmill case at $Re_c = 0.5 \times 10^6$ discussed in Section 3.2.3 and shown in Fig. 3.12. A substantial increase in pressure on the upper surface of the nacelle can be seen at $\alpha = 6°$ relative to the higher Re_c cases, which is consistent with the decreases in C_l and C_m magnitudes present in Fig. 3.12 at that angle of attack in the $Re_c = 0.50 \times 10^6$ case. At the subsequently higher angle of attack $\alpha = 12°$, the nacelle upper surface can be seen to support a suction peak similar to those seen at lower α values. In addition, a plateau in the upper surface pressure distribution can be seen from $x/c = 0.15$ to 0.2. Similar regions of constant pressure, which could be taken to indicate the presence of locally-separated regions in some cases, can be seen in the pressure recovery portion of the pressure distributions at $Re_c = 0.5 \times 10^6$ shown in Fig. 3.19. These features are absent from pressure distributions taken at higher Reynolds numbers, such as those shown in Fig. 3.18, which compares pressure distributions taken at the same tip speed ratio at $Re_c = 0.75 \times 10^6$ and 1.0×10^6.

3.3.1 Spanwise Variation

Examination of the pressure data across the entire ranges of λ and δ_T revealed relatively small spanwise variations in pressure distributions across the region covered by the three pressure tap rows for all angles of attack for $Re_c = 0.75 \times 10^6$ and 1.0×10^6, as can be seen in Fig. 3.15 and 3.16. This large degree in uniformity is contrasted by spanwise variations in pressure loading produced by a number of propeller-driven DEP systems, which feature large variations in the spanloading

across the spanwise region due to the swirling flow contribution produced across the propeller diameter. The most significant spanwise variation in the pressures was observed on the upper surface of the airfoil near the fan inlet for high fan tip speed ratios. In Fig. 3.15, with $\lambda = 5.25$ the upper surface pressure along the fan edge ($y/R = 1.13$) features a pressure recovery profile with a monotonic increase in C_p all the way up to the inlet ($x/c = 0.76$). At the spanwise position of $y/R = 0.57$, a normal pressure recovery profile is observed, though immediately upstream of the fan inlet a sudden decrease in the surface C_p can be observed, at $x/c = 0.76$. Along the fan centerline, at $y/R = 0$, a consistent, yet greater, pressure decrease is observed at this same position. The pressure distributions for the $\lambda = 4$ case in Fig. 3.16a demonstrate a similar trend. This spanwise variation is believed to be produced due to a radial variation in the induced flow across the fan blade elements, alongside the three-dimensional contraction of the flow across the rectangular-to-cylindrical inlet.

The pressures measured on the airfoil lower surface along the $y/R = 1.13$ row appear slightly lower than the surrounding rows for certain cases at $Re_c = 0.75 \times 10^6$ shown in Fig. 3.15. A similar variation can be seen in data taken at $Re_c = 0.5 \times 10^6$ shown in Fig. 3.14, where pressures from the same row appear to be significantly lower than the others under certain conditions. This is in contrast to the data for a Reynolds number of 1.0×10^6 presented in Fig. 3.16, where minimal variation can be seen between all three rows. Given the correlation of this variation with lower Reynolds numbers, it was assumed to be related to viscous flow effects. This fact, combined with the relatively minimal spanwise variation for other conditions, led to the decision to present subsequent surface pressure data for the single row of pressure taps at located at $y/R = 0$.

3.3.2 Constant Tip-Speed Ratio Surface Pressure Measurements

Overall trends in the airfoil and nacelle pressure distributions can be seen in Figs. 3.19 - 3.24, which can be used to visualize differences in the airfoil C_p distributions brought about from varying λ and δ_T independently at various Reynolds numbers and angles of attack. Figs. 3.19 and 3.20 contain pressure data taken at $Re_c = 0.5 \times 10^6$, and Figs. 3.21 and 3.22 contain pressure data taken at $Re_c = 0.75 \times 10^6$. Figs. 3.23 and 3.24 contain pressure data taken at $Re_c = 0.75 \times 10^6$ at various angles of attack.

In Figs. 3.19a and 3.21a, it can be seen that increasing fan tip speed ratio leads to a uniform decrease in the pressure on the upper surface and increase in the pressure on the lower surface, indicating an increase in airfoil circulation effects. At higher cases of thrust deflection, such as $\delta_T = 90°$ shown in Figs. 3.19e and 3.21e, it can be seen that the uniform effects of increasing tip speed ratio magnify the circulatory effects associated with thrust deflection. Additionally, a decrease in the suction peak near the nacelle upper lip leading edge can be observed, which is produced by the movement of the stagnation point forward and around the leading edge with the constriction of the stream tube at higher thrust conditions.

From the pressure data in Figs. 3.20 and 3.22, it is immediately clear that vectoring leads to a significant increase in the suction peak of the airfoil as well as an increase in the pressure on the lower surface. These changes to the pressure distribution brought about by the nozzle deflection have a significant impact not only on the inviscid flow characteristics, but also the coupled viscous boundary layer. As seen in Fig. 3.22c, a region of constant surface pressure appears in the C_p distribution for $\delta_T = 90°$, indicating the presence of flow separation beginning at $x/c = 0.6$. A similar trend can be seen in Fig. 3.24b, where the start of a constant pressure region can be seen to appear at $x/c = 0.6$ in the $\delta_T = 60°$ case. With further increases in nozzle deflection angle to $\delta_T = 90°$, this separation position is observed to move upstream to $x/c = 0.55$. In addition, deflection of the thrust led to a significant increase in the nacelle suction peak as well as an overall decrease in the pressures along the nacelle upper surface.

As was seen from the force balance data, the effects of thrust vectoring were more pronounced at higher fan tip speed ratios. As a result, the pressure distributions shown in Fig. 3.24 were taken from the $\lambda = 4.5$ case. Pressure distributions shown in Fig. 3.23 were taken from a relatively low thrust deflection angle case of $\delta_T = 30°$ to better highlight the uniform effects of tip speed ratio. It is evident from the magnitude of the nacelle suction peaks at $\alpha = -4°$ in Fig. 3.23a and Fig. 3.24a that the pressure load carried by the nacelle plays a significant role in the decrease in zero lift angle of attack presented in Section 3.2.4.

3.4 Comparison Between Vectored DEP and Simple Flap

3.4.1 Performance Comparison

Lift, drag, and pitching moment polars for the baseline airfoil model are shown alongside vectored DEP data in Fig. 3.25 for various flap deflections, δ_f, and thrust deflection angles, δ_T. Separate polars are given for DEP data across tip speed ratios of $\lambda = 0$, 3.5, and 5.25. It can be seen from the vectored DEP C_l data that thrust vectoring produces an overall increase in stream-normal force coefficient for the presented tip speed ratios, excluding the windmilling case, and offers a higher maximum C_l value available in the powered cases. While the simple flap system achieved a maximum C_l of 1.679 at $\delta_f = 20°$, the vectored DEP system achieved a maximum C_l of 2.73 at $\delta_T = 60°$, $\lambda = 5.25$. Use of the simple flap can be seen to result in conventional, uniform increases in $C_{l_{\max}}$ and decreases in zero-lift angle of attack, with decreasing effectiveness as high flap deflection angles are produced. From $\delta_f = 0°$ to 5°, the zero lift angle of attack decreases by 2.5°, but from $\delta_f = 15°$ to 20°, the decrease is only 1°. However, a similar lift-curve slope is produced across the entire range of flap deflections studied here. On the other hand, the increase in C_l brought about by an increase in nozzle deflection angle was a strong function of angle of attack. Since vectoring produced changes in both zero-lift angle of attack and lift-curve slope, this behavior is anticipated, yet important to emphasize. The nonuniform increase in C_l can also be seen to vary significantly as a function of tip speed ratio. For example, a 1° decrease in zero lift angle of attack was observed between $\delta_T = 45°$ and 60° for $\lambda = 0$, whereas the decrease was 6° for $\lambda = 5.25$. A noticeable difference between the baseline and vectored DEP airfoils is the pitching moment characteristic, which demonstrates a typical uniform shift with deflection of the simple flap but significantly greater variations in magnitude for the vectored DEP system.

As expected, increasing flap deflection can be seen to produce an overall increase in drag. The effects of thrust deflection on the net stream-wise force coefficient, however, are more complex in the vectored DEP case. In the windmilling case, the drag is notably higher than the baseline airfoil due to significant installation effects and the obstructive nature of the DEP system in this case. In the powered cases at deflection angles less than 90°, it can be seen that the contribution of thrust from the DEP system along the stream-wise direction causes a shift of the overall C_l/C_d polars

in the negative C_d direction. This effect is much less prominent in the $\delta_T = 90°$ cases, where the vectoring of the thrust force into the chord-normal direction results in a net positive C_d value for all tip speed ratios utilized in the current study.

3.4.2 Surface Pressure Comparison

Pressure distributions for the simple flap configuration at $Re_c = 1.0 \times 10^6$ were also collected, with select cases shown at angles of attack of $\alpha = 4°$ and $\alpha = 10°$ with flap deflection angles of $\delta_f = 0°$, 10°, and 20°. These pressure distributions are shown in Fig. 3.26. Also shown in Fig. 3.26 are pressure distributions recorded for the vectored DEP system at $Re_c = 0.75 \times 10^6$ with thrust deflection angles of $\delta_T = 5.19°$, 45°, and 90°. The tip speed ratio for all of the vectored DEP data was $\lambda = 5.25$. A significant amount of suction on the upper surface of the nacelle can be observed at $\alpha = 4°$, where for all thrust deflection angles the minimum pressure of the nacelle surpasses that of the airfoil. However, a notable feature is the ability of the simple flap case, with $\delta_f = 20°$, to produce a leading-edge suction consistent with a vectored thrust case having a much larger deflection angle, $\delta_T = 90°$. Even in the $\alpha = 10°$ case, the nacelle can be seen to support a significant lift load. The significant increases in the vectored DEP airfoil suction peak in the $\alpha = 10°$ case at $\delta_T = 45°$ and 90° as compared to the shifts in the pressure distribution for the baseline airfoil at $\delta_f = 10°$ and 20° indicates the significant circulation effects of the vectoring system in a fashion conceptually similar to that produced by a movement of the airfoil camber line through a simple flap deflection. However, the region of constant pressure beginning at $x/c = 0.5$ in the $\alpha = 10°$, $\delta_T = 90°$ case indicates the onset of separated flow at high angles of thrust deflection. One additional key difference between the conventional and DEP configuration can also be observed by investigating the trailing-edge pressures produced by both configurations. It is interesting to note that the trailing-edge C_p of the conventional simple flap has a shared pressure asymptotically reached by both the upper and lower surfaces, as expected. However, for the DEP configuration, the pressure difference between the furthest aft surface pressure tap on the nacelle upper surface and the trailing edge of the airfoil lower surface demonstrates the ability of the system to support a pressure load beyond the trailing edge due to the powered wake.

3.5 Chapter 3 Table and Figures

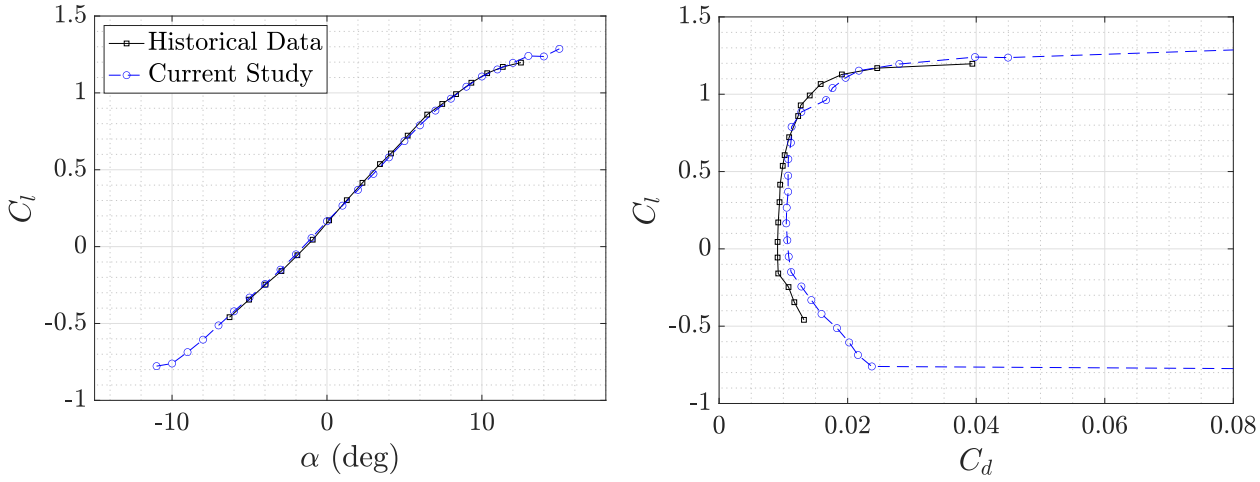

(a) C_l vs α

(b) C_l vs C_d

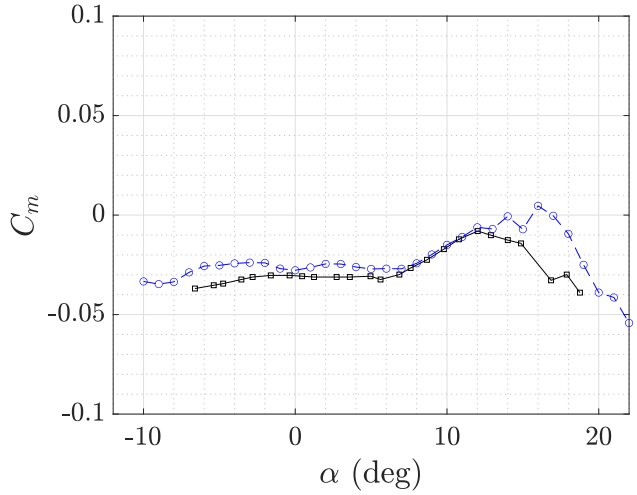

(c) C_m vs α

Figure 3.1: Performance of the baseline S8036 airfoil model compared to historical data [22] at $Re_c = 0.5 \times 10^6$

	Static	Re_c **= 0.5 × 10^6**	Re_c **= 0.75×10^6**	Re_c **= 0.75×10^6**	Re_c **= 1.0 × 10^6**
α **(deg)**	0°	−10°:2°:20°, 0°:2°:20°, 10°:2°:20°	−10°:2°:20°	−10°:2°:20°	−10°:2°:20°
λ (V_{tip}/U_∞)	–	–	–	0, 2.5, 3.5, 4.5, 5.25	0, 2, 3, 3.5, 4
ω (**1000 RPM**)	Windmill, 15, 20, 25, 30	Windmill, 15, 20, 25, 30	Windmill, 15, 20, 25, 30	–	–
δ_T **(deg)**	5.19°, 30°, 45°, 60°, 90°	5.19°, 30°, 45°, 60°, 90°	5.19°, 30°, 45°, 60°	5.19°, 30°, 45°, 60°, 90° (partial)	5.19°, 30°, 45°, 60° (partial), 90° (partial)

Table 3.1: Test parameters and values for various Reynolds number cases

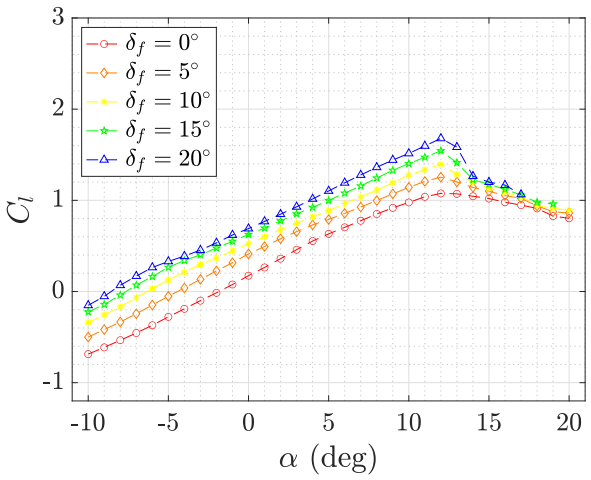

(a) C_l vs α for a range of δ_f

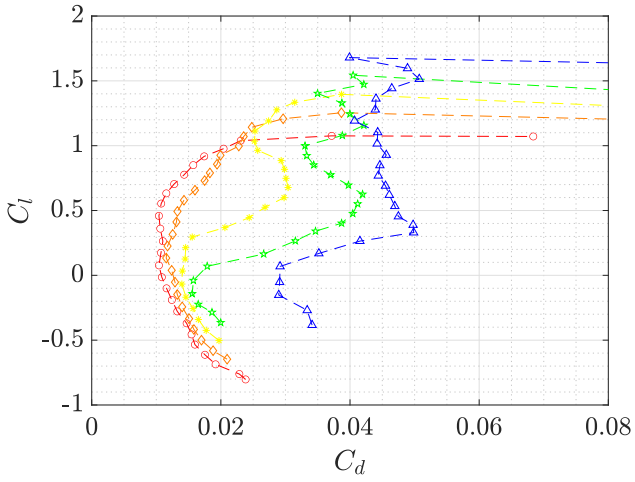

(b) C_l vs C_d for a range of δ_f

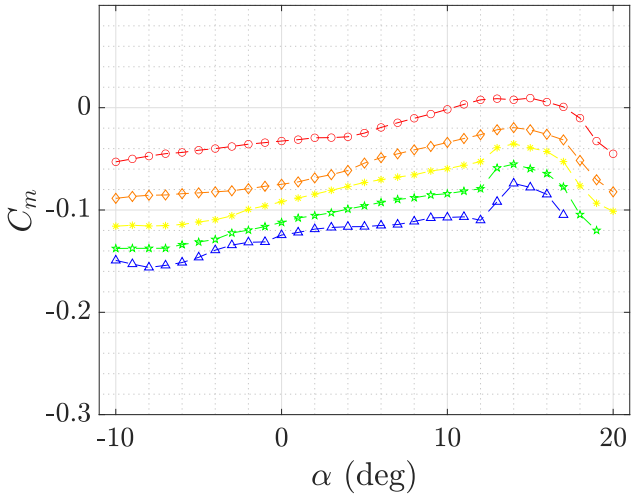

(c) C_m vs α for a range of δ_f

Figure 3.2: Performance of the baseline S8036 airfoil model with a 25%-chord simple flap for a range of δ_f

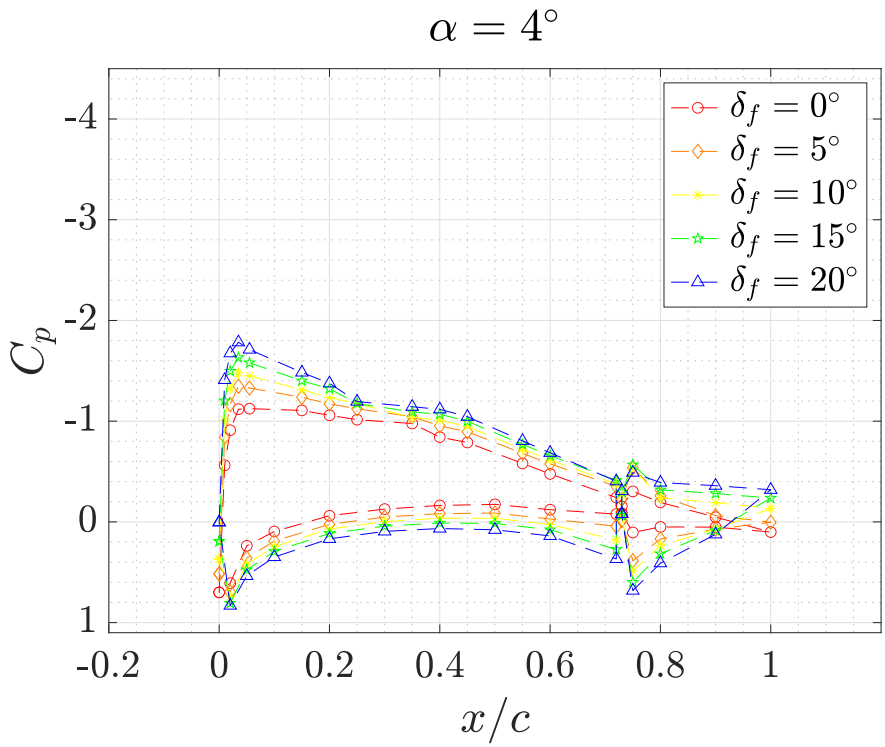

(a) C_p vs x/c at $\alpha = 4°$

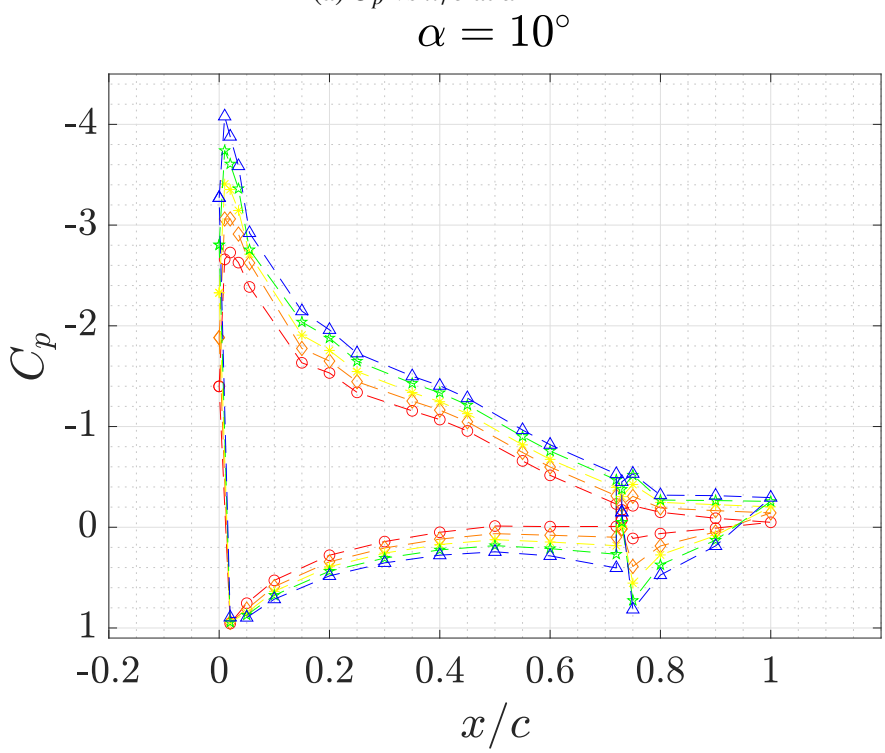

(b) C_p vs x/c at $\alpha = 10°$

Figure 3.3: Pressure distributions of the baseline airfoil with a 25%-chord simple flap at $Re_c = 0.5 \times 10^6$ for various flap and thrust deflection angles at a) $\alpha = 4°$ and b) $\alpha = 10°$

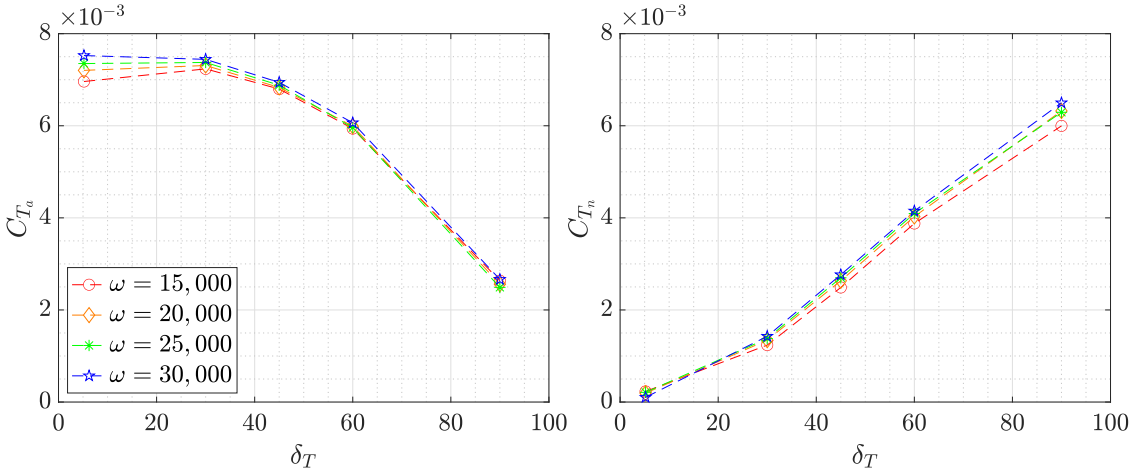

(a) C_{T_a} vs δ_T for various fan ω values

(b) C_{T_n} vs δ_T for various fan ω values

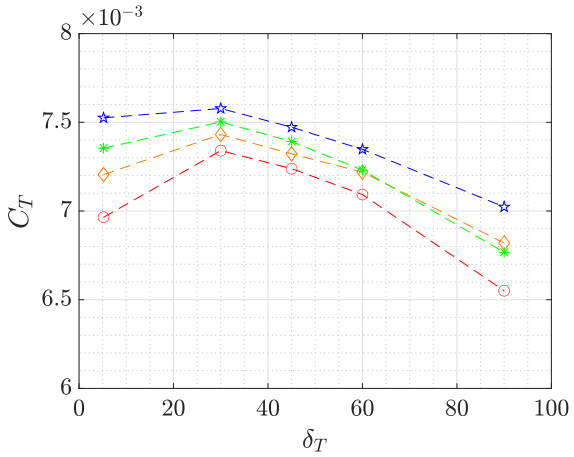

(c) C_T vs δ_T for various fan ω values

Figure 3.4: C_{T_a}, C_{T_n}, and C_T vs δ_T for a range of ω values

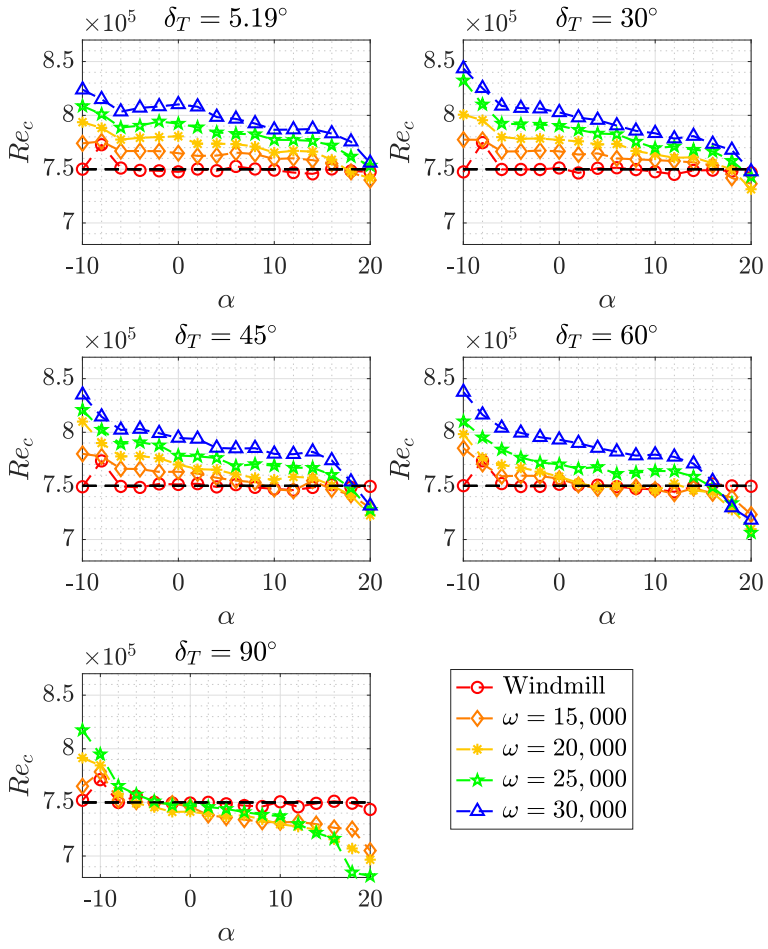

(a) Re_c vs α for the ω control case

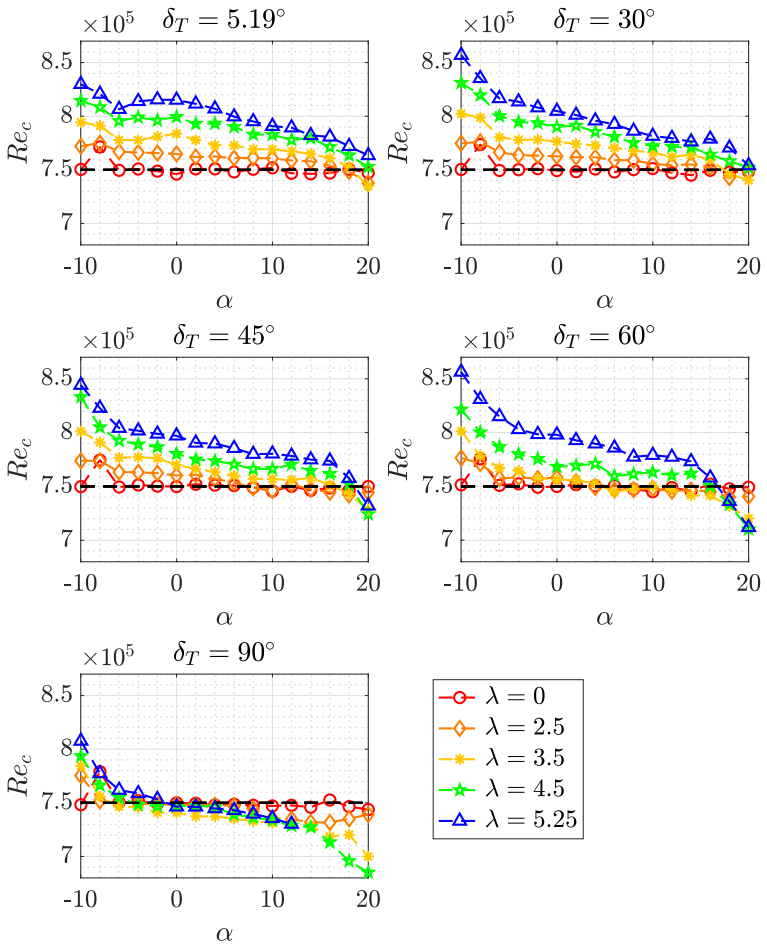

(b) Re_c vs α for the λ control case

Figure 3.5: Measured test section Re_c vs. α for a sweep of target EDF a)RPM values (ω) and b)tip speed ratio values (λ) at each nozzle deflection angle, δ_T, for the target Re_c of $750,000$

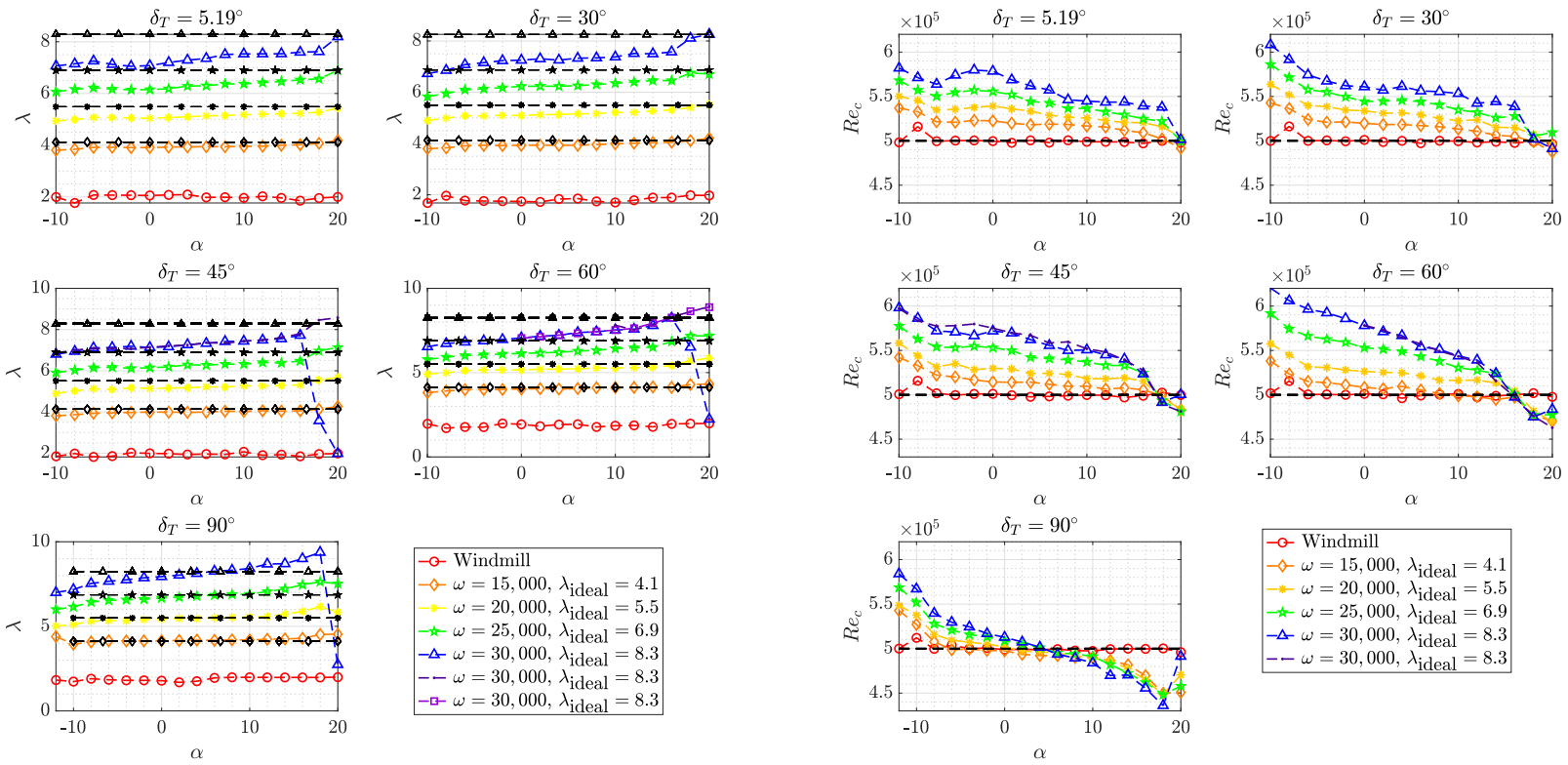

(a) Average EDF λ vs α and ideal λ for the ω control case

(b) Re_c vs α for a sweep of target EDF RPM values

Figure 3.6: Average EDF tip speed ratio (λ) vs. α for a sweep of target EDF RPM values (ω) and measured test section Re_c vs α for the target ω values across all δ_T at a target $Re_c = 0.5 \times 10^6$

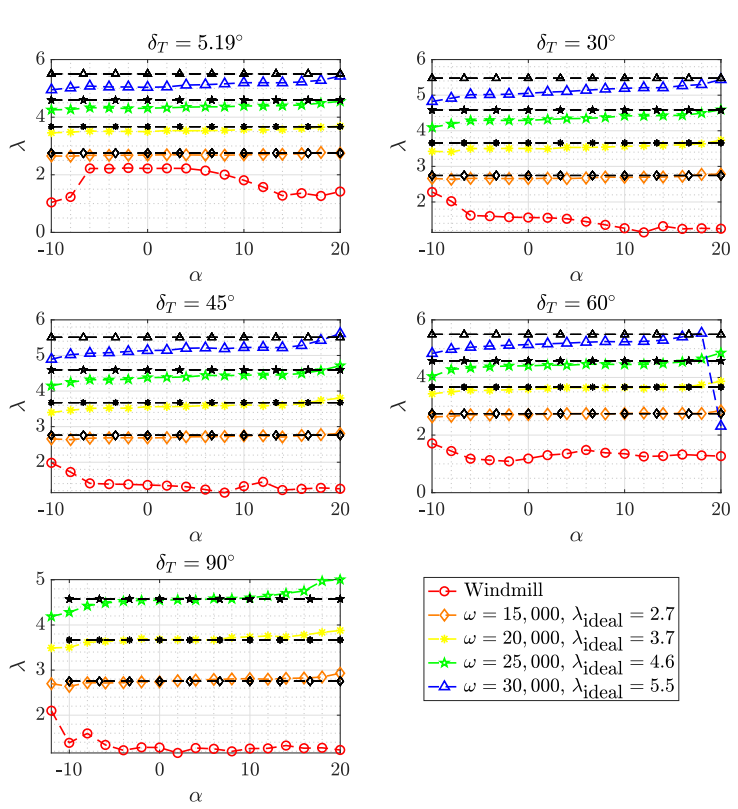

(a) Average EDF λ vs α and average λ for the ω control case

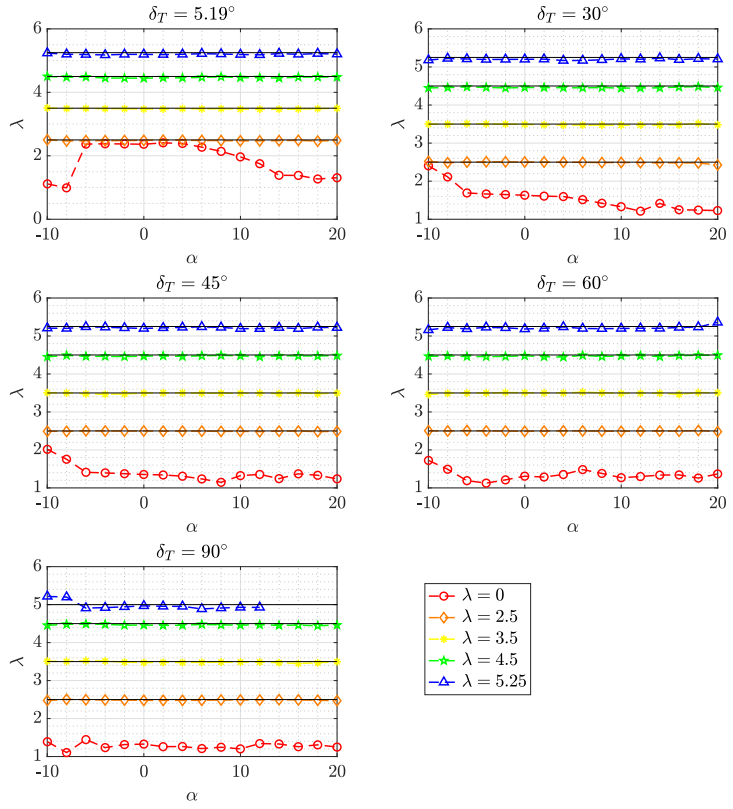

(b) Average EDF λ vs α and target λ for the λ control case

Figure 3.7: Average EDF tip speed ratio (λ) vs. α for a sweep of target EDF a)RPM values (ω) and b)tip speed ratio values (λ) at each nozzle deflection angle, δ_T, for the target Re_c of 0.75×10^6

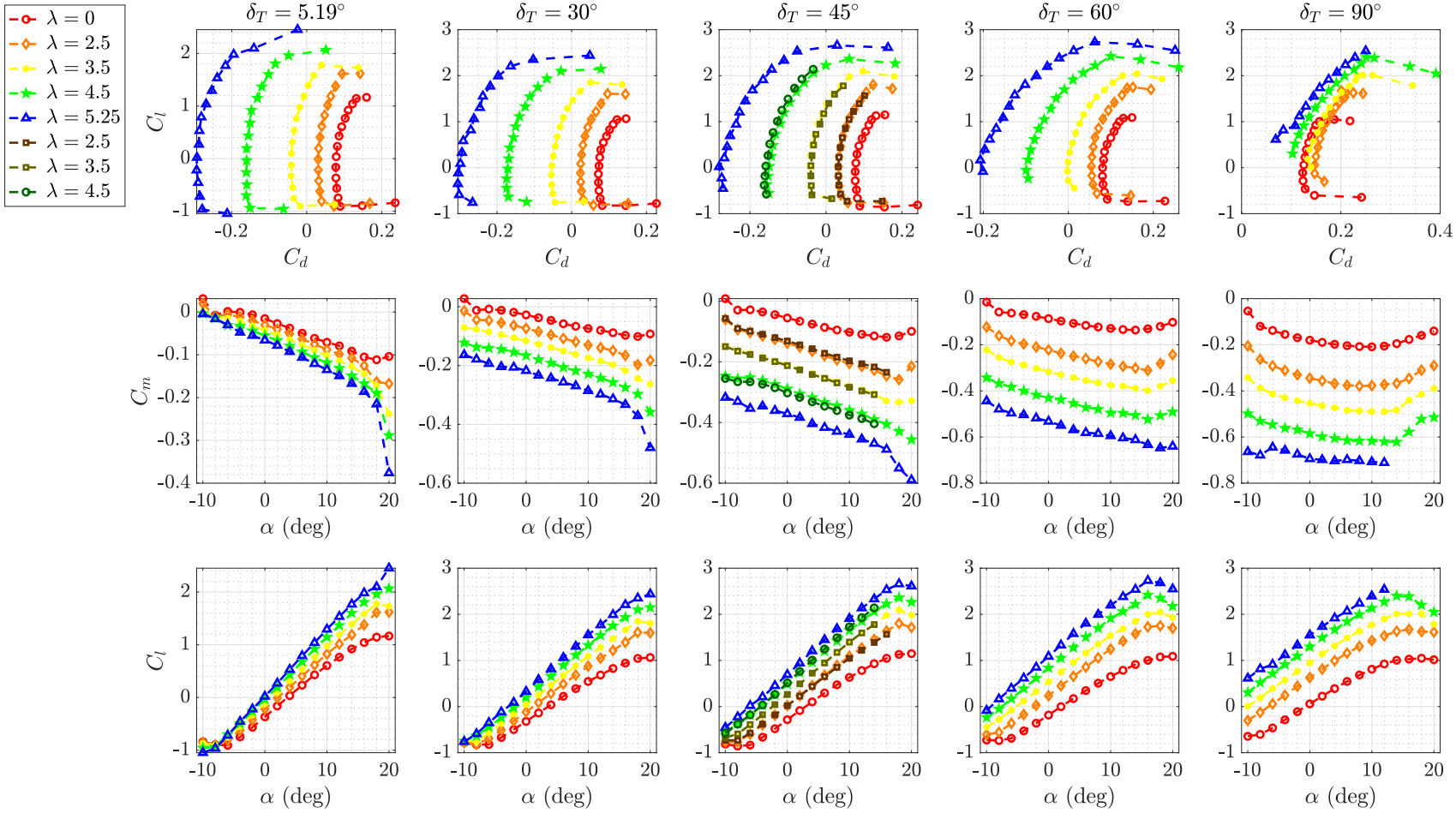

Figure 3.8: Force and moment coefficient data for the $Re = 0.75 \times 10^6$ case for a range of target λ values

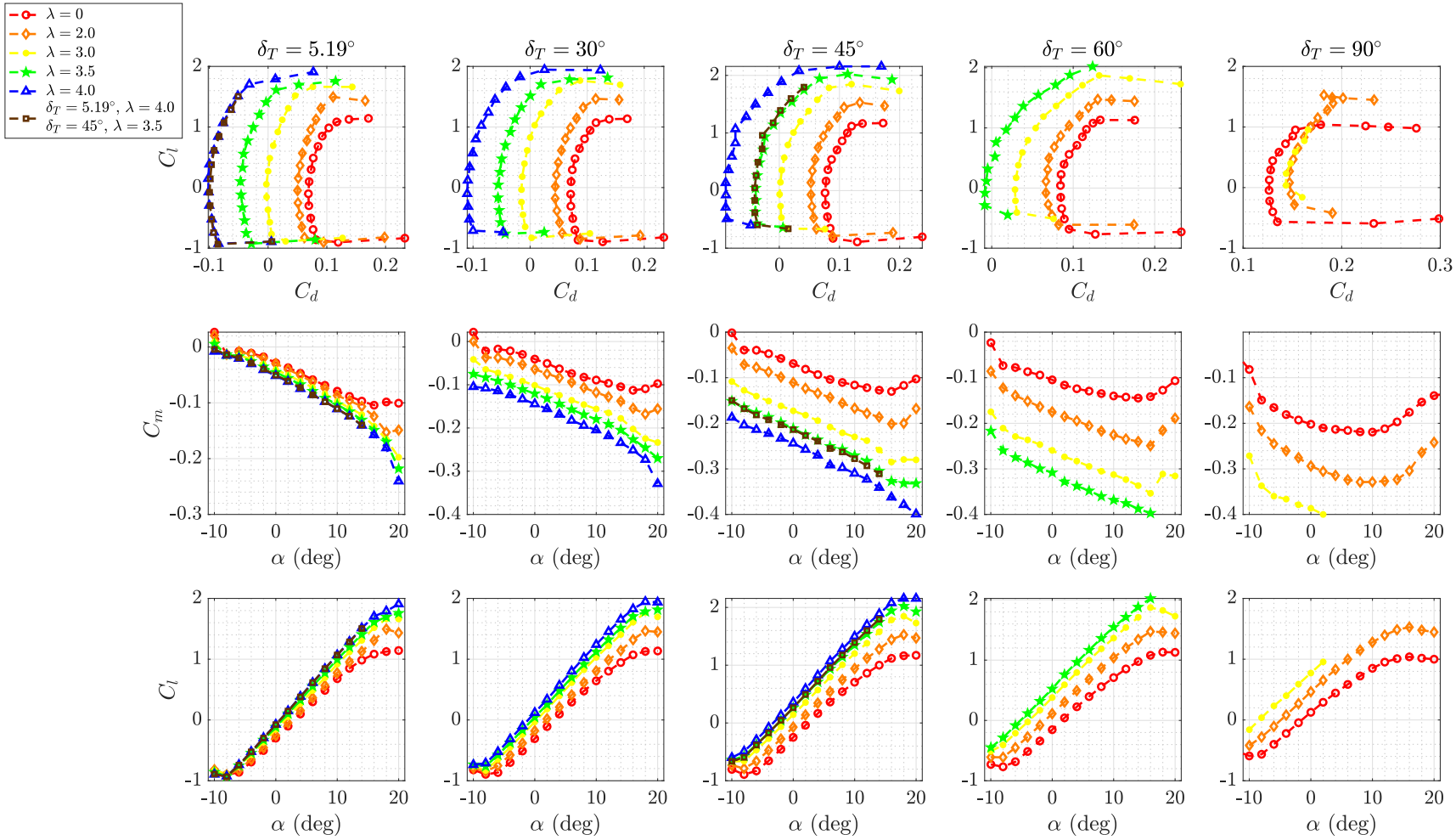

Figure 3.9: Force and moment coefficient data for the $Re = 1.0 \times 10^6$ case for a range of target λ values

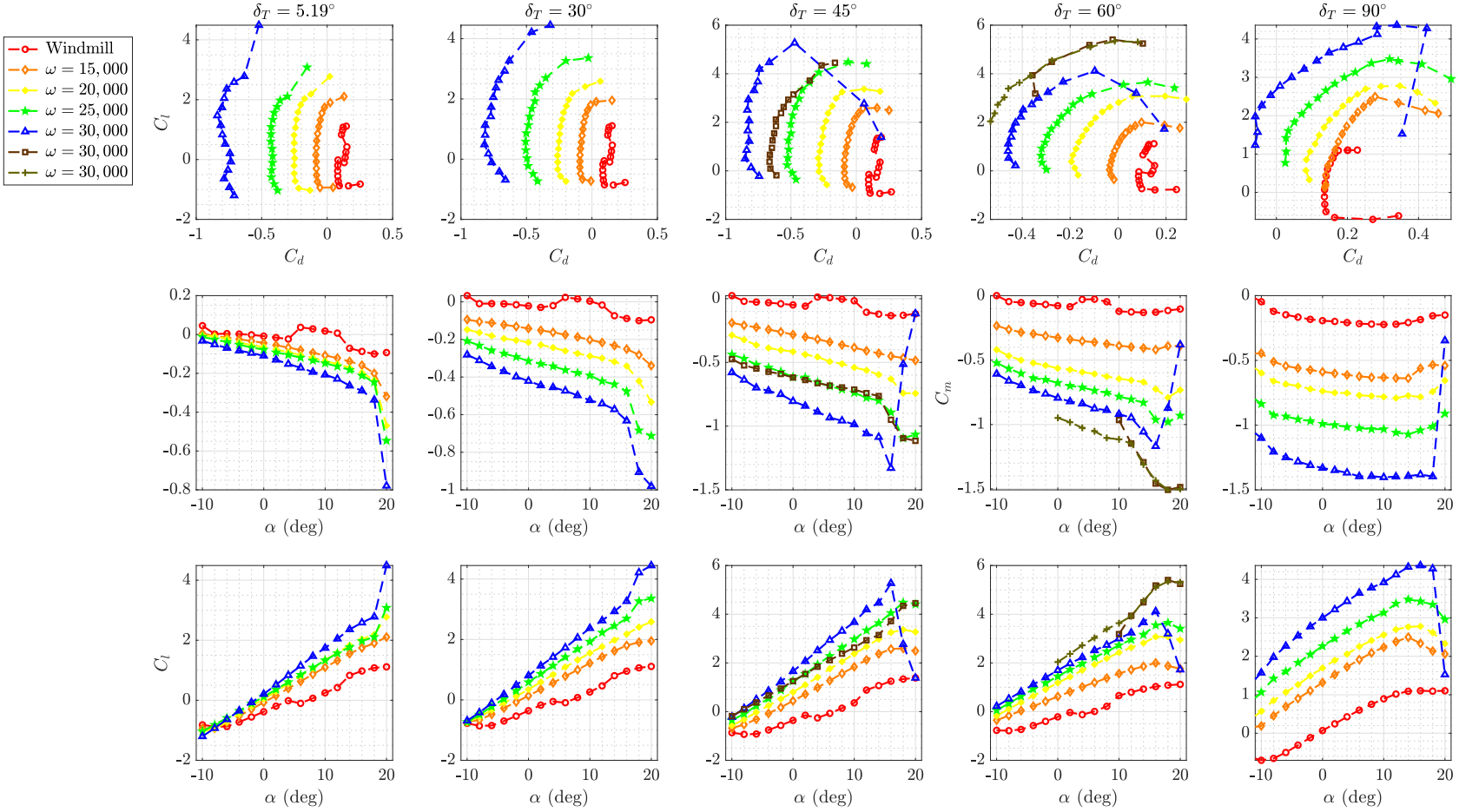

Figure 3.10: Force and moment coefficient data for the $Re = 0.5 \times 10^6$ case for a range of target ω values

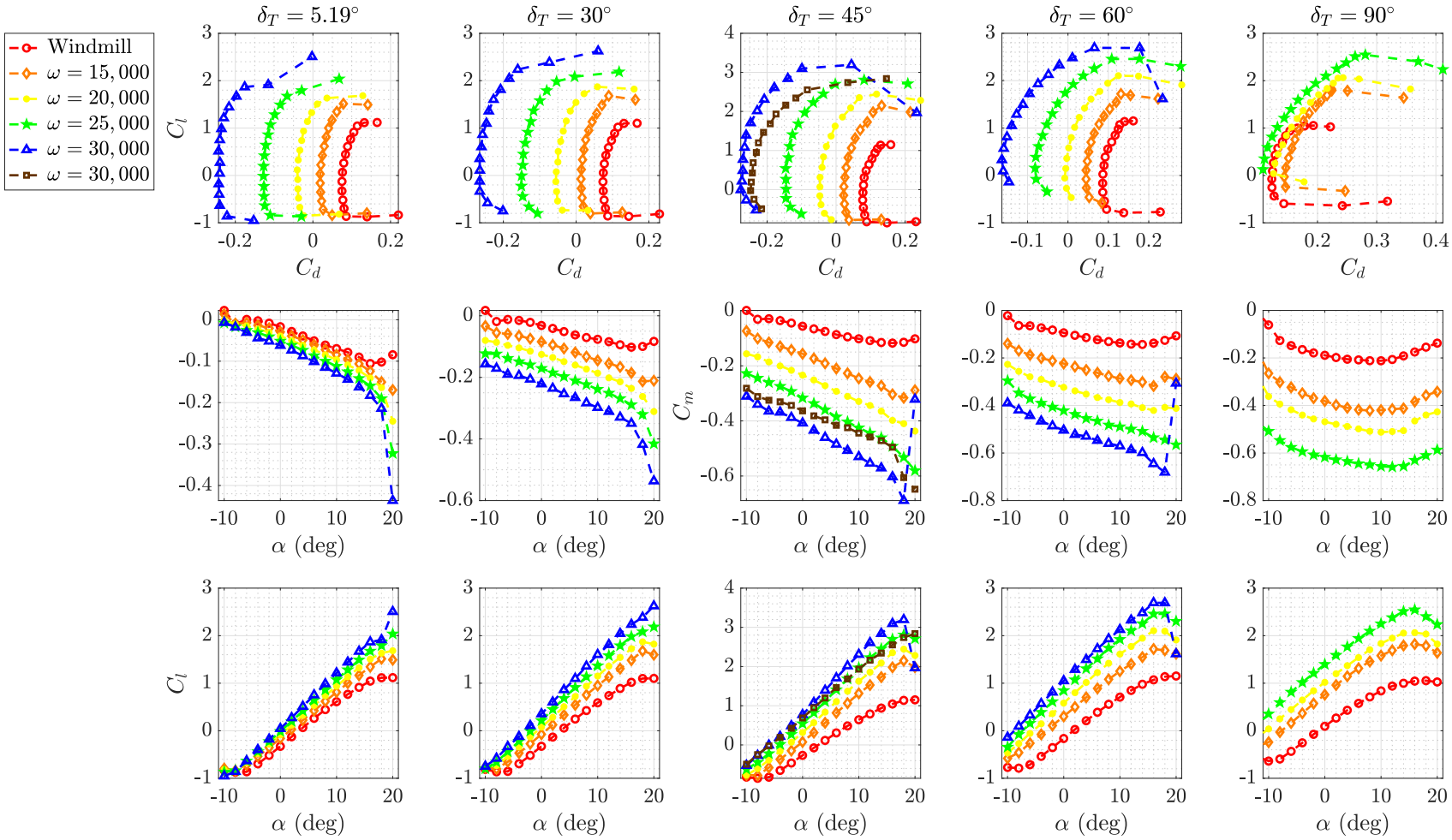

Figure 3.11: Force and moment coefficient data for the $Re = 0.75 \times 10^6$ case for a range of target ω values

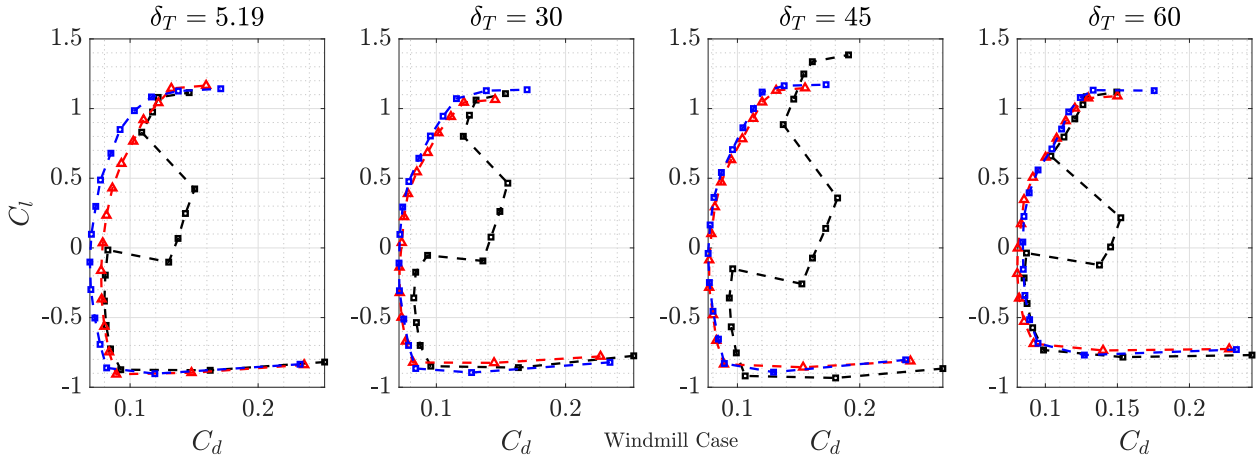

(a) C_l vs C_d for a range of δ_T and windmilling conditions

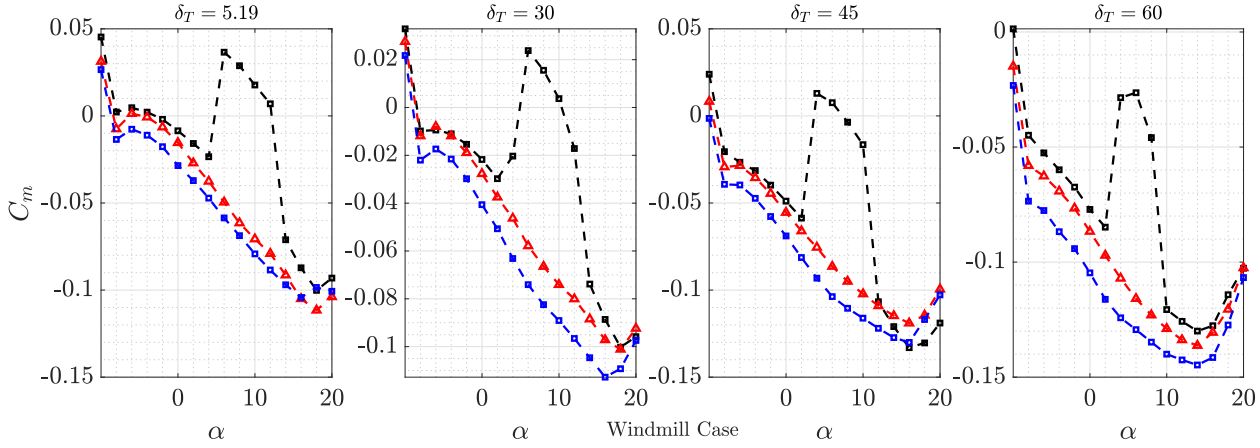

(b) C_m vs α for a range of δ_T and windmilling conditions

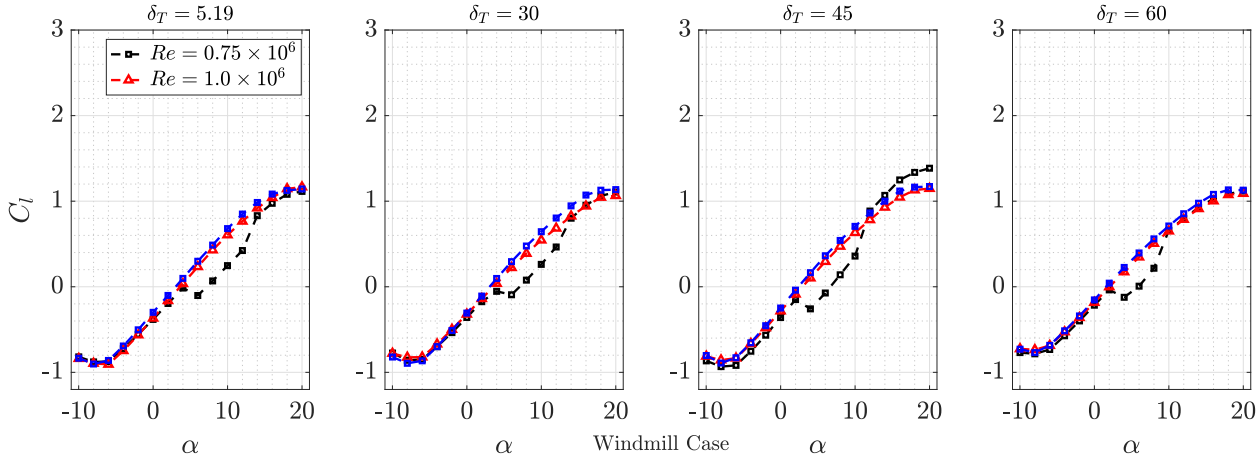

(c) C_l vs α for a range of δ_T and windmilling conditions

Figure 3.12: Force and moment coefficient data for the $Re_c = 0.5 \times 10^6$, 0.75×10^6, and 1.0×10^6 cases

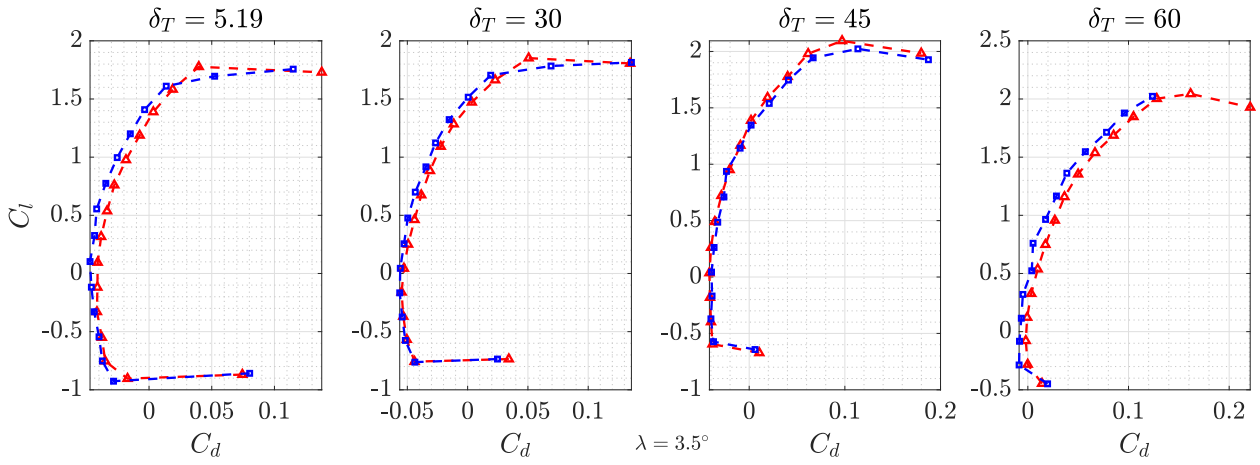

(a) C_l vs C_d for a range of δ_T and $\lambda = 3.5$

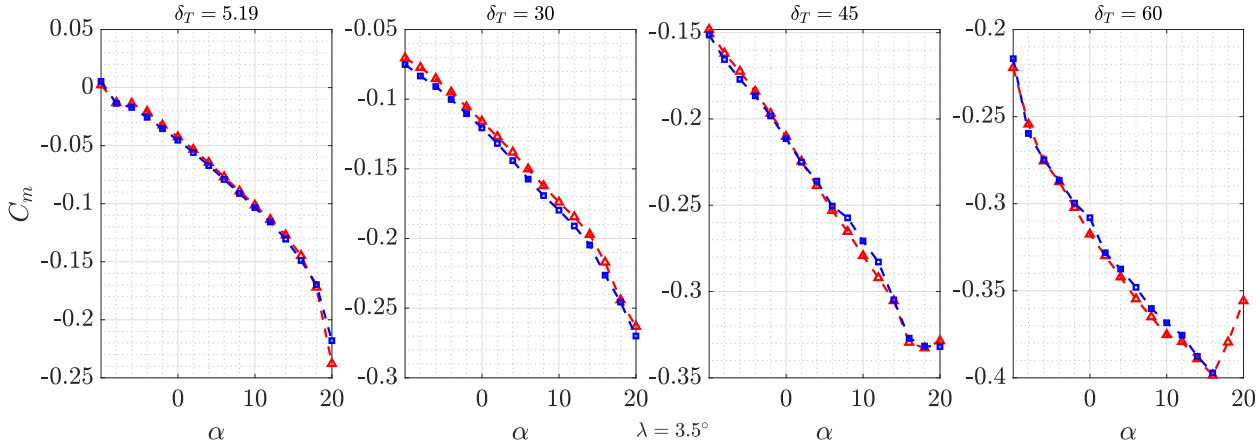

(b) C_m vs α for a range of δ_T and $\lambda = 3.5$

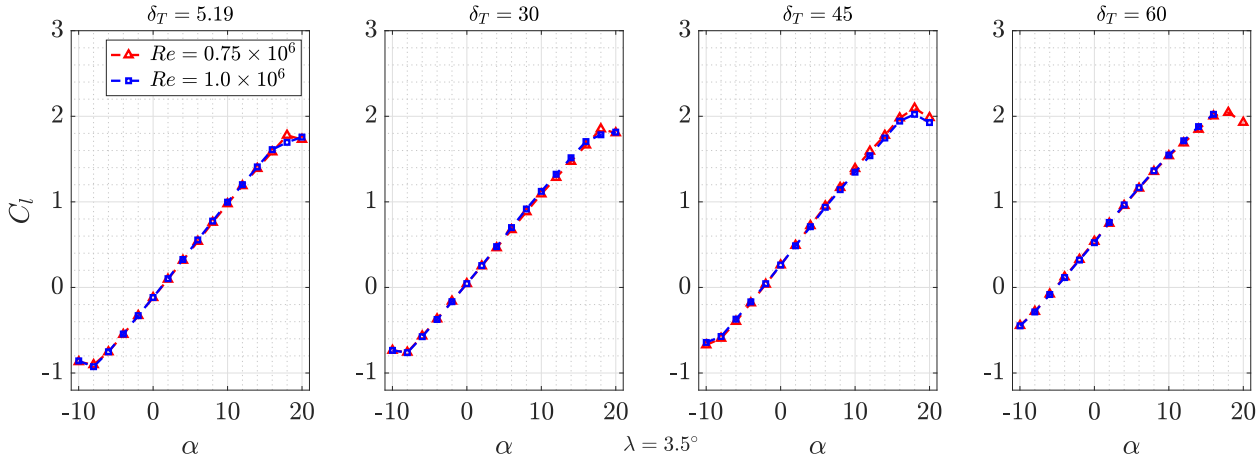

(c) C_l vs α for a range of δ_T and $\lambda = 3.5$

Figure 3.13: Force and moment coefficient data for the $Re_c = 0.75 \times 10^6$ and 1.0×10^6 cases

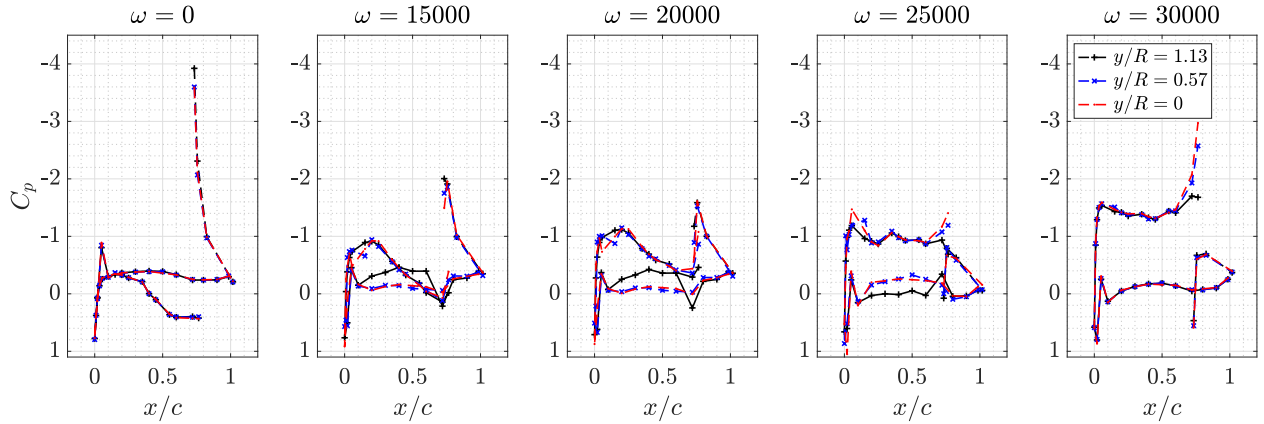

(a) C_p vs x/c for various ω at $\delta_T = 5.19°$

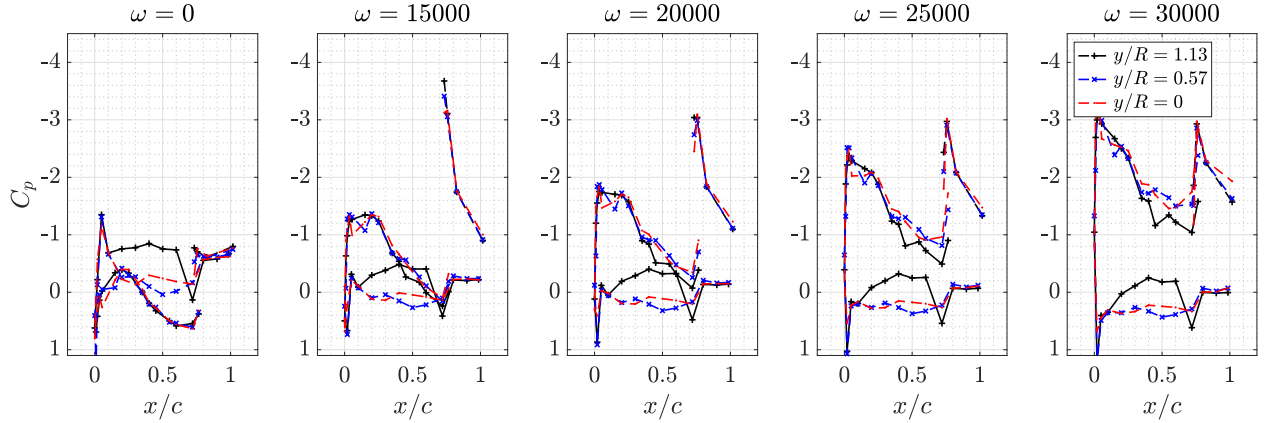

(b) C_p vs x/c for various ω at $\delta_T = 45°$

Figure 3.14: C_p vs x/c distributions for each row of pressure taps at $\alpha = 4°$ for various δ_T and ω values at $Re_c = 0.5 \times 10^6$

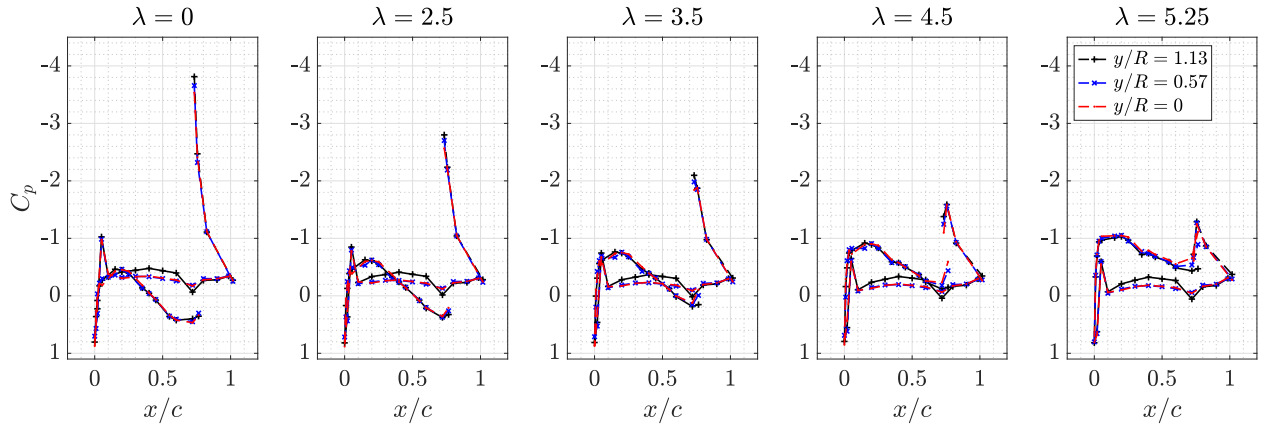

(a) C_p vs x/c for various λ at $\delta_T = 5.19°$

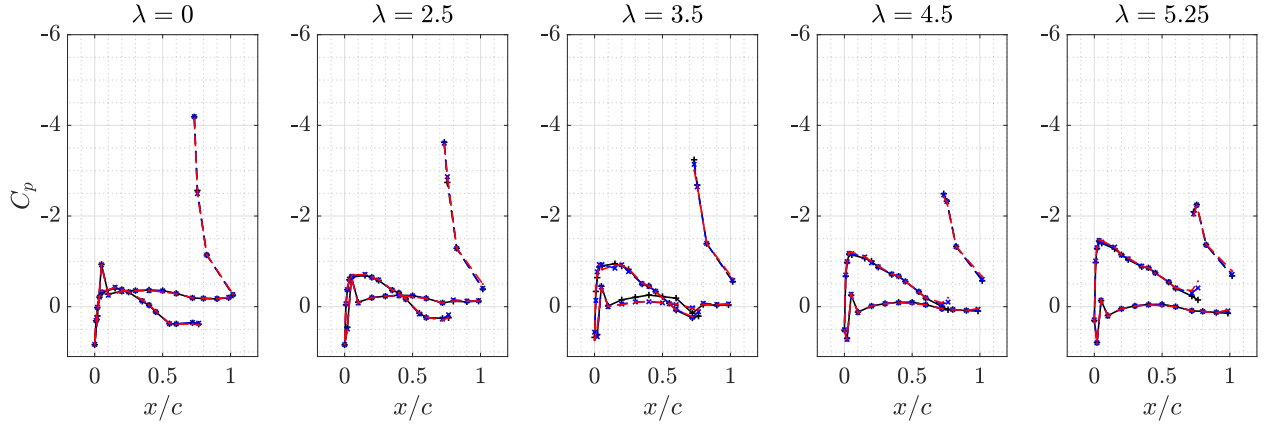

(b) C_p vs x/c for various λ at $\delta_T = 45°$

Figure 3.15: C_p vs x/c distributions for each row of pressure taps at $\alpha = 4°$ for various δ_T and λ values at $Re_c = 0.75 \times 10^6$

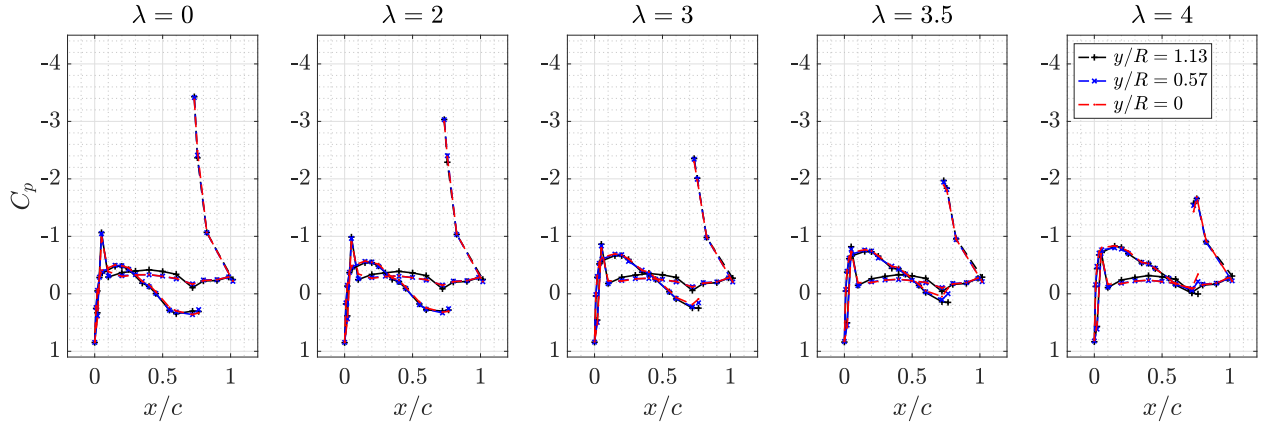

(a) C_p vs x/c for various λ at $\delta_T = 5.19°$

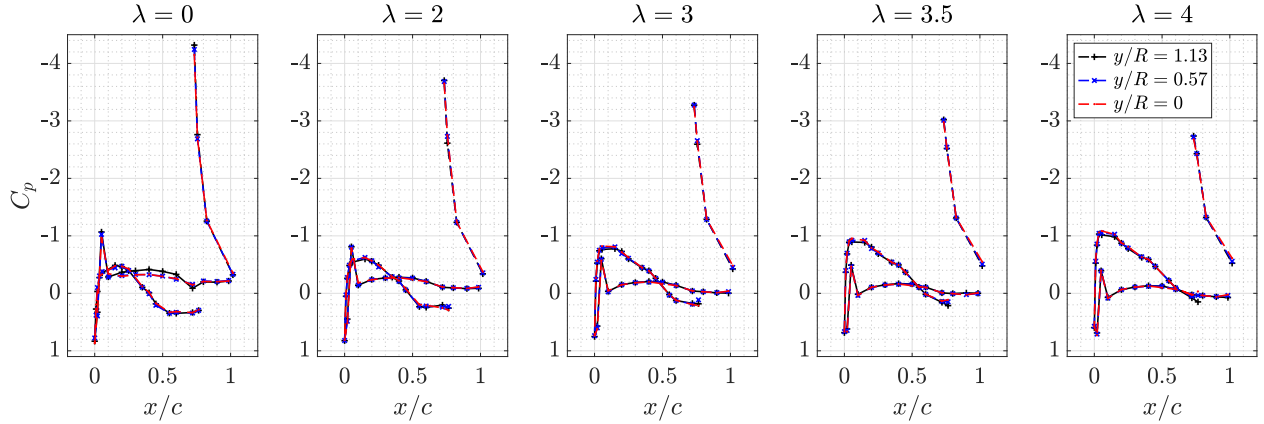

(b) C_p vs x/c for various λ at $\delta_T = 45°$

Figure 3.16: C_p vs x/c distributions for each row of pressure taps at $\alpha = 4°$ for various δ_T and λ values at $Re_c = 1.0 \times 10^6$

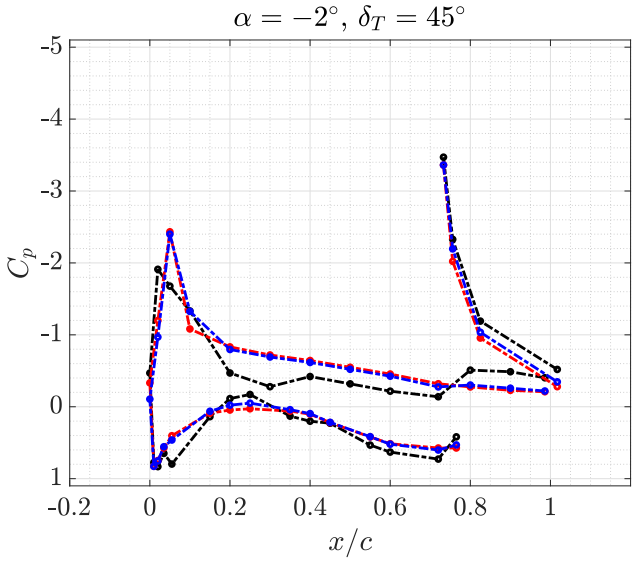

(a) C_p vs x/c for $\delta_T = 45°$ at $\alpha = -2°$

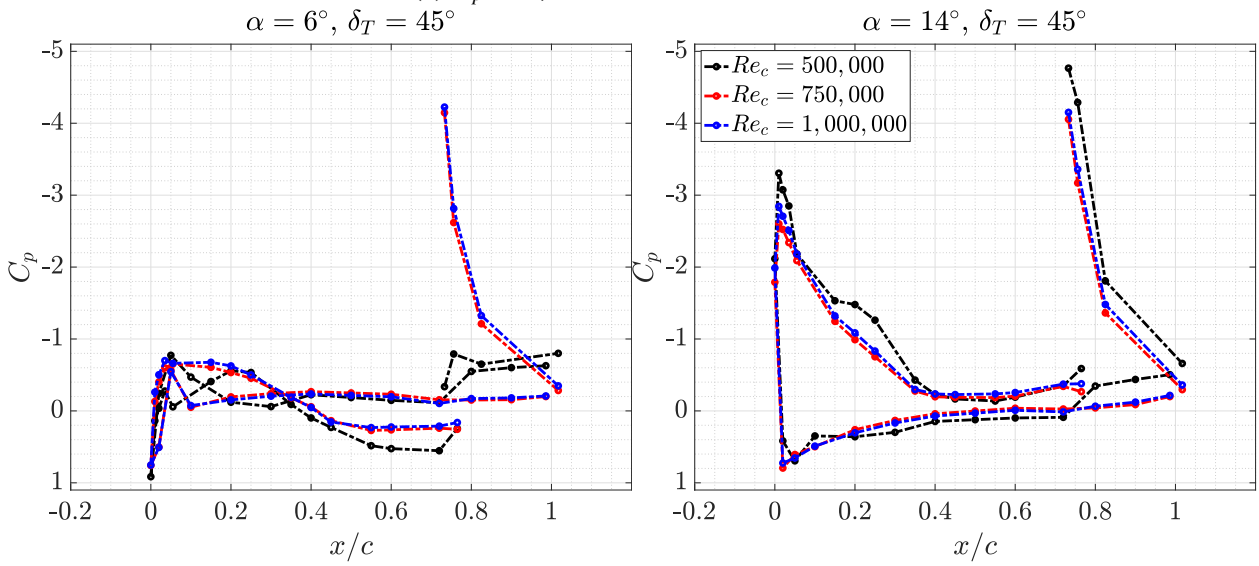

(b) C_p vs x/c for $\delta_T = 45°$ at $\alpha = 6°$

(c) C_p vs x/c for $\delta_T = 45°$ at $\alpha = 14°$

Figure 3.17: C_p vs x/c for the $y/R = 0$ row at $Re = 0.5 \times 10^6$, 7.5×10^6, and 1.0×10^6 for the windmilling case

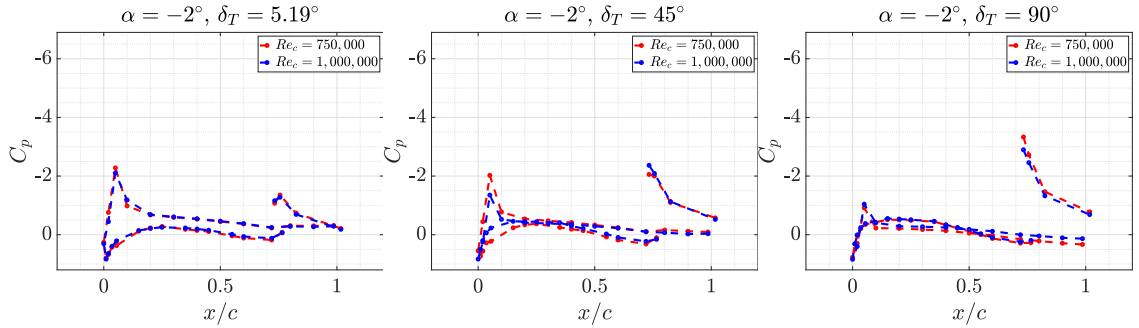

(a) $\delta_T = 5.19°$ at $\alpha = -2°$ (b) $\delta_T = 45°$ at $\alpha = -2°$ (c) $\delta_T = 90°$ at $\alpha = -2°$

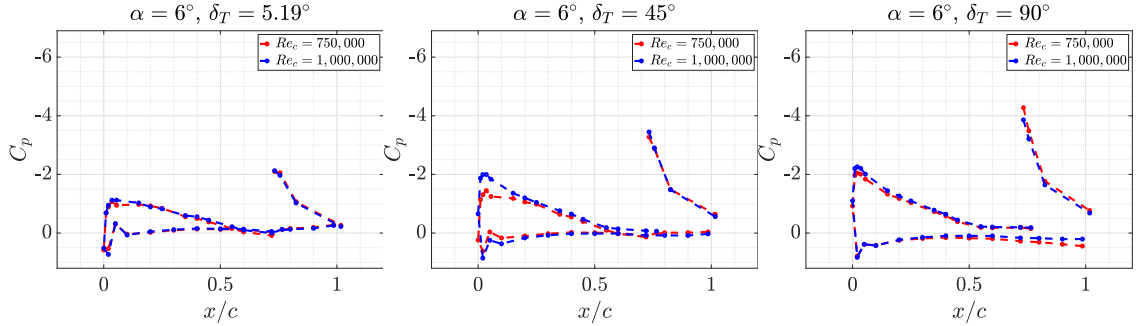

(d) $\delta_T = 5.19°$ at $\alpha = 6°$ (e) $\delta_T = 45°$ at $\alpha = 6°$ (f) $\delta_T = 90°$ at $\alpha = 6°$

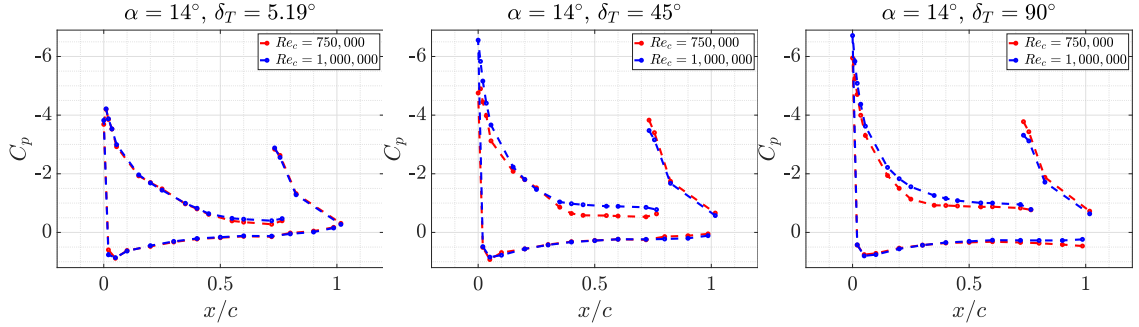

(g) $\delta_T = 5.19°$ at $\alpha = 14°$ (h) $\delta_T = 45°$ at $\alpha = 14°$ (i) $\delta_T = 90°$ at $\alpha = 14°$

Figure 3.18: C_p vs x/c for the $y/R = 0$ row for the $\lambda = 3.5$ case at $Re_c = 0.75 \times 10^6$ and 1.0×10^6 for a range of δ_T and α

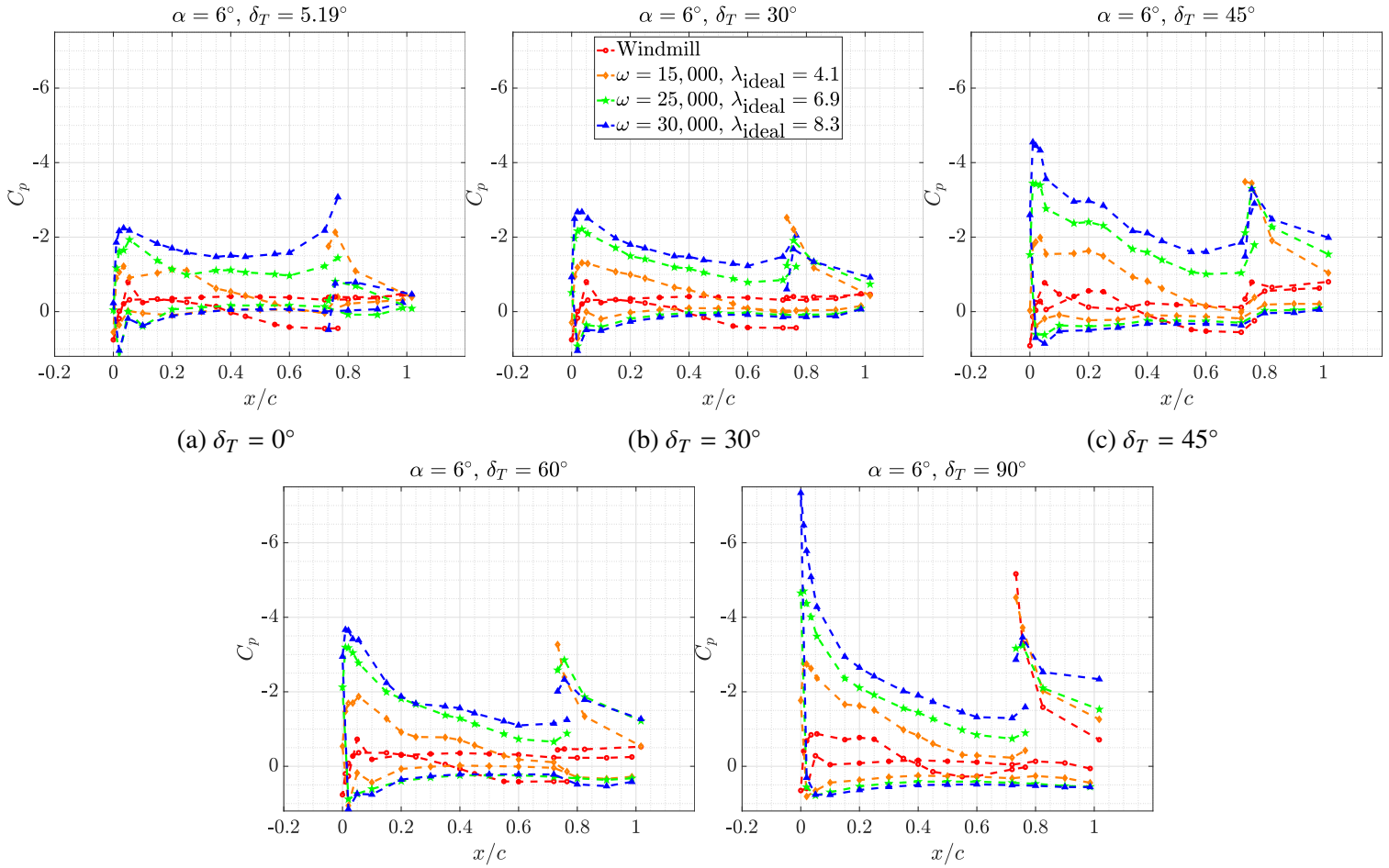

(a) $\delta_T = 0°$ (b) $\delta_T = 30°$ (c) $\delta_T = 45°$

(d) $\delta_T = 60°$ (e) $\delta_T = 90°$

Figure 3.19: C_p vs x/c for a sweep of ω for various δ_T at $\alpha = 6°$ and $Re_c = 0.5 \times 10^6$

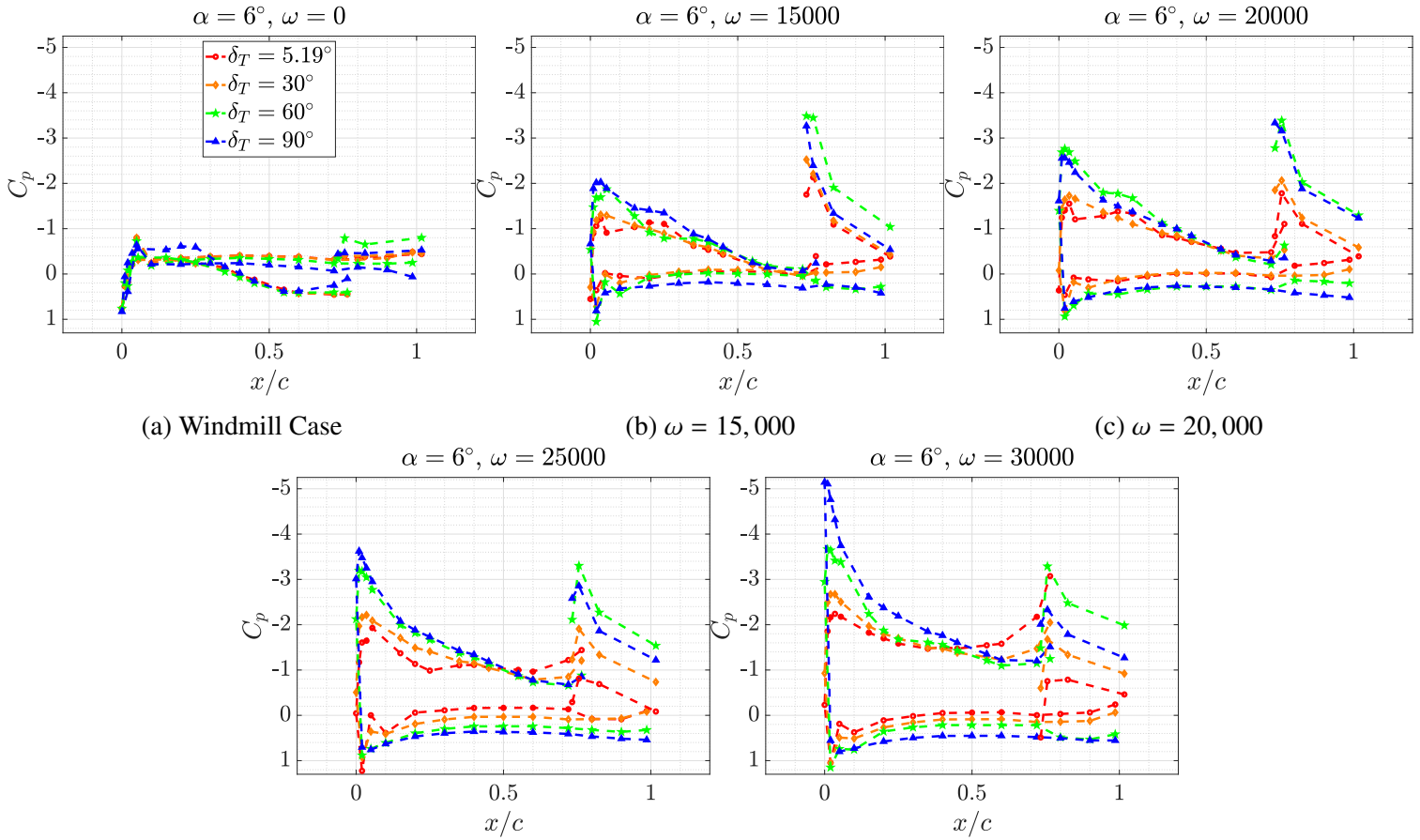

(a) Windmill Case (b) $\omega = 15,000$ (c) $\omega = 20,000$

(d) $\omega = 25,000$ (e) $\omega = 30,000$

Figure 3.20: C_p vs x/c for a sweep of δ_T for various ω at $\alpha = 6°$ and $Re_c = 0.5 \times 10^6$

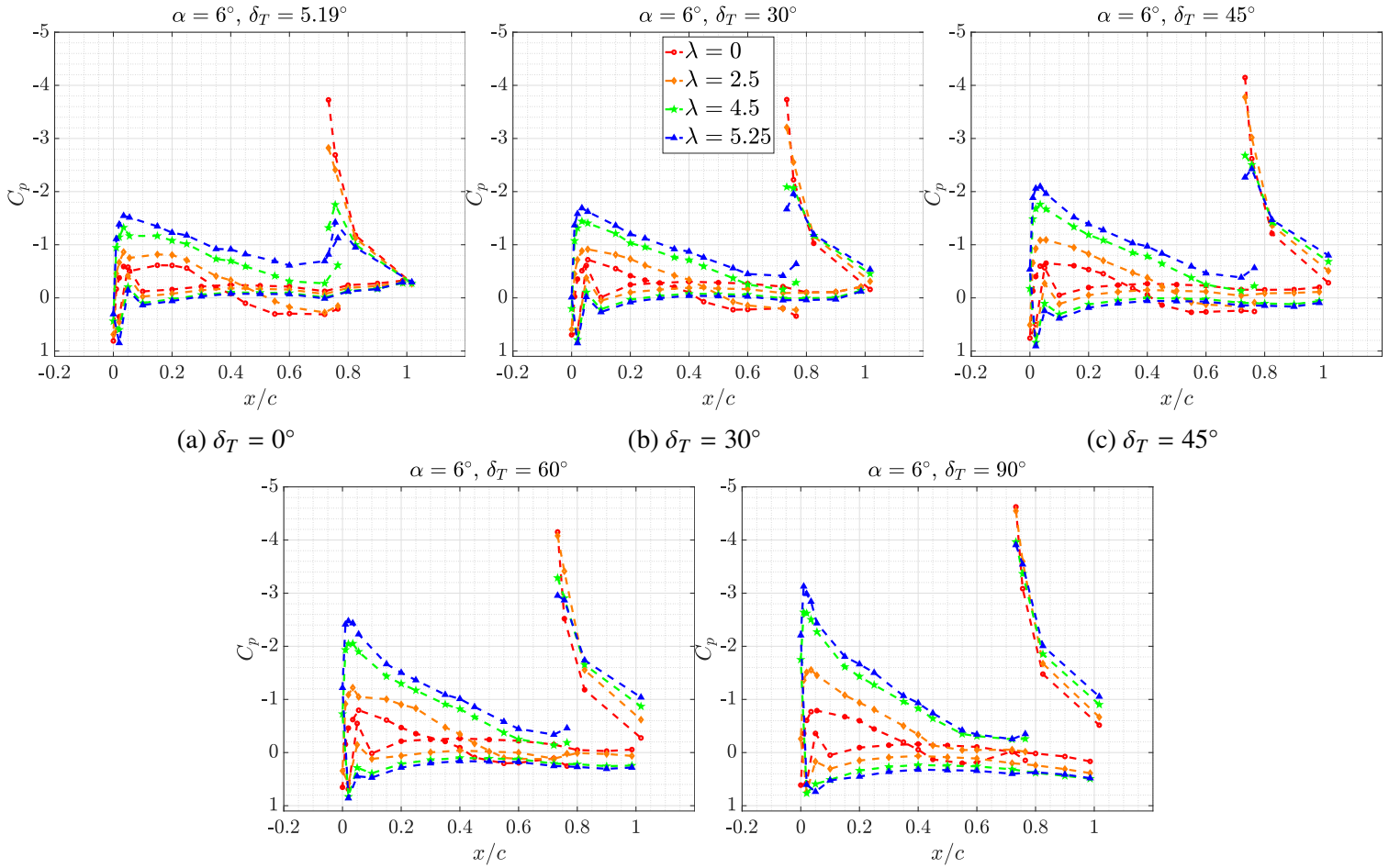

(a) $\delta_T = 0°$ (b) $\delta_T = 30°$ (c) $\delta_T = 45°$

(d) $\delta_T = 60°$ (e) $\delta_T = 90°$

Figure 3.21: C_p vs x/c for the $y/R = 0$ row for a sweep of λ for various δ_T at $\alpha = 6°$ and $Re_c = 0.75 \times 10^6$

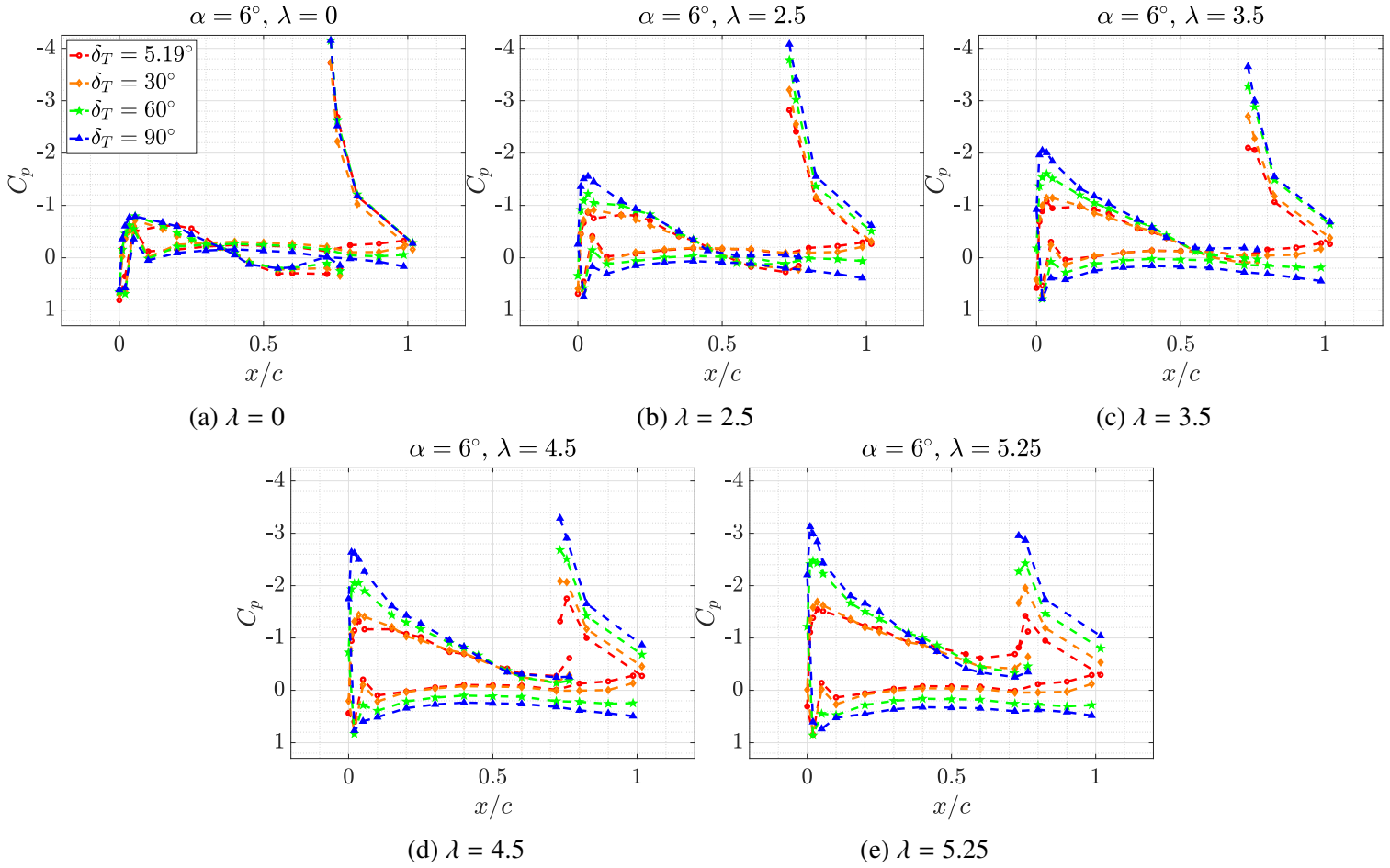

(a) $\lambda = 0$ (b) $\lambda = 2.5$ (c) $\lambda = 3.5$

(d) $\lambda = 4.5$ (e) $\lambda = 5.25$

Figure 3.22: C_p vs x/c for the $y/R = 0$ row for a sweep of δ_T for various λ at $\alpha = 6°$ and $Re_c = 0.75 \times 10^6$

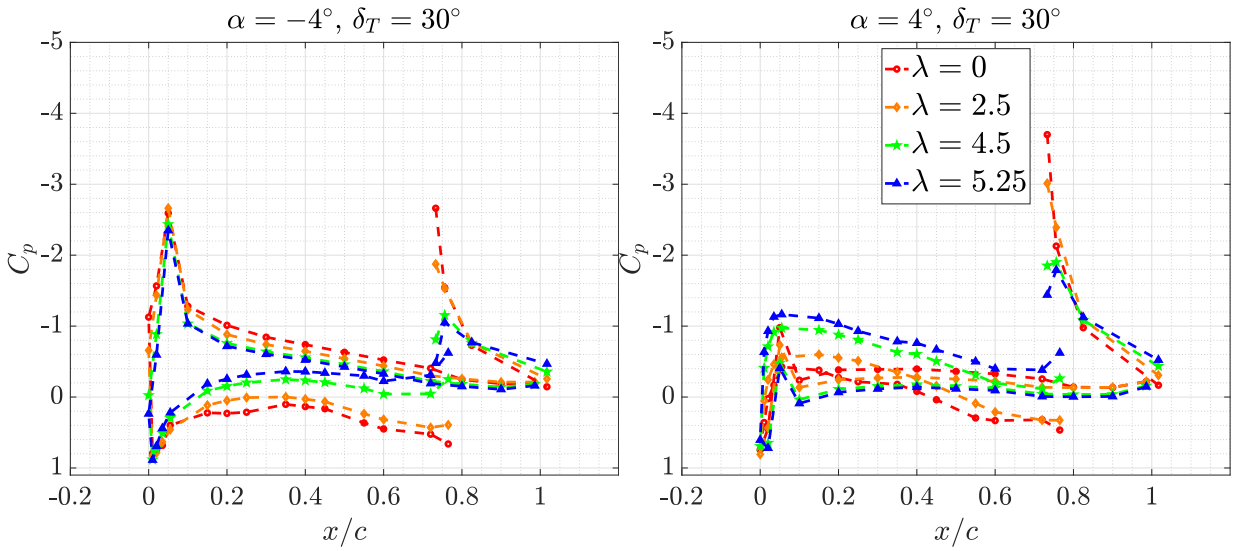

(a) C_p vs x/c for $\delta_T = 30°$ at $\alpha = -4°$

(b) C_p vs x/c for $\delta_T = 30°$ at $\alpha = 4°$

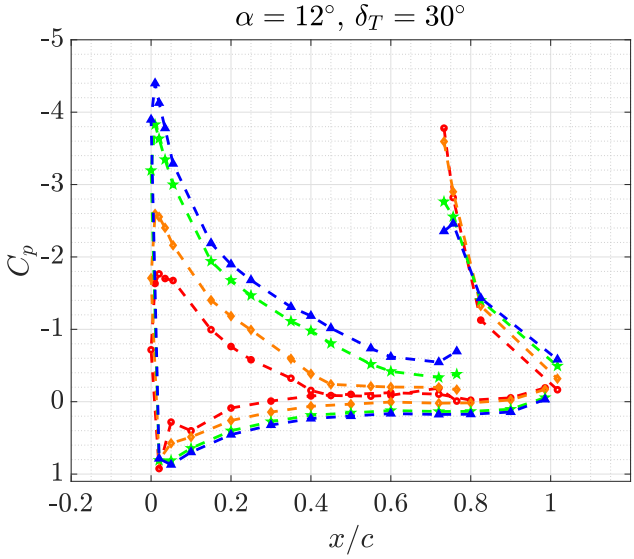

(c) C_p vs x/c for $\delta_T = 30°$ at $\alpha = 12°$

Figure 3.23: C_p vs x/c for the $y/R = 0$ row at $Re = 0.75 \times 10^6$ across a sweep of λ at various α

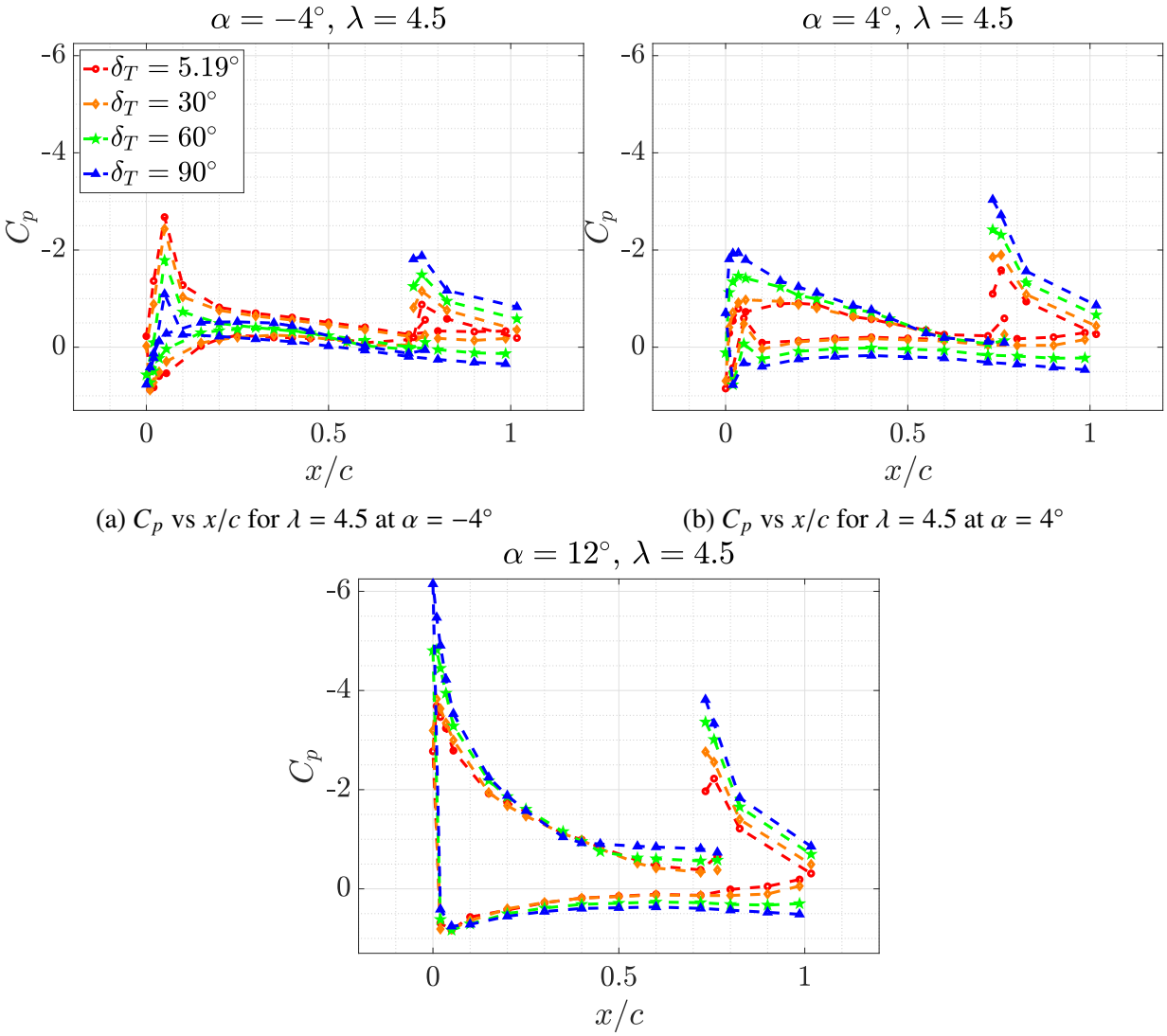

(a) C_p vs x/c for $\lambda = 4.5$ at $\alpha = -4°$

(b) C_p vs x/c for $\lambda = 4.5$ at $\alpha = 4°$

(c) C_p vs x/c for $\lambda = 4.5$ at $\alpha = 12°$

Figure 3.24: C_p vs x/c for the $y/R = 0$ row at $Re = 0.75 \times 10^6$ across a sweep of δ_T at various α

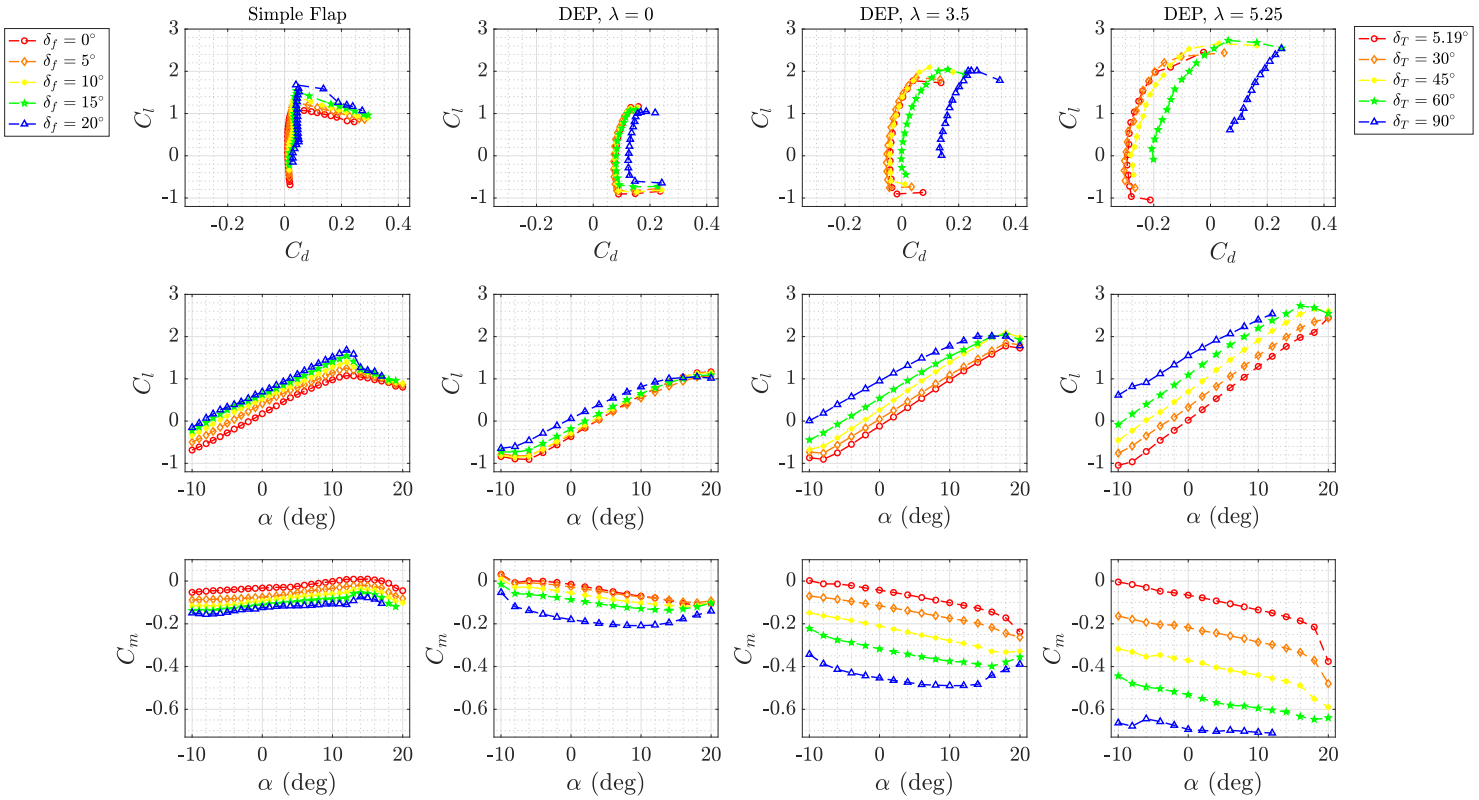

Figure 3.25: Lift, drag, and quarter-chord pitching moment polars for the S8036 airfoil and vectored DEP airfoil for various flap deflections and thrust deflection angles at $Re_c = 1.0 \times 10^6$ and $Re_c = 0.75 \times 10^6$, respectively

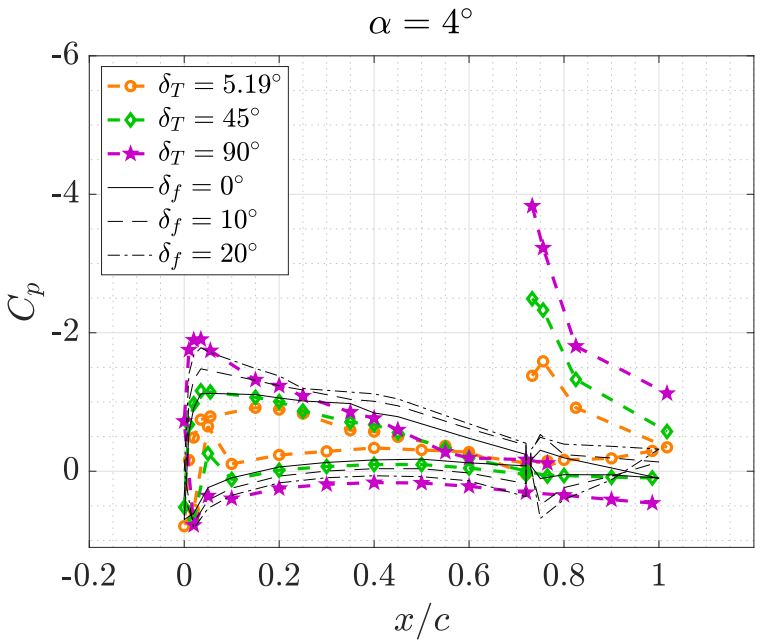

(a) C_p vs x/c at $\alpha = 4°$

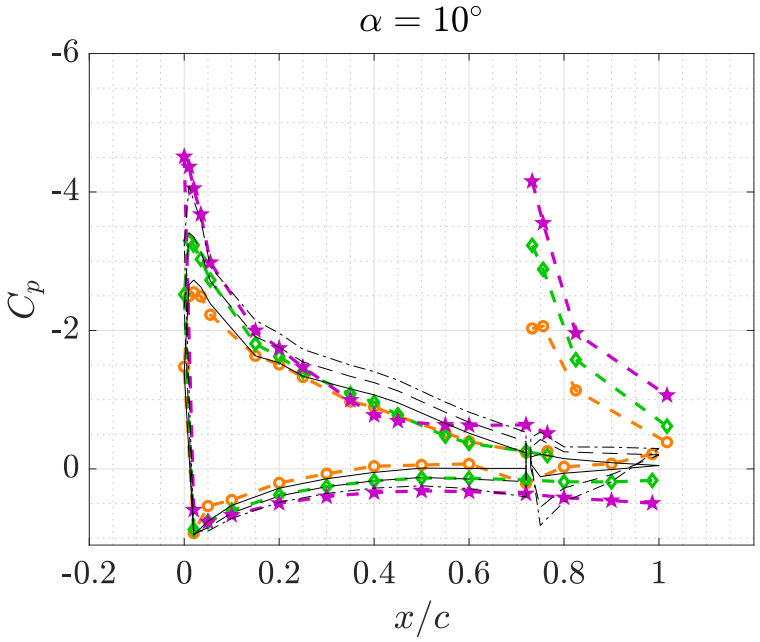

(b) C_p vs x/c at $\alpha = 10°$

Figure 3.26: Pressure distributions of the baseline airfoil at $Re_c = 1.0 \times 10^6$ and vectored DEP model at $Re_c = 0.75 \times 10^6$ for various flap and thrust deflection angles at a) $\alpha = 4°$ and b) $\alpha = 10°$

Chapter 4

Conclusions

4.1 Summary & Conclusions

The aero-propulsive characteristics and performance of a quasi-2D, distributed ducted fan propulsion system were experimentally investigated in the 2.8-ft $\times$ 4-ft low speed wind tunnel. The goal of this investigation was to determine the steady, aero-propulsive effects of vectored thrust from a distributed propulsion system. Net stream-wise and stream-normal force, quarter chord pitching moment, and pressure data were collected as a function of angle of attack, fan tip speed ratio, and thrust deflection at multiple Reynolds numbers in order to fully characterize the aerodynamic performance and surface pressure distributions of the system. Identifying key trends and their underlying mechanisms will allow for the informed study of a vectored distributed propulsion system as a means for achieving simultaneous requirements of vertical thrust, high lift, and forward propulsion using a range of deflections of the propulsion system jet efflux.

The effect of thrust deflection on the stream-normal and stream-wise forces was seen to depend on the tip speed ratio of the ducted fans. Overall, deflection of the thrust led to an increase in stream-normal force when the aero-propulsive system was operating. However, at low tip speed ratios, this observed increase in stream-normal force only occurs up to a certain point, after which further thrust deflection does not appreciably increase stream-normal force, and results in a higher net stream-wise force, indicating a larger contribution of drag to this term. At high tip speed ratios, increasing thrust deflection can be seen to increase stream-normal force up to the highest thrust deflection angle tested. This correlation between tip speed ratio and the increase in stream-normal

force with thrust deflection could be attributed to the ability of the aero-propulsive system to sustain attached flow across adverse pressure gradients associated with high deflection angles, which would be expected to increase with tip speed ratio.

Increasing tip speed ratio was observed to produce an increase in the C_{l_α} slope for a given thrust deflection angle, and this trend was seen to decrease with increased thrust deflection angles. This expected behavior can be attributed to the contribution of thrust from the aero-propulsive system to the stream-normal direction. Variation in fan tip speed ratio was seen to allow the system to achieve a wide range of conditions ranging from positive to negative net stream-normal force at all angles of thrust deflection aside from the fully deflected case. Thrust deflection was found to have a significant effect on the system pitching moment that was further amplified by fan tip speed ratio. The system exhibited a high degree of variation in pitching moment coefficient, achieving variations of almost an order of magnitude difference between the undeflected and the fully deflected cases. The coupling between increased stream-normal force and pitching moment to fan tip speed ratio presents a significant design consideration for such systems.

Pressure data were collected in three chordwise rows that spanned approximately one fan radius across the region occupied by the center fan in the DEP system. The collected data revealed a generally negligible degree of spanwise variation in the airfoil and nacelle pressure distributions. The most significant source of spanwise pressure variation was observed across the highest fan tip speed ratios, which induced lower pressures in the spanwise plane along the fan centerline in the region immediately upstream of the fan inlet. Overall, increased thrust vectoring was found to significantly increase the suction peak of both the airfoil and nacelle as well as increase pressure on the airfoil lower surface. At high thrust deflection angles and relatively low tip speed ratios, constant pressure regions associated with flow separation were observed on the airfoil upper surface. However, at higher tip speed ratios, the system was able to sustain a strong adverse pressure gradient up to the EDF inlet. Increased tip speed ratio for a fixed thrust deflection angle was seen to produce an overall decrease in the airfoil upper surface pressure as well as a decrease in the nacelle suction peak. Even at high tip speed ratios, a significant suction peak was observed on the nacelle at low and negative angles of attack, indicating that the nacelle plays a significant role in the observed decrease in zero lift angle of attack with increased thrust deflection angle.

The aero-propulsive characteristics of the DEP system were also compared to the aerodynamic performance of a baseline airfoil model which utilized the same main airfoil element and a 25%-chord simple flap element. At moderate and high tip speed ratios, the DEP system was observed to achieve higher maximum stream-normal coefficients than the simple flap element. In addition, the ability of the DEP system to delay flow separation at high tip speed ratios led to significantly lower zero lift angles of attack than the simple flap system at high thrust deflection angles. Overall, deflection of the simple flap produced uniform increases in stream-normal coefficient, whereas thrust deflection at a constant tip speed ratio in the DEP system produced increases in stream-normal coefficient as well as an opposite effect to tip speed ratio on lift curve slope. The DEP system exhibited similar magnitude pitching moment coefficients as the simple flap system at thrust deflection angles in the windmill case and at low thrust deflection angles at higher tip speed ratios. At higher thrust deflection angles, the DEP system was observed to produce pitching moment coefficients that reached more than twice the magnitude of the simple flap case.

The unique effects of thrust vectoring on the aero-propulsive characteristics of the DEP system produce a novel set of design challenges and potential applications. The variation in pitching moment resulting from thrust deflection at high tip speed ratios could present a significant stability and control challenge. However, the ability of the system to sustain a range of both positive and negative C_d values for the same, high C_l values at thrust deflection angles greater than 45° and various tip speed ratios could be suitable in applications where horizontal acceleration or deceleration with constant lift performance may be desirable. In addition, the significant reduction in zero lift angle of attack due to the presence of a suction peak on the nacelle at low angles of attack could enable operation at lower angles of attack than a conventional flapped system.

References

[1] Rubin Lineberger et al. 'Elevating the future of mobility'. In: *Deloitte Insights*.

[2] John P. Campbell. 'Overview of Powered-Lift Technology'. In: *Joint Institute for Acoustics and Flight Sciences*. The George Washington University. DOI: N78-24047. URL: https://ntrs.nasa.gov/api/citations/19780016104/downloads/19780016104.pdf.

[3] F. Steven Yaros, Matthew G. Sexstone and Lawrene D. et al Huebner. 'Syngergistic Airframe-Propulsion Interacitons and Integrations'. In: *NASA TMK-1998-207644*. DOI: 10.2514/6.2015-3162. eprint: https://arc.aiaa.org/doi/pdf/10.2514/6.2015-3162. URL: https://arc.aiaa.org/doi/abs/10.2514/6.2015-3162.

[4] Alex M. Stoll et al. 'Drag Reduction Through Distributed Electric Propulsion'. In: *14th AIAA Aviation Technology, Integration, and Operations Conference*. DOI: 10.2514/6.2014-2851. eprint: https://arc.aiaa.org/doi/pdf/10.2514/6.2014-2851. URL: https://arc.aiaa.org/doi/abs/10.2514/6.2014-2851.

[5] Mike F. Kerho. 'Aero-Propulsive Coupling of an Embedded, Distributed Propulsion System'. In: *33rd AIAA Applied Aerodynamics Conference*. DOI: 10.2514/6.2015-3162. eprint: https://arc.aiaa.org/doi/pdf/10.2514/6.2015-3162. URL: https://arc.aiaa.org/doi/abs/10.2514/6.2015-3162.

[6] B. W. McCormick. *Aerodynamics of V/STOL Flight*. 2nd ed. Academic Press, 1967.

[7] R. E. Spitzer. 'Predicted flight characteristics of the augmentor wing jet STOL research aircraft'. In: *NASA-CR-114463*. DOI: 19720020367.

[8] G.H. Laub. 'Low Speed Wind Tunnel Tests on a One-Seventh Scale Model of the H.126 Jet Flap Aircraft'. In: *NASA-TM X-62,433*. DOI: 19750016650.

[9] M.H. Roe and D.J. Renselaer. *STOL Tactical Aircraft Investigation, Externally Blown Flap. Volume II. Design Compendium*. Vol. 2. Rockwell International Corporation, 1973.

[10] William C. Jr Sleeman and William C. Hohlweg. 'Low-speed wind-tunnel investigation of a four-engine upper surface blown model having a swept wing and rectangular and D-shaped exhaust nozzles'. In: *NASA Technical Note*. NASA TN D-8061, 1975, pp. –.

[11] John K Wimpress and Conrad F. Newberry. *The YC-14 STOL Prototype: Its Design, Development and Flight Test*. 1st ed. Reston: AIAA, 1998.

[12] D. R Agrawal et al. 'Wind Tunnel Testing of a Blown Flap Wing'. In: *AIAA AVIATION Forum*. Dallas, TX: AIAA, 2019, pp. –. DOI: 10.2514/6.2019-3170.

[13] Hyun D. Kim, Aaron T. Perry and Phillip J. Ansell. 'A Review of Distributed Electric Propulsion Concepts for Air Vehicle Technology'. English (US). In: *2018 AIAA/IEEE Electric Aircraft Technologies Symposium, EATS 2018*. 2018 AIAA/IEEE Electric Aircraft Technologies Symposium, EATS 2018. 2018 AIAA/IEEE Electric Aircraft Technologies Symposium, EATS 2018 ; Conference date: 12-07-2018 Through 14-07-2018. United States: Institute of Electrical and Electronics Engineers Inc., Nov. 2018, pp. 2414–2426. DOI: 10.2514/6.2018-4998.

[14] Leroy H. Smith. 'Wake ingestion propulsion benefit'. In: *Journal of Propulsion and Power* 9.1 (1993), pp. 74–82. DOI: 10.2514/3.11487. eprint: https://doi.org/10.2514/3.11487. URL: https://doi.org/10.2514/3.11487.

[15] Devaiah Nalianda and Riti Singh. 'Turbo-electric distributed propulsion – opportunities, benefits and challenges'. In: *Aircraft Engineering and Aerospace Technology: An International Journal* 86.6 (Jan. 2014). Ed. by Riti Singh, pp. 543–549. ISSN: 0002-2667. DOI: 10.1108/AEAT-03-2014-0035. URL: https://doi.org/10.1108/AEAT-03-2014-0035.

[16] S. Clarke et al. 'X-57 power and command system design'. In: *2017 IEEE Transportation Electrification Conference and Expo (ITEC)*. 2017, pp. 393–400. DOI: 10.1109/ITEC.2017.7993303.

[17] Andrew T. Wick, John R. Hooker and Cale H. Zeune. 'Integrated Aerodynamic Benefits of Distributed Propulsion'. In: *53rd AIAA Aerospace Sciences Meeting*. 2015, pp. –. DOI: 10.2514/6.2015-1500. eprint: https://arc.aiaa.org/doi/pdf/10.2514/6.2015-1500. URL: https://arc.aiaa.org/doi/abs/10.2514/6.2015-1500.

[18] Aaron T. Perry, Phillip J. Ansell and Michael Kerho. 'Aero-Propulsive and Propulsor Cross-Coupling Effects on a Distributed Propulsion System'. In: *2018 AIAA Aerospace Sciences Meeting*. DOI: 10.2514/6.2018-2051. eprint: https://arc.aiaa.org/doi/pdf/10.2514/6.2018-2051. URL: https://arc.aiaa.org/doi/abs/10.2514/6.2018-2051.

[19] M. Kerho. 'Turboelectric Distributed Propulsion Test Bed Aircraft'. In: *AIAA Paper 2016–3690* (June 2016). DOI: 10.2514/6.2016-3690.

[20] Aaron T. Perry, Timothy Bretl and Phillip J. Ansell. 'System Identification and Dynamics Modeling of a Distributed Electric Propulsion Aircraft'. In: *AIAA Aviation 2019 Forum*. 2019, pp. –. DOI: 10.2514/6.2019-3086. eprint: https://arc.aiaa.org/doi/pdf/10.2514/6.2019-3086. URL: https://arc.aiaa.org/doi/abs/10.2514/6.2019-3086.

[21] J.B. Barlow, W.H. Jr. Rae and A. Pope. *Low-Speed Wind Tunnel Testing*. 3rd ed. John Wiley & Sons, Inc., 1999.

[22] C. Lyon et al. *Summary of Low-Speed Airfoil Data*. Vol. 3. Virginia Beach, Virginia: SoarTech Publications, 1997.

[23] Kristy Hansen et al. 'Laminar separation bubble effect on the lift curve slope of an airfoil'. In: 2014.

[24] S.J. Kline and F.A. McClintock. 'Describing Uncertainties in Single Sample Experiments'. In: *Mechanical Engineering* 3-8 (1953).

[25] Robert J. Moffat. 'Describing the uncertainties in experimental results'. In: *Experimental Thermal and Fluid Science* 1.1 (1988), pp. 3–17. ISSN: 0894-1777. DOI: https://doi.org/10.1016/0894-1777(88)90043-X. URL: https://www.sciencedirect.com/science/article/pii/089417778890043X.

[26] J. P. (Jack Philip) Holman. *Experimental methods for engineers*. English. 7th ed. McGraw-Hill series in mechanical engineering. Boston: McGraw-Hill, 2001. URL: http://catdir.loc.gov/catdir/enhancements/fy0820/00036059-d.html.

Appendix A

Uncertainty Analysis

Aerodynamic performance and pressure data were acquired using multiple instruments. In addition, some presented results were calculated using primary measurements of various parameters such as atmospheric pressure or temperature. Therefore, analyzing the uncertainties of the collected data is important in establishing a comprehensive perspective of the results. Significant errors in data can occur and be noted as a result of identifiable events, such as an error in a pressure measurement sensor or insufficient battery voltage. Two additional sources of error and therefore uncertainty are precision and bias errors. Precision errors are characterized by a random nature, and generally occur with a zero mean. Bias errors, also referred to as "fixed errors", correspond to repeatable, quantifiable errors that are typically associated with measurement capabilities or the accurate calibration of measuring equipment. A review and quantification of uncertainties in the collected experimental data is presented in this chapter.

In order to collect data that span a meaningful space of test parameters, primarily EDF operating condition (denoted by λ or ω) at multiple thrust deflections δ_T over a range of angles of attack, in a limited amount of time, most test cases were not repeated. As a result, a single-sample uncertainty analysis provided by Kline and McClintock [24] and summarized by Moffat [25] was applied to the results. The method consists of computing the uncertainty of a result, R, as a root-sum square combination of the effects of its individual and independent inputs, x_i. The effects of an individual input on the result, δR_{x_i}, which was assumed to be small, can be estimated as:

$$\delta R_{x_i} = \frac{\delta R}{\delta x_i} \delta x_i \tag{A.1}$$

The overall uncertainty of the result, δR, can thus be calculated as the root-sum square of the effects of each input:

$$\delta R = \left(\sum_{i=1}^{N} \left(\frac{\delta R}{\delta x_i} \delta x_i \right)^2 \right)^{1/2} \tag{A.2}$$

It should be noted that Eqn. A.2 relies on three key assumptions: each measurement is independent, repeated measurements would display Gaussian distributions, and the probabilities of uncertainty in each measurement are the same. It should be noted that the third assumption arises from the nature of Kline and McClintock's method, which provides the option for specifying the odds of the uncertainty of a result or measurement being larger than $\pm\delta R$. According to Holman, the specification of such odds can only be made by the experimenter based on the total laboratory experience [26]. Upon reflection on the author's total laboratory experience to date, it was decided that more experience was needed before any odds could be specified. Therefore, the odds of all uncertainties were assumed to be equal for the present study. Given that the three conditions are true, the value δR can be taken to represent 2σ, where σ is the standard deviation of the population of possible measurements of R.

The absolute uncertainties of primary measurements based on instrument manufacturer information are summarized in Table A.1 and sample uncertainties from data acquired at $\alpha = 4^\circ$ during the $\delta_T = 45^\circ$, $\lambda = 4.5$, $Re_c = 0.75 \times 10^6$ case are presented. The calculated absolute uncertainties of data from a $Re = 0.75 \times 10^6$ and $Re = 1.0 \times 10^6$ case are summarized in Tables A.2 and A.3, respectively. The derivations of the expressions for uncertainty are presented in the following sections. Uncertainties in the airfoil geometric properties such as chord, span, and quarter chord location were based on the manufacturing tolerances associated with the SLA 3D printing method used to fabricate the airfoil model and DEP flap. It should be noted that given the relatively high RPM values at which the EDFs were operating, the uncertainty of EDF RPM estimation was deemed negligible, as it would have been orders of magnitude less than the RPM measurements. Therefore, the natural variation in RPM of the EDFs due to slight variations in flow conditions and other physical effects associated with imperfect, real life conditions was taken as the uncertainty

of RPM. This variation was observed to be at most 50 RPM during experiments. The remaining uncertainties were obtained from information provided by the manufacturer of each instrument.

Parameter	Absolute Uncertainty	Reference Value	Rel. Uncertainty (%)
c	±0.005 in	18 in	±0.0278
b	±0.005 in	33.6 in	±0.0149
$X_{c/4}$	±0.005 in	4.5 in	±0.111
$Y_{c/4}$	±0.005 in	??	??
T_{amb}	±1.8 °R	532.15°R	±0.338
α	±0.02°	3.999°	±0.5
P_{amb}	±0.008 psi	14.418 psi	±0.0555
$P_{\pm 5 \text{ psid module}}$	±0.0036 psid	−0.148376 psid	±2.42627
$P_{\pm 1 \text{ psid module}}$	±0.0014 psid	−0.043317 psid	±3.2320
$(P_{ts} - P_{ss})$	±0.0036	0.063434 psid	±5.675
F_N	±0.09 lbf	37.944139 lbf	±0.5180
F_A	±0.0135 lbf	−7.376039 lbf	±0.183
M	±0.0135 ft·lbf	−18.829876 ft·lbf	±0.07160
ω	±50 rpm	25,011.1 rpm	±0.200

Table A.1: Sample uncertainties for primary measurements taken at $\alpha = 4°$ and $Re_c = 0.75 \times 10^6$ for the $\delta_t = 45°$, $\lambda = 4.5$ case

Parameter	Absolute Uncertainty	Reference Value	Rel. Uncertainty (%)
ρ_∞	7.7933×10^{-6} slug/ft^3	2.2708×10^{-3} slug/ft^3	±0.343
q_∞	0.001864 psi	0.063434 psi	±2.9383
U_∞	2.5728 ft/s	86.561 ft/s	±2.9723
μ	1.9346×10^{-9}	3.8162×10^{-7}	±0.507
Re_c	23,587	772,605	±3.053
L	0.1302 lbf	38.366 lbf	±0.3393
D	0.09540 lbf	−4.7119 lbf	±2.025
$M_{c/4}$	0.44896 ft·lbf	−18.830ft·lbf	±2.384
C_l	0.0051075	0.960412	±0.5318
C_d	0.003425	−0.12028	±2.847
C_m	0.008831	−0.31745	±2.782
C_p	0.0333458	−0.405776	±8.218
λ	0.133	4.467	±2.98

Table A.2: Sample uncertainties for primary measurements taken at $\alpha = 4°$ and $Re_c = 0.75 \times 10^6$ for the $\delta_t = 0°$, $\lambda = 4.5$ case

Parameter	Absolute Uncertainty	Reference Value	Rel. Uncertainty (%)
ρ_∞	7.7612×10^{-6} slug/ft^3	2.2610×10^{-3} slug/ft^3	±0.343
q_∞	0.001864 psi	0.11518 psi	±1.618
U_∞	1.9214 ft/s	115.962 ft/s	±1.657
μ	1.9352×10^{-9}	3.8082×10^{-7}	±0.508
Re_c	18,548	1,032,740	±1.798
L	0.1086 lbf	23.4444 lbf	±0.4630
D	0.06290 lbf	−3.0561 lbf	±2.0582
$M_{c/4}$	0.4221 ft·lbf	−27.5202ft·lbf	±1.5338
C_l	0.8361	0.336921	±0.5318
C_d	0.003425	−0.043920	±2.847
C_m	0.004461	−0.069772	±6.3937
C_p	0.0086827	−0.444303	±1.9542
λ	0.0557	3.480107	±1.599

Table A.3: Sample uncertainties for primary measurements taken at $\alpha = 4°$ and $Re_c = 1.0 \times 10^6$ for the $\delta_t = 45°$, $\lambda = 4.5$ case

A.1 Uncertainty in Flow Measurements

Atmospheric and flow parameters that were presented and used for calculation of results include ambient density, ambient pressure, free stream dynamic pressure, and dynamic viscosity. Ambient density was calculated using measurements of ambient pressure and ambient temperature according to Eq. 2.4. The uncertainty of the ambient density was thus calculated based on the effects of each measured input on the result and their respective uncertainties:

$$\partial\rho_\infty = \left(\left(\frac{\partial\rho_\infty}{\partial P_{\text{amb}}}\partial P_{\text{amb}}\right)^2 + \left(\frac{\partial\rho_\infty}{\partial T_{\text{amb}}}\partial T_{\text{amb}}\right)^2\right)^{1/2} \tag{A.3}$$

$$\frac{\partial\rho_\infty}{\partial P_{\text{amb}}} = \frac{1}{RT_{\text{amb}}}$$

$$\frac{\partial\rho_\infty}{\partial T_{\text{amb}}} = \frac{-P_{\text{amb}}}{RT_{\text{amb}}^2}$$

Ambient pressure and temperature were measured directly, and the uncertainties of each value, ∂P_{amb} and ∂T_{amb}, are presented in Table A.1. As stated in Section 2.1.1, the flow was assumed to be incompressible for the present study. Therefore, an expression for dynamic pressure can be derived from Eq. 2.2:

$$\frac{1}{2}\rho_\infty U_{\text{ss}}^2 + P_{\text{ss}} = \frac{1}{2}\rho_\infty U_{\text{ts}}^2 + P_{\text{ts}} \tag{A.4}$$

$$q_\infty = \frac{1}{2}\rho_\infty U_{\text{ts}}^2 = \frac{P_{\text{ss}} - P_{\text{ts}}}{1 - \left(\frac{A_{\text{ts}}}{A_{\text{ss}}}\right)^2} \tag{A.5}$$

As with the derivation of Eq. 2.3 for U_∞, the velocity at the tunnel settling section was assumed to be zero. A ±5 psid module was used to measure the pressure difference between P_{ss} and P_{ts}. It was assumed that the tunnel contraction ratio, $A_{\text{ts}}/A_{\text{ss}}$, had a negligible amount of uncertainty, or $\partial q_\infty / \partial(\frac{A_{\text{ts}}}{A_{\text{ss}}}) = 0$. As a result, the uncertainty of dynamic pressure can then be calculated using Eq. A.5, where the uncertainty of the pressure difference between the settling section and test section, $\partial(P_{ts} - P_{ss})$, is that of the ±5 psid pressure module shown in Table A.1:

$$\partial q_\infty = \left(\left(\frac{\partial q_\infty}{\partial(P_{ts} - P_{ss})}\partial(P_{ts} - P_{ss})\right)^2\right)^{1/2} \tag{A.6}$$

$$\frac{\partial q_\infty}{\partial(P_{ts} - P_{ss})} = \frac{1}{1 - \left(\frac{A_{\text{ts}}}{A_{\text{ss}}}\right)^2}$$

The uncertainty of freestream velocity can be similarily found to be:

$$\partial U_\infty = \left(\left(\frac{\partial U_\infty}{\partial\left(P_{ss} - P_{ts}\right)}\partial\left(P_{ss} - P_{ts}\right)\right)^2 + \left(\frac{\partial U_\infty}{\partial \rho_\infty}\partial\rho_\infty\right)^2\right)^{1/2} \tag{A.7}$$

$$\frac{\partial U_\infty}{\partial\left(P_{ss} - P_{ts}\right)} = \frac{1}{2}\sqrt{\frac{2}{\rho_\infty\left(1 - \left(\frac{A_{\text{ts}}}{A_{\text{ss}}}\right)^2\right)\left(P_{\text{ss}} - P_{\text{ts}}\right)}}$$

$$\frac{\partial U_\infty}{\partial \rho_\infty} = \frac{-1}{2\rho_\infty}\sqrt{\frac{2\left(P_{\text{ss}} - P_{\text{ts}}\right)}{\rho_\infty\left(1 - \left(\frac{A_{\text{ts}}}{A_{\text{ss}}}\right)^2\right)}}$$

The dynamic viscosity used to calculate Reynolds number according to Eq. 2.5 was calculated using Sutherland's formula:

$$\mu = \mu_0 \frac{T_0 + C}{T_{\text{amb}} + C} \left(\frac{T_{\text{amb}}}{T_0} \right)^{3/2} \tag{A.8}$$

$$\mu_0 = 3.58404 \times 10^{-7} \text{slug/ft-sec}$$

$$T_0 = 491.6^\circ\text{R}$$

$$C = 199.8^\circ\text{R}$$

Where μ_0, T_0, and C are known constants. The uncertainty of dynamic viscosity, $\partial\mu$, can be calculated using Eq. A.8 as:

$$\frac{\partial \mu}{\partial T_{\text{amb}}} = \frac{3}{2} \mu_0 \frac{T_0 + C}{T_{\text{amb}} + C} \left(\frac{T_{\text{amb}}^{1/2}}{T_0^{3/2}} \right)$$

$$\partial \mu = \left(\left(\frac{\partial \mu}{\partial T_{\text{amb}}} \partial T_{\text{amb}} \right)^2 \right)^{1/2} \tag{A.9}$$

Finally, from the equation used to calculate Reynolds number shown in Eq. 2.5, the uncertainty of Reynolds number can be found to be:

$$\partial Re_c = \left(\left(\frac{\partial Re_c}{\partial \rho_\infty} \partial \rho_\infty \right)^2 + \left(\frac{\partial Re_c}{\partial U_\infty} \partial U_\infty \right)^2 + \left(\frac{\partial Re_c}{\partial c} \partial c \right)^2 + \left(\frac{\partial Re_c}{\partial \mu_\infty} \partial \mu_\infty \right)^2 \right)^{1/2} \tag{A.10}$$

$$\begin{aligned}
\frac{\partial Re_c}{\partial \rho_\infty} &= \frac{U_\infty c}{\mu_\infty} \\
\frac{\partial Re_c}{\partial U_\infty} &= \frac{\rho_\infty c}{\mu_\infty} \\
\frac{\partial Re_c}{\partial c} &= \frac{\rho_\infty U_\infty}{\mu_\infty} \\
\frac{\partial Re_c}{\partial \mu_\infty} &= -\frac{\rho_\infty U_\infty c}{\mu_\infty^2}
\end{aligned} \tag{A.11}$$

A.2 Uncertainty in Performance Measurements

Force balance data in the form of chord-normal and chord-axial forces, F_N and F_A were rotated into the wind axis frame using angle of attack, α, to obtain lift and drag, L and D. These values were then nondimensionalized by q_∞ and airfoil geometry to obtain C_l and C_d as shown in

Eq. 2.10 and Eq. 2.11. Pitching moment, M, measured by the force balance was converted into quarter-chord pitching moment, $M_{c/4}$, as per Eq. 2.7. The uncertainties of F_A, F_N, M, α, $X_{c/4}$, $Y_{c/4}$, c, and b are summarized in Table A.1. Expressions for uncertainty of lift, drag, and quarter chord pitching moment are shown in Eq. A.12, A.13, and A.14, and expressions for uncertainty of lift coefficient, drag coefficient, and quarter chord pitching moment coefficient are shown in Eq. A.15, A.16, and A.17.

$$\partial L = \left(\left(\frac{\partial L}{F_N}\partial F_N\right)^2 + \left(\frac{\partial L}{F_A}\partial F_A\right)^2 + \left(\frac{\partial L}{\alpha}\right)^2\right)^{1/2} \tag{A.12}$$
$$\frac{\partial L}{F_N} = \cos\alpha$$
$$\frac{\partial L}{F_A} = -\sin\alpha$$
$$\frac{\partial L}{\alpha} = -F_N\sin\alpha - F_A\cos\alpha$$

$$\partial D = \left(\left(\frac{\partial D}{F_N}\partial F_N\right)^2 + \left(\frac{\partial D}{F_A}\partial F_A\right)^2 + \left(\frac{\partial D}{\alpha}\right)^2\right)^{1/2} \tag{A.13}$$
$$\frac{\partial D}{F_N} = \sin\alpha$$
$$\frac{\partial D}{F_A} = \cos\alpha$$
$$\frac{\partial D}{\alpha} = F_N\cos\alpha - F_A\sin\alpha$$

$$\partial M_{c/4} = \left(\left(\frac{\partial M_{c/4}}{\partial M} \partial M \right)^2 + \left(\frac{\partial M_{c/4}}{\partial F_N} \partial F_N \right)^2 + \left(\frac{\partial M_{c/4}}{\partial F_A} \partial F_A \right)^2 + \left(\frac{\partial M_{c/4}}{\partial X_{c/4}} \partial X_{c/4} \right)^2 + \left(\frac{\partial M_{c/4}}{\partial} Y_{c/4} \partial Y_{c/4} \right)^2 \right)^{1/2} \tag{A.14}$$

$$\frac{\partial M_{c/4}}{\partial M} = 1$$

$$\frac{\partial M_{c/4}}{\partial F_N} = -X_{c/4}$$

$$\frac{\partial M_{c/4}}{\partial F_A} = -Y_{c/4}$$

$$\frac{\partial M_{c/4}}{\partial X_{c/4}} = F_N$$

$$\frac{\partial M_{c/4}}{\partial Y_c/4} = F_A$$

$$\partial C_l = \left(\left(\frac{\partial C_l}{\partial L} \partial L \right)^2 + \left(\frac{\partial C_l}{\partial q_\infty} \partial q_\infty \right)^2 + \left(\frac{\partial C_l}{\partial c} \partial c \right)^2 + \left(\frac{\partial C_l}{\partial b} \partial b \right)^2 \right)^{1/2} \tag{A.15}$$

$$\frac{\partial C_l}{\partial L} = \frac{1}{q_\infty c b}$$

$$\frac{\partial C_l}{\partial q_\infty} = \frac{-L}{q_\infty^2 c b}$$

$$\frac{\partial C_l}{\partial c} = \frac{-L}{q_\infty c^2 b}$$

$$\frac{\partial C_l}{\partial b} = \frac{-L}{q_\infty c b^2}$$

$$\partial C_d = \left(\left(\frac{\partial C_d}{\partial D} \partial D \right)^2 + \left(\frac{\partial C_d}{\partial q_\infty} \partial q_\infty \right)^2 + \left(\frac{\partial C_d}{\partial c} \partial c \right)^2 + \left(\frac{\partial C_d}{\partial b} \partial b \right)^2 \right)^{1/2} \tag{A.16}$$

$$\frac{\partial C_d}{\partial D} = \frac{1}{q_\infty c b}$$

$$\frac{\partial C_d}{\partial q_\infty} = \frac{-D}{q_\infty^2 c b}$$

$$\frac{\partial C_d}{\partial c} = \frac{-D}{q_\infty c^2 b}$$

$$\frac{\partial C_d}{\partial b} = \frac{-D}{q_\infty c b^2}$$

$$\partial C_m = \left(\left(\frac{\partial C_m}{\partial M_{c/4}} \partial M_{c/4} \right)^2 + \left(\frac{\partial C_m}{\partial q_\infty} \partial q_\infty \right)^2 + \left(\frac{\partial C_m}{\partial c} \partial c \right)^2 + \left(\frac{\partial C_m}{\partial b} \partial b \right)^2 \right)^{1/2} \tag{A.17}$$

$$\frac{\partial C_m}{\partial M_{c/4}} = \frac{1}{q_\infty c^2 b}$$

$$\frac{\partial C_m}{\partial q_\infty} = \frac{-M_{c/4}}{q_\infty^2 c^2 b}$$

$$\frac{\partial C_m}{\partial c} = \frac{-2M_{c/4}}{q_\infty c^3 b}$$

$$\frac{\partial C_m}{\partial b} = \frac{-M_{c/4}}{q_\infty c b^2}$$

Tip speed ratio data were calculated based on RPM data acquired through electrical sensors as described in Section 2.4.3. As shown in Eq. 2.14, freestream velocity and EDF diameter were required in addition to RPM to calculate tip speed ratio. The expression for uncertainty in freestream velocity is shown in Eq. A.7. It was assumed that the uncertainty in the EDF diameter, D, was negligible. As a result, the expression for uncertainty in tip speed ratio can be found to be:

$$\partial \lambda = \left(\left(\frac{\partial \lambda}{\partial \omega} \partial \omega \right)^2 + \left(\frac{\partial \lambda}{\partial U_\infty} \partial U_\infty^2 \right)^2 \right)^{1/2} \tag{A.18}$$

$$\frac{\partial \lambda}{\partial \omega} = \frac{\pi D/60}{U_\infty}$$

$$\frac{\partial \lambda}{\partial U_\infty} = -\frac{\pi D \omega/60}{U_\infty^2}$$

A.3 Uncertainty in Pressure Measurements

Steady pressure data were collected in the form of the difference in pressure measured by each pressure module and a reference pressure, which was set to be the test section ambient pressure, p_∞. These data were subsequently nondimensionalized by q_∞ to obtain C_p data according to Eq. 2.13. As a result, the uncertainty in pressure measurements can be found to be:

$$\partial C_p = \left(\left(\frac{\partial C_p}{\partial (P - P_\infty)} \partial (P - P_\infty) \right)^2 + \left(\frac{\partial C_p}{\partial q_\infty} \partial q_\infty \right)^2 \right)^{1/2} \tag{A.19}$$

$$\frac{\partial C_p}{\partial (P - P_\infty)} = \frac{1}{q_\infty}$$

$$\frac{\partial C_p}{\partial q_\infty} = -\frac{P - P_\infty}{q_\infty^2} \tag{A.20}$$